Analysis and optimisation of postbuckled damage tolerant composite laminates

Rhead, Andrew

Award date:
2009

Awarding institution:
University of Bath

Analysis and optimisation of post-buckled damage tolerant composite laminates

Andrew Thomas Rhead

A thesis submitted for the degree of Doctor of Philosophy

University of Bath

Department of Mechanical Engineering

November 2009

……

I would like to dedicate this thesis to my beautiful wife Sarah; thank you for your love and support. And to my Mum and Dad who gave me my love for life and learning.

Contents

Table of figures

Acknowledgements

I would like to thank Great Western Research (GWR) alliance and Airbus UK who sponsored my PhD. Mr. N. Baker, Mr. M. Kinawy, Mr. C. Arnold, Mr. C. Hurd, D. Betts and Mr. N. Gathercole at the University of Bath for their assistance with experimental testing and Dr. Weaver and Mr. I. Chorley at the University of Bristol for providing impact testing facilities.

Finally, and most of all, I would like to thank Dr. Richard Butler and Prof. Giles Hunt for their teaching and guidance and for being the friendliest supervisors I have ever met. I have enjoyed working with you both.

Abstract

Barely Visible Impact Damage (BVID) can occur when laminated composite material is subject to impact, i.e. from runway debris or dropped tools, and may result in a significant reduction in the compressive strength of composite structures. A component containing BVID subjected to compression may fail via a number of mechanisms. However, it is assumed that the impact damage problems to be modelled will fail by delamination buckling leading to propagation of damage away from the original site. This precludes problems where the initial mechanism of failure is via kink banding or buckling of the full laminate.

An analytical model is presented, for application to various composite structures, which predicts the level of compressive strain below which growth of BVID following local buckling of a delaminated sublaminate will not occur.

The model is capable of predicting the critical through-thickness level for delamination, the stability of delamination growth, the sensitivity to experimental error in geometric measurements of the damage area and additionally establishes properties desirable for laminates optimised for damage tolerance. Problems treated with the model are split into two impact categories; ‘face’ (i.e. an out-of-plane skin impact) and ‘free edge’ (i.e. an in-plane stiffener edge impact) and two compressive loading regimes; ‘static’ and ‘fatigue’.

Analytical results for static and fatigue compression of face impacted plates show an agreement of threshold strain to within 4% and 17% of experimental values respectively. In particular, for impacts to the skin under a stiffener subject to static loading the model is accurate to within 5%. An optimised laminate stacking sequence has shown

an experimental increase of up to 29% in static strength can be achieved in comparison to a baseline configuration.

Finally, compression testing has been undertaken on three coupons in order to validate an analysis of static free edge problems. Analytical results are, on average, within 10% of experimental results. An optimised laminate is theoretically predicted to increase static compression after free edge impact strength by at least 35%.

Publications

The work presented in this thesis is an amalgamation of a number of papers that have been published in either international journals or conference proceedings. Following presentation at the ICCM 16, ICCM 17 and DFC10 conferences three of these papers were selected to form parts of three separate special issues containing the proceedings of the aforementioned conferences.
The following papers have been published in international journals:

- Rhead AT, Butler R, Hunt GW. *Post-buckled propagation model for compressive fatigue of impact damaged laminates*. International Journal of Solids and Structures 45(16):4349-4361, 2008. (Invited special issue paper)

- Rhead AT, Butler R. *Compressive static strength model for damaged composite laminates*. Comp. Sci. Tech, 69(14): 2301-2307, 2009.

The paper below has been accepted for publication:

- Rhead AT, Butler R, Marchant D. *Compressive strength of laminates following free edge impact.* Composites Part A, 2009. (Invited special issue paper)

The following papers have been published as part of the appropriate conference proceedings:

- Rhead AT, Butler R, Hunt GW. *Enhanced compressive fatigue model for impact damaged laminates*. Proceedings of ICCM 16, Kyoto, Japan, 2007.

- Rhead AT, Butler R. *A static compressive strength model for damaged composite laminates*. Proceedings of ECCM 13, Stockholm, 2008.

- Rhead AT, Butler R, Marchant D. *Compressive strength of laminates following free edge impact. DFC10 Sheffield, 2009.*

- Rhead AT, Baker N. Butler R, *Compression testing of laminates optimised for damage tolerance.* Proceedings of ICCM 17, Edinburgh, 2009. (Invited to become part of a special issue of the Journal of Applied Composite Materials)

- Baker N, Rhead AT, Butler R. *Optimisation of aerospace laminates for damage tolerance.* 7th ASMO-UK/ISSMO International Conference of Engineering Design Optimisation, Bath, 2008.

Nomenclature

A_{ii}	In-plane laminate stiffness'.
$[A]_D$	Axial stiffness matrix for the delaminated sublaminate.
A_{11}	Axial stiffness in the principle load direction.
a_1	Energy due to end-shortening in the pre-buckling regime
a_2	Membrane energy in the pre-buckling regime.
a_3	Membrane energy in the post-buckling regime.
a	Major axis length of elliptical delamination in the CDM.
b	Minor axis length of elliptical delamination in the CDM.
B_{ii}	Laminate coupling stiffness'.
d	Diameter of the tup used for impact.
D_{ii}	Laminate bending stiffness'.
E_{11}	Young's Modulus in the principle fibre direction.
E_{22}	Young's Modulus orthogonal to the principle fibre direction.
G_I	Strain energy release rate for Mode I fracture.
G_{IC}	Threshold SERR required for Mode I resin fracture.
G_{II}	Strain energy release rate for Mode II fracture.
G_{IIC}	Threshold SERR required for Mode II resin fracture.
G_{12}	Intra laminar shear modulus.
I	Second moment of area.
$\{k\}$	Laminate curvatures
K Euler	Constant used to describe all non-length related terms in buckling of a strut.
k_0	Elastic buckling coefficient for an orthotropic plate

$l_{\max}$ Diameter of the circle containing the full area of delamination.

l Delamination length.

l_b A length derived from the tup diameter for the smallest. delamination in the LDM model.

M_X Moment in the principle loading direction.

M_y Moment in the principle transverse direction.

M_{xy} Moment in the principle/transverse plane.

$\{N\}_D$ Applied loads for the delaminated sublaminate.

N_X Applied load in the principle loading direction.

N_X^C Critical principle buckling load of the delaminated sublaminate.

N_Y Applied load in the principle transverse direction.

N_Z Applied load in the out-of-plane direction.

N_{XY} Shear load in the principle/transverse plane.

P Constant used to describe all non-length related terms in Euler buckling of a square plate.

R_S Sensitivity of sublaminate threshold strain to delamination size.

r Ratio of post-buckling stiffness to pre-buckling stiffness.

T Total laminate thickness.

t Cured lamina or layer thickness.

U_1 Bending energy per unit width.

U_2 Membrane energy in the delaminated sublaminate.

U_2^* Membrane energy in the undelaminated sublaminate.

ν_{12} Poisson's ratio (principle to transverse).

W	Free-edge impacted specimen width for the CDM.
$\{\varepsilon\}_L$	Strain vector for the full laminate.
ε^C	Critical sublaminate buckling strain.
ε_A^C	Critical sublaminate buckling strain following propagation.
ε	Applied strain in the principle loading direction.
ε_y	Applied strain the transverse loading direction.
ε_{th}	Applied principle strain required for propagation to occur.
ε_x	Applied strain in the principle loading direction.
ε_{xy}	Shear strain in the principle/transverse plane.
δl	Infinitesimal length used for propagation calculations.

BVID	Barely Visible Impact Damage.
CFRP	Carbon Fibre Reinforced Plastic.
FEA	Finite Element Analysis.
CAI	Compression After Impact.
NDT	Non-Destructive Testing.
SERR	Strain Energy Release Rate.
CCT	Crack Closure Technique.
VCCT	Virtual Crack Closure Technique.

1. Introduction

In a weight for weight comparison to other aerospace materials currently in use, laminated composites have excellent in-plane properties. This has led to Carbon Fibre Reinforced Plastic (CFRP) becoming the material of choice for aircraft designers. CFRP laminated structures are created by layering plastic sheets reinforced with carbon fibres aligned in a single direction. By rotating and stacking these sheets in certain sequences during the layering process laminates can be given varying load carrying capabilities.

As has been popularly reported for a number of years, CFRP has the potential to radically reduce the weight of any vehicle in which it is employed. However, this weight saving is not being fully realised even in the most recent aircraft such as the Boeing 787 and the Airbus A380 that contain high proportions of composite parts. The approach to using composites in these new aircraft has, so far, been somewhat conservative which has meant the potential weight saving offered by these materials may not have been completely realised. This conservativeness is due to a variety of problems associated with incorporating composite materials into aircraft structures and their resistance to damage.

When layered structures are subjected to out-of-plane impact loads for example flying runway debris or dropped maintenance tools delaminations can occur which may significantly reduce static strength. Some of these impacts leave exterior marks and can be located by sight. However, other impacts are not as easily seen, generally due to them being in difficult to inspect areas or because of their size, such damage is known as Barely Visible Impact Damage (BVID). It is generally accepted BVID leaves surface marks only a few millimetres in diameter but causes below surface delaminations

to occur with diameters that are typically tens of millimetres in size. Clearly, BVID can be very dangerous but it can also be unpredictable with regard to its position and frequency of occurrence. BVID becomes particularly dangerous when compressive loading causes buckling of sublaminates in the BVID region which in turn forces opening of delaminations allowing damage to propagate from the initial site. This increasing area of damage can lead to widespread delamination and subsequent failure of components. Clearly with the above aircraft about to or having recently entered service the need to advance understanding of the mechanics of composite structures has a renewed impetus.

Following present regulations for aircraft manufacture [1] which effectively state that, provided the level of impact required to cause BVID is due to a "realistically expected event" (defined as a probability of occurrence of 1 in 10^5 flying hours) it must be assumed that such BVID is present and that the structure must tolerate this damage at ultimate levels of load without failing. Current design methodologies account for BVID by applying empirically derived conservative strain limits at ultimate levels of load. This is due to an inherent difficulty in detection of BVID and a lack of accurate and time efficient modelling capacity. These regulations become especially conservative when dealing with free edge impact on stiffeners due in part to the extra difficulties encountered during in-service inspection of stiffeners.

Clearly there is an excellent opportunity to save weight by challenging current design methodologies through better prediction of the behaviour of delaminated composite materials under compressive and hence increasing the damage tolerant strain limit. A component containing BVID subjected to compression may fail via a number of mechanisms including kink banding, global or component buckling and propagation of local delaminations. However,

delamination propagation as a result of local buckling is the most representative of failure in an aerospace structure and is thus the process modelled in this work.

With these points in mind, it is evident that a mechanical model is required that predicts the threshold strain, below which damage will not propagate following delamination buckling for general laminates, whilst maintaining the speed of calculation necessary for preliminary design of aircraft structures. Currently, models in the literature fall into two categories; Finite Element Analysis (FEA) models such as [2] which are computationally expensive and require input of predetermined layers of cohesive elements to model propagation of delamination, and analytical models [3, 4] which, though computationally efficient, are relatively inaccurate and limited to isotropic or quasi-isotropic coupons.

The latter analytical approach has been taken in this work and a computationally efficient enhanced version of an earlier quasi-static analytical model (hereafter the beam model) [5] has been derived and extended to include general laminates, stiffened panels and edge impacted stiffeners. This mathematical model, similar to Chai [6], calculates the level of strain required to propagate an area of BVID at a critical delamination level. This level of strain (hereafter the threshold strain) is taken as a lower bound to the compressive strength of simple composite structures containing BVID. The enhanced model uses simple approximations of BVID morphologies and an updated propagation approach based on fracture mechanics and the available strain energy in the delaminated, post-buckled plate together with damage principles similar to those proposed by Hwang and Liu in [7]. In their work with 2D plane strain FEA models, they suggest that buckling of a composite plate with multiple delaminations arising from out of plane impact damage can be simplified to buckling of a plate with a single delamination at a critical

level in the laminate. Melin and Schön [8] report this critical level to be at a depth of around 10%-20% of the total thickness. The model is used to show whether the initial propagation is stable or unstable, and to evaluate sensitivity to parametric variation. In [9] certain laminate properties, desirable for damage tolerant structures, were also revealed.

The model has been applied successfully to a variety of problems from the literature, see [8,10-14]. Including the fatigue loading problems reported in the experimental studies of Curtis et al [10], Melin and Schön [8], Melin et al [11] and Chen et al [12]. The results of which are described in Chapter 7.1.

Static strength problems are treated in Chapter 7.2 and include applications to; coupon tests from [8], [11] and [13], a stiffened panel from [14], and standard coupons, with stacking sequences optimised to maximise static strength following impact damage. These laminates, together with a control coupon were impacted and then loaded in compression until failure. Results of these experiments indicate large increases in static strength can be produced and that the model is capable of making qualitative predictions about the compression after impact (CAI) strength of composite laminates. Detailed C-scan information collected during the course of these experiments has allowed an improved representation of BVID to be employed which results in enhanced accuracy in comparison to the initial approximation to damage morphology.

The results of three baseline experimental tests conducted in order to validate the model for CAI of edge impacted stiffeners will be provided and compared with the theoretical results in Chapter 7.3. The experiments consisted of impacting a T-stiffener section (with two different impact energies) on its free edge at three separate locations (along its length) before cutting it into coupons and testing each under static compression until failure. C-scans of the impact

damage were used to produce a simple approximation to the damage morphology of the free edge impacts which has aided in the successful implementation of the extended CAI model. To the author's knowledge this is the first analytical model to tackle CAI *strength* for the in-plane free edge case, although free edge impact *damage* has been explored experimentally and with a finite element approach e.g. [15].

2. Scope, objectives and thesis overview

2.1 Scope

The concept of this to work is to derive an analytical model that calculates the level of strain below which propagation of BVID does not occur. The modelling methodology must be flexible enough to be applicable to any problem based on BVID in a flat structure (or one that can be approximated as such) including enclosed and free edge delamination in simple geometric features under static or fatigue loading. However, while accomplishing the above the model must remain computationally efficient and accurate enough to be used as a first stage design tool that can process a large number of problems very quickly. The model is to be limited to axial compressive loading as it is understood that, although transverse and shear loading are likely to occur in aircraft wing panels (the main structures for applications of the model), axial compressive load is the dominant force particularly when manoeuvres place the wing under loads close to the ultimate allowable level. It is intended the model will require an accurate description of BVID information from Non-Destructive Testing (NDT) or a separate model taken from the literature as creation of such a model is a large undertaking and beyond the scope of this work. However simple methods of approximation of BVID are to be derived so as to allow the model to work with limited information and to be as flexible as possible.

In order to fulfil the above thesis roadmap the following objectives are to be fulfilled:

2.2 Objectives

1. Derive simple approximations to complex BVID morphology that allow for quick computation times.

2. Identify a computationally efficient method for calculating the critical strain required to buckle a delaminated sublaminate.

3. Create an analytical model that determines a ‘safe’ level of strain for plate like composite structures with BVID under static and fatigue compressive loading regimes.

4. Investigate the sensitivity (robustness) of the model to problem parameters including material properties and damage shape, area and depth.

5. Identify problems in the literature suitable for validation of the model, or where no suitable problem can be found undertaking of experimental testing instead.

6. Via the model identify candidate optimised laminate stacking sequences that will improve damage tolerance or CAI strength.

7. Test these laminates to experimentally verify the optimisation predictions and compare these results with those from previous experimental tests.

2.3 Thesis overview

Chapter 3 – Literature review

A literature review is undertaken that establishes a need for the original work in this thesis to be conducted by highlighting the lack of a sufficiently accurate computationally efficient modelling capability suitable for preliminary design work. Currently available NDT techniques and models for imaging or modelling BVID are considered and a suitable method is identified for calculating the bucking strain of delaminated sublaminates.

Chapter 4 – Damage morphology

In Chapter 4 four damage models that use NDT representations of damage morphology to produce through thickness delamination distributions are derived. The models cover damage distribution in enclosed and free edge delamination problems including damage in stiffeners and stiffened panels. The models require only very simple (if any at all) algebraic computation.

Chapter 5 – Sublaminate buckling

In this chapter the principles of load transfer from the base laminate to the delaminated sublaminate and the associated boundary conditions are described for enclosed and free edge delaminations. Implementation of the boundary constraints for enclosed and free edge problems in the infinite strip program VICONOPT, which is used to calculate buckling strains, has been described.

Chapter 6 – Propagation model

An analytical model is derived that uses basic and freely available material properties, a damage representation simplified from NDT images (as derived in Chapter 4) and a critical buckling strain,

calculated using methods detailed in Chapter 5, to calculate the level of strain for plate like composite structures with BVID below which propagation will not occur. Comparisons are made with a fully 2D analytical model from Chai [3].

In addition equations are derived that analyse the sensitivity (robustness) of the model to problem parameters including material properties and damage shape, area and depth. The direction and stability of growth are analysed and pure Mode I growth is shown to be a conservative approximation to mixed mode growth. Optimal sublaminate properties for improved damage tolerance are also derived.

Chapter 7 – Experimental validation

In Chapter 7 the robustness (different to the analytical treatment given in Chapter 6) and validity of the modelling methodology is examined by applying the model to a wide variety of laminates, enclosed BVID morphologies and types of CFRP which were identified for this purpose. Where suitable problems were not found, such as in the case on in-plane free edge impact on a stiffener, experimental work has been undertaken the results of which are included and discussed.

Using results derived in Chapter 6 candidate optimised laminate stacking sequences are identified that theoretically improved damage tolerance or CAI strength for all loading regimes and types of BVID (enclosed or free edge). The results of experiments using these stacking sequences are included together with a discussion of their implications.

Chapter 8 – Final discussion

An overall final discussion is conducted that analyses the effects of the various assumptions that are implicit to the modelling methodology. This includes a discussion of to which real-life problem situations the model can be applied and to what extent the assumptions may affect its validity.

Chapter 9 – Final conclusions

Overall conclusions about the models effectiveness are drawn based primarily on a percentage comparison with experimental data from the test problems. The accuracy of the model in all analysed load BVID combinations is given. Conclusions are also drawn about the suitability of the model as a predictive strategy for optimising composite laminates for damage tolerance.

Chapter 10 – Future and ongoing work

This final chapter deals with suggested further work, in particular projects that are currently being undertaken by the author and parallel projects using the modelling methodology set out in this thesis being undertaken by colleagues are discussed. Further applications and possible modifications to the methodology that will allow new classes of problems (including certain curved structures) to be analysed are also suggested.

3. Literature review

The purpose of this literature review is to define the novelty of this work, describe where it fits into current research, detail the earlier research it draws upon and the research it models.

To achieve this literature will be considered in the following categories:

3.1 **Impact damage**

3.2 **Failure criteria**

3.3 **Sublaminate buckling**

3.4 **Experimental work**

3.5 **Analytical models**

3.6 **Finite Element Analysis methods**

3.7 **Optimisation techniques**

3.1. Impact damage

As described in the introduction in order to make a fully contained model for analysis of BVID and its propagation it is necessary to produce a model that will describe impact damage from a typical impact event. Work here focuses on low velocity impact damage as this is the regime of impact associated with BVID. Static impact is ignored as it is unlikely on an aircraft and high-velocity impact is also ignored as although it can cause significant damage it is generally easily detected and hence it is very unlikely that such an impact

would be present on an aircraft forced to endure loads approaching those required to propagate damage under static conditions. An analytical and FEA approach to the problems and their outcomes are given below together with some interesting experimental results that could be useful in future attempts at deriving a model for impact damage prediction.

Davies and Zhang [16] report a strategy for ‘predicting the extent of internal damage in a brittle carbon fibre laminated composite structure’. The strategy was implemented in FEA and compared to experimental coupon tests which used a variety of boundary conditions. The main principle of the strategy was to remove the need for a full 3D stress field. This was achieved by considering the response of structures to stress waves and limiting the wave speed to 20m/s or less thus allowing the structure to respond in a way suitable for application of simple engineering theory for plates and shells. Good agreement was found between the FEA model and the experimental worked carried out. Davies and Zhang also note the damage area vs. maximum force plots for impact are independent of size and dynamic response of the impacted structure and thus the occurrence of structural damage during impact can be derived from discontinuities in a coupon’s force vs. impact time plot

An analytical impact damage model that predicts the number of failed plies and the total fibre damage area in axisymmetric composite circular plates is derived by Lee and Soutis [17]. The model is found to be in good agreement with impact tests and an FEA model reported in the same paper. The model uses the Rayleigh-Ritz method together with the principle of virtual work to model the fibre damage area and number of failed plies occurring from a transverse load applied to the centre of a circular laminate. A maximum strain criterion, simple stiffness degradation scheme and classical laminate plate theory were used to predict failure within plies.

Lammerant and Verpoest [18] conducted impact experiments on transversely loaded plates, with impact normal to the plane of the laminate, in order to verify FEA predictions of matrix cracking and delamination development. It was shown that accurate modeling of this development requires use of energy criteria and inclusion of mode III loading effects. For the initiation and growth of delaminations they suggest it is necessary to include the existence of matrix cracks and to allow for growth in both horizontal and vertical directions.

In their paper Qian et al [19] propose scaling rules for impact response in undamaged specially orthotropic laminate plates that allow results from laboratory experiments to be applied to full-scale components. Rules are offered for the scaling of maximum strain in a plate, impact velocity, contact force, contact pressure and impactor mass as functions of plate scaling. Experiments are conducted and show good agreement with analytically derived rules.

Ollsson has individually authored two papers [20,21] on low-velocity impact and is the lead author on a third [22]. The first of the two individually authored papers describes an analytical model that shows good agreement with exact numerical solutions and a wide range of experimental data for peak impact load. The second of the two papers predicts the critical load required for delamination growth during impact. Although both models are analytic and therefore computationally efficient, neither can predict the extent of individual delaminations which is a necessary initial condition for the propagation model developed in Chapter 6. However, as noted by the author, the models may be capable of determining damage resistance of composite laminates and could prove to be a useful first stage design tool. The third paper describes the development of a closed form model validated against an FEA model that predicts “delamination onset in transversely isotropic laminated plates under

small mass, high velocity impact". The authors report a good correlation between the two. However, again due to the models only predicting delamination onset at a single critical level and not being applicable to anisotropic composite laminates they are not of use for the work to be undertaken here.

Work was carried out by Greenhalgh et al [23] on the effects of impact events at various locations on a CRFP wingbox. The wingbox was impacted in three areas: in the bay between spars, directly over the centre of a spar and at the edge of the flange of a spar. These impacts were also carried out under three different loading conditions: no load, upper surface in tension and upper surface in compression. The following conclusions were drawn by the authors:

- Impact location was found to have the greatest effect on results although loading also made a large contribution.
- There was no interaction of growth between impact sites in pre-loading or test to failure.
- There was a linear relationship between the impact duration and the damage producing during area indicating the two are directly linked.
- Impact between spars produced circular damage areas.
- Impact near the flange of a spar produced 50% larger damage elongated parallel to the spars.
- Tensile loading promoted damage extension parallel to the spars.
- Compression loading promoted damage extension perpendicular to the spars.

- Impacts closer to the tip of the wingbox promoted damage formation parallel to the spars.

Experimental impact work has also been carried out by Breen et al [24] who looked at out-of-plane central and near edge impact on different thicknesses of laminates made from non crimp fabric layers. The authors note that near edge impacts produced larger amounts of delamination than the central impacts but that central impacts produced a higher density of cracks than the near edge impacts. However, the most important conclusion and one that has helped to drive some of the work presented in Chapter 7 is that the residual strength of near edge impacted coupons is significantly lower than centrally impacted coupons making this type of impact a more dangerous threat to an aircraft's structural integrity.

Similarly, Malhorta et al [15] compared the damage extents of out-of-plane near edge impacts and in-plane, on-edge impacts such as might occur on a stiffener web. An FEA simulation of the impacts showed good agreement for peak loads and displacements. The authors conclude that in-plane impacts are more severe than out-of-plane near edge impacts which themselves, as established above, cause considerably more damage than out-of-plane central impacts. In-plane impacts were seen to cause longer multiple delaminations in comparison to out-of-plane impacts which caused a single shorter delamination. This work is again a major driver for some of the work carried out in Chapter 7.

Models available in the literature to predict damage formation have been seen to be too inaccurate or complex and problem dependent for implementation in this work which has the objective of being computationally efficient and as widely applicable as possible. Hence focus will be turned in later chapters to developing simple approximate damage models based on damage viewed using NDT techniques such as C-scan.

3.2. Failure criteria

Prior to modeling the problem of propagation of BVID it is necessary to understand the failure mechanisms associated with it. In the main this involves sublaminate buckling but not global buckling. The principal mechanism associated with propagation of BVID is delamination buckling which is recognised by many authors [2-7,25,26] in their attempts to model this problem. However, BVID can also propagate (without buckling) via a Mode II shearing action between plies though this tends to require a higher level of strain than that required for delamination buckling to cause propagation and as such is not such a series threat to the aircraft. There also other failure mechanisms exist for compressed composite laminates and since a full scale component may not always fail by local delamination buckling failure but rather by global buckling [2] it is worth noting the work by Yerramalli and Waas [27] who introduce a non-dimensional number to predetermine the failure mechanism of undelaminated compressively loaded composite laminates. This number η can be used to determine whether a laminate will fail by kinking or splitting which are reported as the two prevalent failure mechanisms for undelaminated compressed composite laminates. The authors note that the key properties of the laminate that determine η and hence the failure mechanism are fibre diameter, interfacial fracture energy and the effective shear properties at failure. Examples are taken from the literature to support their findings. Other work by Berbinau et al [28] suggests that for failure by kink banding in unidirectional carbon fibre composite laminates, the microbuckling failure associated with kinking occurs on the compressed side of the fibres as opposed to the tensile side. This is supported by a favourable comparison with experimental work. It is

also noted that their work implies the microbuckling half wave length is of the same order of magnitude as the kink band width.

3.3. Sublaminate buckling

As the work in this thesis centres on the local delamination buckling failure process a key aspect will be the calculation of the critical buckling strain associated with the delaminated sublaminate. This will be the main concern of this subsection. However, delamination propagation following local buckling of the sublaminate is not the only failure process possible for a composite laminate and although this work will not seek to model these failure methods for completeness they are briefly explored.

Work on buckling of a number of bodies made from homogenous material was carried out and recorded by Thompson and Hunt in 1984 in their book Elastic Instability Phenomena [29]. Since then a large body of work has examined the buckling of plates made from heterogeneous layers i.e. composite laminates. A summary of key papers and their conclusions important to future work are given below.

Hunt et al [30] used a fourth order differential equation to model a delaminated strut. The buckling solutions of the model show good agreement with FEA results both quantitatively and qualitatively. Indeed it captures the complicated bifurcation and secondary bifurcation in buckling modes that can be displayed in experiments. The authors note that the FEA comparison implies that for thin film buckling critical loads are effectively the same for pinned and clamped-end conditions on the loaded boundary.

A Rayleigh-Ritz solution is derived by Suemasu et al [31] to determine the buckling of a rectangular plate under compressive

loading with a free edge delamination. Results of experiments undertaken to test the validity of the model are reported and comparisons drawn. The authors made the following conclusions:

- the reduction of global buckling load for an edge delaminated plate is significant.
- The lowest load leading to instability with constant size of delamination occurs when the delamination is located on the mid-plane.
- Local instability is observed for large delaminations when they are located near the surface.

Hwang and Liu [7] consider the buckling behaviour of composite laminates with multiple delaminations under uniaxial compression. A number of configurations of delaminations are considered, of particular interest is the 'Christmas tree' configuration associated with BVID. The authors conclude that this configuration can be successfully approximated by a single delamination with little effect on the buckling load. The overall effect for all configurations is that the closer the longest delamination is to the surface the better approximation of a single delamination is. However, the mode of buckling may be affected by changes in length and configuration so care should be taken.

Anderson et al [32] present a paper on VICON (VIPASA [33] (Vibration and Instability of Plate Assemblies including Shear and Anisotropy) with CONstraints), the buckling analysis part of the buckling and optimisation program VICONOPT [34] (VICON with OPTimisation). VICON uses forces, calculated by describing plate deflections with complex Fourier series, to determine the total potential energy of a structure or plate which is then minimised with

respect to constraints, i.e. the circular boundary of a delamination, to give the governing differential equations.

The plate can be supported by differing types of constraint and be made from anisotropic materials. The paper extends program VIPASA to include analysis of skewed buckling modes resulting from material anisotropy. Results are presented that show the increase in accuracy of the program, the number of terms required for convergence, the number of discrete restraints require to simulate continuous restraint and the computation time required to FEA. The computation time required is approximately 1% of the time required for a full FEA analysis.

Diaconu and Weaver [35] suggest a solution for the post-buckling response of long unsymmetrically laminated plates under axial compression. The method is a simple one using non-dimensional parameters and is compared to two FEA models with differing boundary conditions for verification. The comparison suggests the model usually gives results that lie between the two FEA predictions and could be used as a happy medium for design purposes. The results also suggest that the postbuckling behaviour is highly dependent on the boundary conditions placed on the lateral edges.

Harris [36] presents a model for buckling and post-buckling of composite plates under biaxial loading. The relevance of coupling terms in determining the shape of the buckle via the buckling wave pattern and consequently determining the loads required to buckle the plate are noted in particular.

The method chosen for calculating local sublaminate buckling loads was VICONOPT as it offers an accuracy and flexibility in problem application that is not available to non-numerical analytical solutions and a flexibility and computational efficiency that is not possible with an FEA solution.

3.4. Experimental work

Some of the earliest experimental work on impact after compression of composite laminates was carried out by Chai and Babcock [37]. Panels of composite laminates were impacted by a projectile while in compression and were then compressed to failure. Displacement was measured using the Shadow-Moire technique and cross sections were taken of the laminates to investigate the internal damage. The authors concluded that the damage growth due to compressive loading occurs normal to the loading direction and can be split into distinct stages. In particular, the first stages of global plate reaction to impact, damage generation and initial growth phase can be separated from the final rapid stages of damage growth. It is this last finding that the authors consider maybe helpful in formulating a model of damage growth.

Curtis et al [10] tested a variety of composite laminates for fatigue and static strength under both tension and compression. An important result of their work was that the thermoplastic material IM8/PEEK performed better than the thermosetting materials in CAI tests due to its resistance to delamination, but much worse in undamaged compression tests. This was due to lower shear modulus and greater fibre waviness. Extensive C-scan images were also included with this paper which may be useful in determining areas of damage for impact. The authors noted an ‘incubation’ period where delamination propagation was not seen to occur outside the original damage area before further growth occurred at a higher number of cycles; a fact that will be made use of when modelling fatigue in Chapter 7.

Zhou and Rivera [38] investigated the effects of impact damage and embedded delaminations on the residual compressive strength (RCS) of 16 ply carbon/epoxy panels. A damage area threshold was found at 25% of the panel width that separated effects of degradation

on the RCS and global buckling load into two regions. In the first region below the 25% panel width threshold relating to small amounts of damage, no effect was reported on the global buckling load but the RCS was significantly reduced and little evidence was found for sideways propagation. In the second region above the threshold level, relating to significant damage, global buckling loads were found to have reduced moderately but no further reductions in RCS were discovered. However, in this second region some evidence was found for sideways propagation of damage. The authors conclude that global buckling loads cannot be used to approximate RCS and that size and number or intensity of delaminations are important factors effecting RCS.

Asp et al [39] carried out static compression tests on impact damaged, artificially damaged and undamaged plates to provide information for a database that can be used to validate residual compressive strength models. The authors concluded from the tests that for impact damaged plates the global buckling load was 10% lower than the artificially delaminated plates and 20% lower than the undamaged ones. Propagation was found to occur perpendicular to the loading direction. Delamination growth for the artificially delaminated plates was found to depend on the thickness of the plate. Growth was most localised in plates with thin delaminated members and its width increased with the delaminated member thickness.

Short et al [40] implemented drop weight tests on the convex side of curved Glass Fibre Reinforced Plastic (GFRP) laminates and then compressed them until failure occurred. The authors concluded from their results that impact areas for curved laminates were slightly larger than those for flat plates. However for both artificially delaminated and impact damaged curved laminates residual compressive strength was similar to that for flat plates. Artificial

delamination was also found to be a good approximation for impact damage in curved laminate plates.

Wang et al [41] considered the reduction of compressive strength of composite laminates containing multiple artificial delaminations at different levels through the thickness. The conclusion was made that multiple delaminations lead to larger reductions in compressive strength than single ones and that the worst case scenario is for multiple equally spaced delaminations through the thickness i.e. equal thickness sublaminates. They also noted that it has been observed that delamination is most likely to occur between plies of highest difference in angle.

Chen et al [42] reported on a new experimental set-up for testing composite laminates in both fatigue and static strength. At the heart of the new process is acoustography (effectively real-time c-scanning) which uses ultrasonic imaging to view the composite laminate in situ under loading. In the tests carried out with the equipment the authors noted that when a specimen was loaded and then unloaded the images showed that the damage was 15% larger in the loaded state. The authors concluded that this was due to already existing cracks being opened enough during loading to be present on the acoustography images. The implication from this is that c-scanning, since it doesn't consider specimens under load, will not pick up the full damage area and so results from it should be treated with caution.

Lee et al [43] carried out testing on thick composite laminates to discover failure mechanisms, something the authors note, which has received little attention in the literature. The main conclusions from the testing of thick composite laminates are that scaling rules apply to the compressive strength with regards to the thickness. As the thickness increases the compressive strength decreases. This is linked to the larger amounts of inherent defects such as voids and

fibre waviness. The same effect was found for specimen volume. All the specimens were also found to fail via kink banding.

Falzon et al [44] tested t-stiffened composite panels under uniaxial compression. The authors found that the panels failed in a different way to panels stiffened using other stiffeners which generally failed after stiffener debonding. In this case damage initiated at the free edge of the stiffener web at a node-line and the failure mechanism was described as an interlaminar shear stress failure occurring due to a combination of compressive loading on the post-buckled stiffener blade and twisting induced at the node-line of the buckled stiffener.

Singh and Greenhalgh [45] summarised a body of work carried out by the GARTEUR Action Group AG22. The work consisted of experimental test data on damage formation, growth and failure in coupons and stiffened panels. The following conclusions were obtained:

- Delamination growth is generally found to occur transverse to the direction of the applied load. Initial damage size and shape had little effect on damage processes compared to depth of delamination and ply orientation in the delaminated material.

- Delamination growth at a ply interface was always parallel to fibres in the ply closer to the surface; cracks would migrate through plies to interfaces closer to the surface to obtain this.

- Damage in the bay of a stiffened panel is more detrimental to strength than damage partly or fully beneath a stringer for a given impact energy. However, the authors didn't compare equal damage areas which may produce a different conclusion.

Greenhalgh et al [46] tested a CRFP wingbox with a 150J impact on a spar foot under bending load. The loading was such that the impact

site was placed under compression. A detailed analysis was carried out noting and explaining the key events in chronological order until complete failure occurred. The following conclusions and observations were made. No interaction occurred between low impact energy sites and the main high energy 150J impact site. However, there was a large loss in performance. Initial damage spread as mode I growth to the two central spars and this was followed by a narrow band of surface delamination across most of the width. Delaminations also developed close to and within the spar feet. Final failure occurred when the spars and skin separated under compression. The primary damage growth mechanisms were very similar to those for smaller structural elements. In contrast to [45] the authors note that impacts under stiffener feet reduced the strength of the stiffened panels more than impacts to the skin between bays. Problems in this paper are analysed in Chapter 7.

Another paper by Greenhalgh et al [14] presented work on a comparison of impact damage and embedded defects in stiffened panels. Results from this paper reinforced the findings of [45] that damage underneath a stiffener foot is considerably more detrimental to stiffened panel strength than damage in the mid-bay. Other findings in the paper indicate that damage had little effect on the buckling strain of the panels and that failure mechanisms related to embedded delaminations and impact damage are very. This leads the authors to conclude that experimentally mimicking impact damage with a single level embedded delamination may be of ‘limited validity’.

Benmedakhene et al [47] used acoustic emission monitoring to investigate initiation and growth of delaminations in composite specimens with 5% perpendicular woven fibres. Delaminations are introduced to the specimens during manufacture using Teflon inserts. Pure mode I energy release rate was established using a double

cantilever beam (DCB) test. The authors conclude that fracture mechanisms are a function of velocity and that at low velocity failure propagates principally in the resin and progressively as the velocity increases, the failure propagates in the fibre/matrix and interplay interfaces.

3.5. Analytical models

It is the intention of this review to focus on the delamination buckling method. With this in mind delamination buckling models will be mainly considered here although a few alternatives are mentioned for completeness.

Nyman et al [48] consider two possible methods for the calculation of residual strength of composite laminates. The first method is the soft inclusion method and the second is delamination buckling theory. Both methods are tested against a range of materials and laminates which were either experimentally tested or modelled using an FEA analysis. The damage in the laminates was also modelled in three different ways. The first used a best fit ellipse that contains the full area of damage. The second and third methods used the median of the angle of plies adjacent to each delamination to determine the angle of an ellipse that has length constrained by the length of delamination and width based on a combination of the length of the delamination and the median angle. The second and third methods differ here on the way the length of delamination and median angle are combined. Model and test predictions for the failure stress of the damaged laminates are displayed graphically and a number of conclusions are drawn. The most important of these is that for low-impact energies the authors delamination buckling theory combined with the simplification of the damage area to an ellipse and an approximation of the strain energy release rate around its edge gives

excellent predictions of residual strength. Chai et al [6] made a first attempt at modeling delamination related failure in laminated plates. A one dimensional thin film case and a number of general cases were considered including multiple delaminations. The one-dimensional thin-film model was derived first (using beam stiffness properties) as it is fully analytic and more simple than the general case. The one-dimensional general case allowed the base and sublaminate to buckle which required some numerical work to be undertaken. In their conclusions the authors note that the models show an interesting variety of behaviours in particular they find growth can be stable, unstable or unstable followed by stable. No experimental validation is undertaken as the authors state that the model was not capable of dealing with the 'complex dynamic process of delamination growth in an impacted plate'.

Chai and Babcock [3] also derived a two-dimensional model of a plate with a single elliptical (or circular as a special case) delamination under compression. The model was mainly analytic with numerical calculation used to determine coefficients in the necessary buckling equations. They report a variety of crack growth characteristics including 'stable, unstable and unstable followed by crack arrest'. They conclude the parameters controlling the type of growth are 'the dimensions and elastic properties of the cover layer, the Poisson's ratio of the parent medium, the loading history and the fracture energy'. It is noted that a decrease in the radius of delamination or an increase in the thickness of the delaminated layer narrowed the strain difference between buckling and growth. This is something that should be considered when designing components that are purposely allowed to buckle.

Butler et al [5] proposed an analytical quasi-static combined buckling and propagation model based on a thin film assumption that represented the final stages of growth of fatigue damage when

delaminations have buckled and subsequently opened. Their model used the bending energy, with laminate bending stiffness, and membrane energy of a strip, of equal length to the delamination, to calculate the strain energy release rate (SERR) for the laminate at every possible level of delamination. The infinite strip buckling program VICONOPT was used to calculate the buckling strain for the sublaminates which was necessary for the calculation of the SERR. This SERR is then compared with the failure criterion G_{1C} (the SERR required to crack the resin) to determine a critical level of strain. Experimental fatigue tests on AS4/8552 coupons with BVID were carried out by the authors. The model was validated against the results from the experimental work and a set of XAS/914 results from the literature. It was found to predict fatigue limit strains to within 4% of experimental values. Butler et al [5] also made the assumption that a single circular delamination at some critical depth within the laminate represents the full extent of BVID which proved very successful. However, Suemasu [49] studied the effect of multiple delaminations on the compressive buckling behaviour of composite panels and an analytical model was derived that tried to capture these effects, the predictions of which compared well with experimental and FEA results. A number of conclusions were drawn from the work the most pertinent of which being that significant reduction in the compressive strength of delaminated plates can be accounted for by assuming multiple delaminations, kinks appear at the delaminated regions even at low loads and when multiple delaminations are located near clamped ends, the buckling load is reduced.

An analytical approach to post-buckling and growth of delaminations in composite plates is presented by Kardomateas [4]. Closed form solutions were derived for the strain energy release rate and mode I/II mixity, and also for the load and midpoint deflection for comparison with experimental studies. The approach taken was

asymptotic which negates the need for a thin-film assumption. Taylor series expansions are used to model end rotation and end moments which in turn are used to derive forces and moment equilibria in the plate. The author notes that delaminations further from the surface exhibit higher SERR for an equal applied strain. This essentially inhibits layers very close to the surface from propagating, something which was not concluded by Chai et [6] (with which a comparison is made) or other thin-film models. Delaminations further from the surface also exhibit a larger proportion of Mode-I in the Mode Mixity. Plate length was also studied and it was found that for large strains longer plates have higher energy release rates. Kardomateas and Pelegri [50] also derive criteria necessary to decide whether crack growth is going to be stable (increasing growth with increasing load) or unstable (crack growth occurs for constant load). The criteria identify sublaminate thickness (delamination depth), overall finite plate length, boundary conditions on the plate, post-buckling behaviour of the laminate and fracture toughness of the material from which the laminate is made. Comparisons are made with the thin film model predictions for stability of crack growth. The main conclusion is that the thin film model predicts that growth may be more unstable than it actually is.

Katerelos et al [25] derived a model that predicts the direction of delamination propagation under fatigue loading as well as the weakest interface. This is derived by considering the variation of strain energy release rate around an elliptical delamination. The model is compared to experimental results and is found to be in good agreement both in the prediction of propagation direction and also finding the weakest interface. Furthermore a power law, which is independent of initial impact energy, is derived to model the growth of the delaminated region under fatigue cycling.

Chen et al [51] derive a model using an open hole as the damage region for the compression after impact strength of composite laminates. Excellent agreement is shown with the results from test data using a range of materials. It is stated that this is the first model to use an open elliptic hole as an approximation of impact damage. The model also uses an unusual failure criterion derived by the authors based on assumption that failure occurred when 'stress in the 0^o plies in a composite laminate over some distance away from a notch was equal to or greater than the longitudinal ultimate tensile or compressive strength of a unidirectional laminate'. The authors report that: CAI is more greatly affected by in-plane stress redistribution than interlaminar toughness; notched laminate strength is not significantly affected by notch size parallel to the loading direction (a similar result for damaged laminates is assumed by the authors); damage area, impact energy, impactor shape and dimension can be represented by their effect on damage width. Zhuk et al [52] also had the idea of applying a model developed for open hole compressive strength to the problem of compression after impact behaviour of stiffened composite panels. The model is a combination of 3D stability theory for an undamaged panel and a maximum stress criterion and a fracture mechanics based model for the panel with an open hole. The model was found to agree well with FEA and experimental values reported in the paper. The authors note that location of the 0^o ply through the thickness of the laminate and the orientation of the plies supporting it can be critical in the initiation and final failure of stiffened panels. Finally it is suggested that this type of model should only form part of the final solution for calculation of the failure load, a second model considering out of plane buckling should also be applied and the minimum failure load should be taken as the lower of the loads suggested by the two types of model.

Whitcomb [26] presents a superposition model for the calculation of mode I and II energy release rates. The method is based on the simplification of the delaminated buckled region to the simple application of an axial force and a moment to the edge of the crack at the undelaminated region. The model gives loads for a range of delamination lengths and locations as well as for initial imperfections and mechanical and thermal loads. Validation is provided by comparison with FEA analysis. The author concludes that the magnitude of the mode I energy release is very sensitive to delamination length, initial imperfection and delamination depth. The sensitivity to these imperfections was also analysed.

Bruno and Grimaldi [53] consider both an analytical approach based on fracture mechanics and an FEA approach using unilateral springs to approximate the adhesion between layers to model delamination failure in two-layer plates loaded in compression. Both rectangular and circular plates are modelled. The authors note that the delamination process appears to be unstable for these problems and that the results for the two methods show good agreement.

Naik and Ramasimha [54] modeled the compressive strength of delaminated symmetric woven laminates as opposed to earlier work in this Chapter that covered angle ply laminates only. Woven laminates have advantages over non-woven and their static strength may need to be considered if they are to be implemented in components. Their method has three parts: ‘stress analysis of the laminate prior to the buckling of the sublaminate; eigenvalue analysis of the sublaminate; obtaining the compressive strength of the delaminated composite from these results’. An FEA analysis is performed to determine the stability of the sublaminate. The model was validated against a series of experiments and a good correlation was found. A parametric study considered the effects of delamination size and delamination depth on the compressive strength of the

laminate. The results of this study indicate that increasing the damage size causes a reduction in compressive strength and that the compressive strength of the delaminated composite 'decreases and then increases as the depth of delamination increases'.

At present to the author's knowledge no purely analytical model exists that predicts the static or fatigue CAI strength of composite structures to an acceptable degree of accuracy. A purely analytical model that is both accurate and computationally efficient that could be applied in a range of situations would be invaluable as a preliminary design tool for aerospace structures and is the overall objective for this work.

3.6. Finite Element Analysis methods

The alternative to an analytical model and one that has been widely explored in the literature is a Finite Element Analysis. This approach is not the one taken in this thesis however as although it is very accurate this comes at the expense of long computation times and long problem set-up times which makes this sort of modelling inflexible. Hence, FEA analysis should be a secondary choice as a preliminary design tool although its accuracy makes it a good choice for checking final stage designs. Despite FEA not being the approached used in this thesis a review of the literature that uses FEA is a useful and interesting exercise.

Tay [55] covers a wide range of papers on delamination in composites from 1990 to 2001. In particular some analytical advances used to speed up FEA computations are described and the advantages of differing elements and their application to a variety of problems in plates and shells are discussed. This is an excellent place to review developments in FEA theory up until 2001. The

papers below are selected from the period 2001 to the present and include applications to both plates and cylindrical shells. A number of FEA techniques are also considered but the most common approach amongst these papers is the crack closure technique (CCT) or virtual CCT (VCCT) descriptions of which are given below. However, an alternative technique was reported by Hawyes et al [56] who used an FEA cohesive zone model to predict the open hole compressive strength of laminated composites. They found the model to be a good predictor for CAI strength.

Ahn and Waas [57] used a micromechanics based FEA incorporating the J2 flow theory of plasticity (a name given to the application of the von Mises yield criterion which is based on the principle that yielding in 3-D occurs when the distortion strain energy reaches that required for yielding in uniaxial loading) and Halpin-Tsai relations to predict damage initiation in compressively loaded symmetric angle-ply laminates. The model captured the change in failure mode (from kink banding for low ply angles to a fibre-matrix interfacial failure for larger angles) and was in good agreement with experimental results. The main conclusion given by the authors is the fact that the limit load can be used as an indicator of the compressive strength of a laminate as it is independent of the size of the micro region (an area of intense stress inside the laminate which is modelled as alternating layers of matrix and fibres) chosen within the laminate.

de Moura et al [58] also used an FEA approach to model the residual compressive strength of composite laminates after impact. Their model used interface elements with contact penalties to model the crack in the laminate and solid elements for the rest of the laminate. The FEA results compared favourably with experiments and manage to capture the compression behaviour shown in the experimental work.

Nilsson et al [2] presented a combined FEA and experimental paper aimed at testing a moving mesh FEA scheme that allowed for contact between members. Excellent agreement was found between the results of the experiments and the FEA model for buckling, onset of delamination growth and evolution of delamination. The experiments were carried out for 35 ply cross-ply lay-up laminates with either no delamination or artificial delaminations inserted at 3, 5 or 7 plies from the upper surface using Teflon inserts. The FEA allowed for bending of both the base and sublaminate and used 'death-birth' contact springs that could alter stiffness as the area of contact changed. Dial-gauge forces were taken into account in the FEA and a number of different set-ups of the strain gauges were trialed in the experiments. It was found however, that the strain gauges inhibited laminates with a third ply delamination from buckling into an open mode so it was suggested that a non-contact laser instrument should be used. The conclusions of the paper centre on a comparison of a thin-film model and the FEA model. The authors concluded that the thin-film model will only be suitable for predicting delamination growth if it occurs at loads of 2/3 of the global buckling load or less. A second conclusion of note is that aircraft that may contain delaminations should not be allowed to globally buckle because the results of this paper point to failure occurring at loads at or just below the global buckling load. Hence an anti-buckling guide will be required for any experiments conducted for this thesis to avoid any global-local buckling interaction.

The following papers all used the CCT or VCCT technique. This technique is explained in the work by Riccio et al [59] who used Double Cantilever Beam (DCB) experiments to validate their FEA model for embedded delamination growth in composite panels under compressive load. The FEA model used a contact element which works on the penalty method where by some overlapping of elements is allowed but is opposed by a contact force F_C given by,

$$|F_C| = \alpha |GAP|$$

where GAP is the distance between elements and α is a penalty constant. Interface fracture elements are also used in the model and work on the VCCT, the principle theory of which is that it requires the same amount of energy to grow a crack some infinitesimal amount as it does to close the crack by the same amount. The VCCT is an approximation of the Crack Closure Technique (CCT) and is used as it requires only one step per computation as opposed to two for the CCT. The authors conclude that crack growth for specimens with delaminations near the surface is stable and that the FEA model compares well with the experimental data.

Chen and Sun [60] derived an FEA model for the residual compressive strength of delaminated plates. The model was based on first-order shear deformation theory and Von Karman's assumption. A 'modified crack closure technique' is used to calculate the SERR at each delamination front. A Tsai-Hill criterion was applied by the authors together with a stiffness degradation scheme to predict material properties after failure. All these theories were combined by the authors to produce a C computer model DAMAGE. DAMAGE does not appear to have been experimentally verified.

Shen and Tay [61] derived an FEA method based on the Virtual Crack Closure Technique VCCT for the calculation of the local SERR across the delamination front for post-buckled delaminated plates made of both woven and non-woven laminates. Both static and fatigue regimes are considered. The numerical results are validated with experiments and the following conclusions drawn by the authors: The direction of delamination growth generally coincides with

direction of maximum SERR which is significantly affected by sublaminate lay-up. The use of one quarter models for computational efficiency causes erroneous results due to the assumptions of symmetry conditions which do not reflect the true asymmetry of the real plates. This is confirmed by comparison in the paper of a full plate model and quarter plate model.

The final three papers reviewed in this chapter used a range of techniques to study curved and stiffened panels. Zhuk et al [62] presented an FEA model for determination of final failure loads for stiffened panels with delaminations placed in the skin away from the stiffeners. The authors reported a good correlation between their FEA model (based on the Stress Intensity Factor (SIF) and representation of impact damage as an open hole) and a purely analytical model. The calculation of the SIF requires calculation of the J-integral which is the same as the energy release rate. A conclusion is drawn that the presence of stiffeners has no effect on the correlation of the analytical model and the FEA model until the crack grows beneath the stiffener but this is not dealt with in this paper. The authors report good correlation with results for stiffened panels from the literature for two of three possible panel configurations with elliptical holes but suggest that for a third, which has longer bay widths, a soft inclusion model may be better as impact damage does not appear to be as severe as an open hole.

Asp and Nilsson [63] applied the DEBUGS (DElamination, BUckling and Growth Simulator) to model slender compression loaded composite panels with single embedded delaminations. The model of a stringer stiffened composite panel was found to be in good agreement with coupon tests. However, the authors warn that small geometrical variations were found to have a large effect on the behaviour of the panel and that care should be taken in allowing structures with delaminations to buckle as growth of these

delaminations is found to be promoted by global buckling. The site of the delamination combined with the mode shape of the buckle was also tested and it is suggested that a worst case scenario, where the delamination is placed at the point with the largest out of plane displacement, should be considered when designing components.

Yang and Fu [64] presented an FEA model which used the principle of moving boundary and Griffith fracture criterion to calculate energy release rates along delaminations in cylindrical shells. The authors concluded that delamination growth occurs more easily for increasing axial loads, delamination sizes and depths and for an increase in anisotropy of the materials involved. The boundary conditions also play an important role with delamination occurring more easily for simply supported cylindrical shells than for cylindrical shells with clamped ends.

3.7. Review of optimisation techniques

A range of optimisation procedures are reviewed which optimise laminates for a number of conditions including buckling resistance and weight. The most interesting appears to be an optimisation procedure by Herencia et al [65] which allows for constraints imposed by elastic tailoring. A summary of the paper is given below.

Herencia et al [65] used lamination parameters and a two stage process to optimise long anisotropic composite laminate panels with T shaped stiffeners for weight reduction. Different geometric constructions of the T stiffener are considered in the results. The first level of optimisation carried out uses lamination parameters and this is followed by a second stage which employs a genetic algorithm. Laminates are optimised under various constraints, in particular, owing to manufacturing constraints, ‘skin and stiffener laminates are

assumed to be symmetric or mid-plane symmetric laminates, with 0, 90, 45, or -45 degree ply angles'. The main difference between the approach adopted here and other papers is the 'inclusion of membrane and flexural anisotropy for elastic tailoring purposes' as well as the manufacturing constraints mentioned earlier. Results indicate that a weight reduction of about 2.7% is possible under a reduced constraint set when compared to results from the literature. However, if full design constraints are applied a weight penalty of 2% is introduced. It is also noted that the authors consider the computational cost associated with the genetic algorithm to be acceptable.

Adali et al [66] described the results of an optimisation procedure for 'shear deformable rectangular plates' under compressive loading that used ply angle to optimise laminates for maximum failure load. This failure load generally takes the form of the buckling load for thinner laminates or material failure load for thicker laminates. However both are considered for all laminates by the optimisation procedure and the lower of the two is taken as the failure load. Results were presented that consider the effects of various ratios of length, width and thickness of the laminates on the failure loads and optimal ply-angles are given in each case.

In the work by Adali et al [67] symmetric balanced laminates were placed under either uniaxial or bi-axial loading and then optimised using both continuous and discrete ply angles. The laminates were optimised for buckling and post-buckling stiffness and buckling load using the design index *DI* given as,

$$DI = \mu_1 K^* + \mu_2 N^* + \mu_3 P^*$$

where *K** is the pre-buckling stiffness, *P** is the initial post-buckling stiffness and *N** is the critical buckling load. μ_1, μ_2 and μ_3 are weightings given to the optimisation parameters to allow for differing objectives in the optimisation. The resulting laminate with the highest *DI* is considered to be the optimal one. For optimisation using continuous ply angle 'candidate laminates' are required and it is these that are optimised. Numerical results are given for example laminates and conclusions drawn. The most interesting of these is that post-buckling stiffness seems to be particularly sensitive to changes in ply angle in fact "within about 3^o change of the ply angle, the post-buckling stiffness may drop as much as 50%".

Diaconu and Weaver [68] considered infinitely long composite laminate plates in the post-buckling response region. Lamination parameters are first used to model the problem and then to choose optimised laminates. Good agreement was found between the lamination parameter solution and an FEA solution for the post-buckling model. Optimisation is undertaken first using continuous laminate configurations which produce optimised laminates for minimising 'maximum transverse displacement' and 'applied strain'. These are then compared to laminates produced using more realistic discrete laminate configurations. The comparison between the two is good with very little optimisation lost making the layers discrete.

Wiggenraad et al [69] reported on the optimisation procedure PANOPT. They provide results for three variations of stiffened panels. One is a base line configuration and the other two panels are optimised by PANOPT to be damage resistant. The peak force in impact is used as a damage initiation criterion and found to be accurate for stiffener foot impacts and conservative for mid-bay impacts. The authors note that due to this conservativeness in prediction of mid-bay impacts it is stiffener foot impacts that should be the future design drivers for damage resistance. It is shown that

the optimised panels offer better damage resistance than the baseline configuration but only at a weight penalty of 16-28%.

Summary

A lack of computationally efficient modelling capability with acceptable accuracy has led to NDT being identified as the most efficient way to describe impact damage morphology.

A current lack of efficient accurate analytical modelling capability that would be suitable for preliminary design work has been established and hence this an area for where research can and should be conducted.

VICONOPT has been identified as the most computationally efficient approach for calculating sublaminate buckling strain fulfilling objective 2.

No work has been identified that proposes laminate stacking sequences that maybe considered damage tolerant. Thus this is identified as an area in which original research can be undertaken.

4. Damage morphology

Barely visible impact damage has a very complex structure composed of delaminations and inter-ply and intra-ply cracks, see Figs 1 and 2. The composition of BVID and in particular the distribution and size of delaminations for individual coupons is certainly both stacking sequence and impact energy dependent and to some extent can vary in geometry for individual coupons with the same lay-up.

Complex FEA models reconstructing damage morphologies such as those in Fig. 1 require substantial development and once produced have long computation times [69] which conflicts with the principle of this work which is to produce a time-efficient preliminary design model for predicting damage tolerance of composite laminates containing BVID. Thus attention is turned to simplification of the damage morphology in order to produce time efficient models. An approach used by a number of researchers [3, 8] is to approximate delaminations through the thickness using circles or ellipses while generally ignoring intra-ply cracks. This is the approach considered here.

The four damage models presented in this Chapter have the aim of capturing as simply as possible the state of the volumetric region in and around the BVID as delamination propagation occurs. Each model represents the complex morphology, captured via C-scan see Fig. 1, associated with BVID for a different combination of loading (fatigue or static) and component (plate, stiffened panel, or stiffener) using a single circular or semi-circular delamination at each ply-interface. Note that all four models only consider interfaces in the 20% of laminate thickness closest to the surface (generally the non-impact face) as the critical

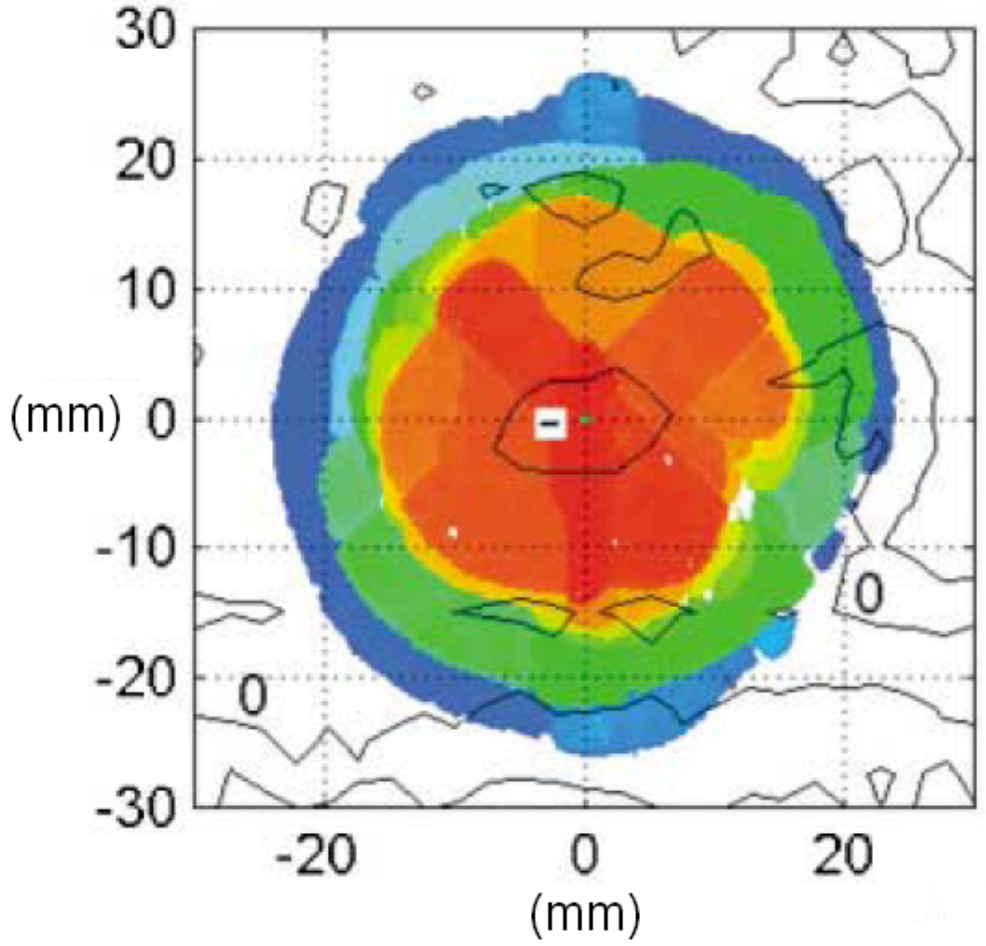

Fig. 1. C-scan and contour map from [7]. Colours give a qualitative indication through thickness position of individual delaminations. Negative contours denote deflection towards the back face.

delamination, the delmination at which damage propagation initiates, is assumed to occur in this region. This reflects observations made by Melin and Schon [8] and is consistent with critical delamination depths reported by Butler et al [5] and Greenhalgh et al [14].

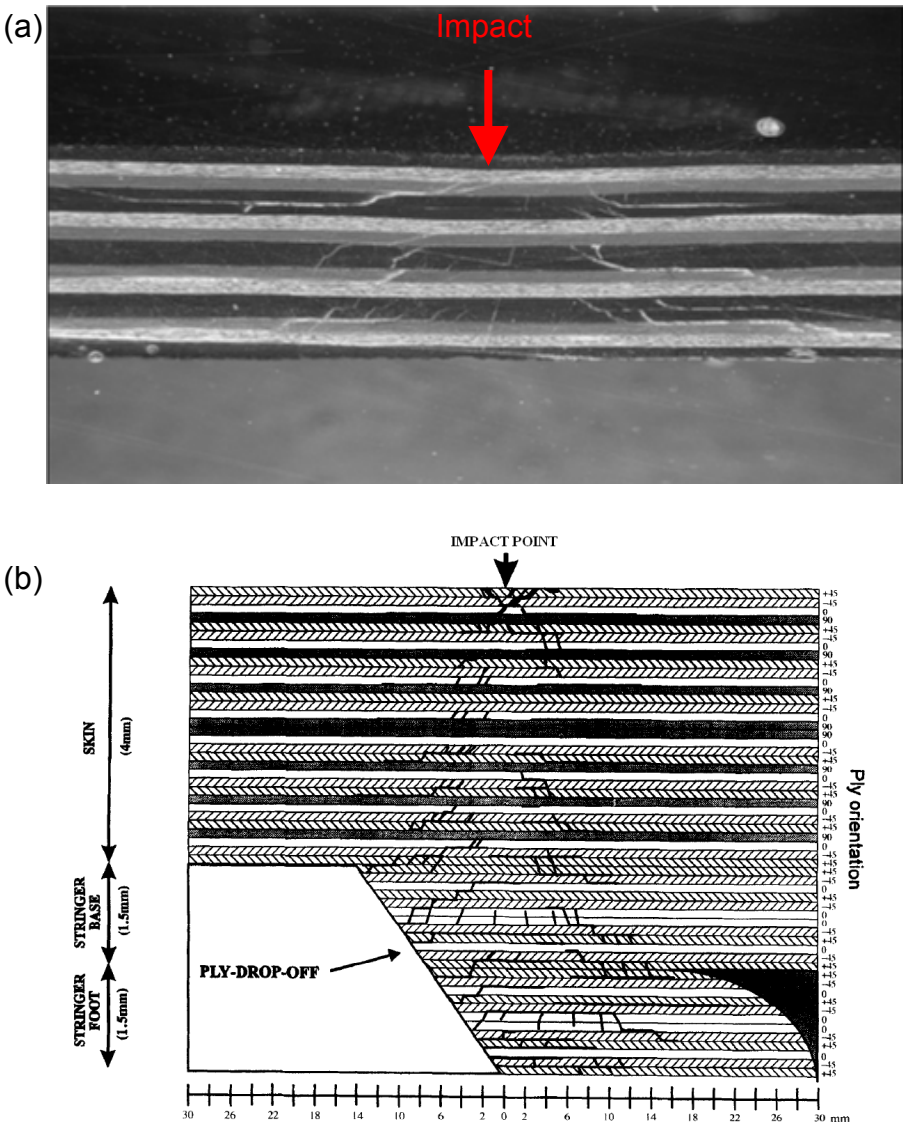

Fig. 2. (a) BVID in a cross sectional image showing delaminations in a coupon following an impact normal to the top surface taken from [14]. (b) Schematic diagram of BVID resulting from impact on a stiffened panel under a stiffener foot taken from [71].

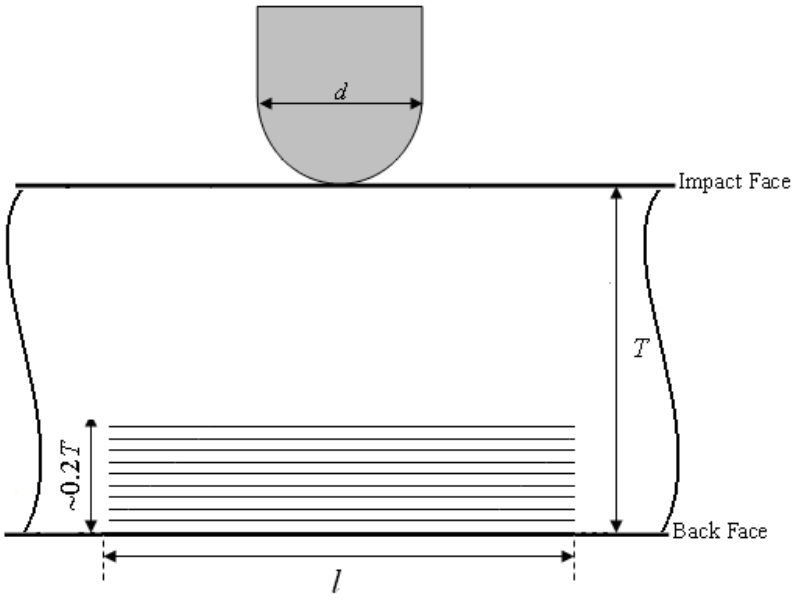

Fig. 3. CDM model of through thickness damage diameter distribution

4.1. Constant Damage Model (CDM)

Before final failure occurs, and for most of a coupons life under fatigue loading, BVID remains within its initial area. It is only the final stages of fatigue loading, when delaminations at a significant depth within the sample have buckled and subsequently opened, that cause the damage to propagate from the initial site. This increasing area of damage can lead to widespread delamination and subsequent failure of the component.

The Constant Damage Model (CDM) (see Fig. 3) is employed for a fatigue loading regime in flat plates and is designed to capture the above conditions apparent in the final stages of fatigue damage growth. Hence, it is assumed that the damage at every interface has spread to the boundary of the initial damage which is itself approximated by a circle with diameter $l_{\max}$ that contains the full damage footprint as seen on a C-scan, see Fig. 4.

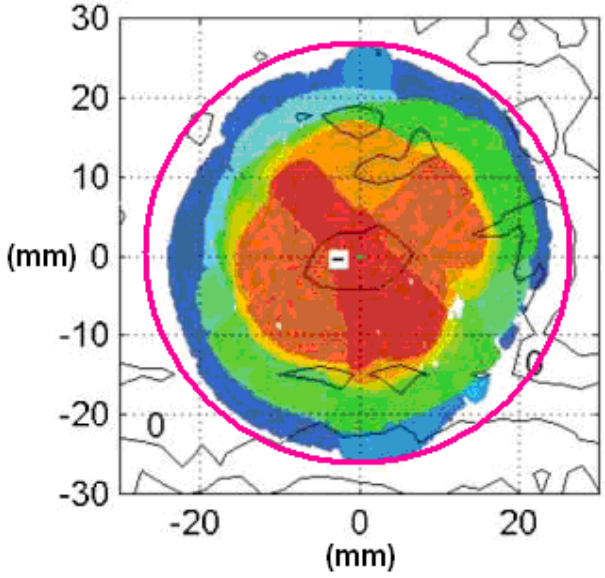

Fig. 4. Plan form C-scan image from [7] showing circle of diameter $l_{\max}$ approximating the plan form damage.

4.2. Linear Damage Model (LDM)

Unlike fatigue loading where cycling of the loading causes damage to consolidate, a range of different sized circular delaminations are required at various depths within the laminate, as can be seen from Fig. 5 (reproduced from [13]), to describe the initial conditions for the damage morphology present in plates prior to failure induced by static loading.

Figure 6 (a) shows a linear damage model based on a distribution of circular delaminations reported by Uda and Ono [13], see Fig. 5. The diameters of circular delaminations in the lower 20% of the laminate thickness in Fig. 5 can be approximated by assuming a linear decrease in diameter away from the largest delamination toward the back face of the laminate. A similar relationship can be inferred from

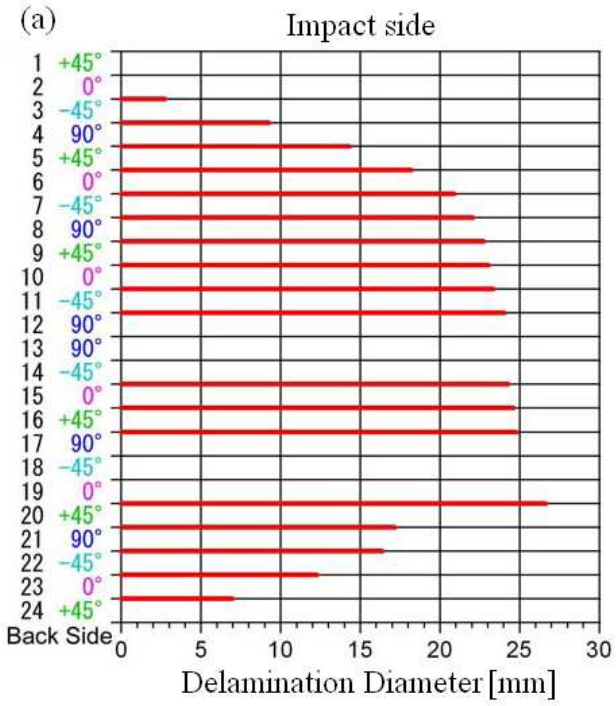

Fig. 5. Sectional view of damage from [13] showing diameters of circles approximating through-thickness damage obtained from C-scan.

Hull and Shi [72] who relate the formation of damage in this region of the laminate to bending of the laminate and peeling of the back face ply.

The delamination corresponding to the largest delamination $l_{\max}$, approximated by a circular delamination of diameter equal to that of a circle that contains the plan view of damage on a C-scan, see Fig. 4, is assumed to occur at 20% of laminate thickness *T*. Damage circles then decrease in diameter linearly so that the final diameter l_b corresponds to the delamination closest to the back face. This configuration of damage with $l_{\max}$ at 20% gives the most conservative approximation to damage while maintaining the 20% critical region. There are many factors affecting the size of individual delaminations including laminate thickness, stacking sequence, tup size and

support conditions. However, as most impact tests are conducted using official standards, boundary conditions are generally consistent and have a limited affect here. Thickness affects the level of energy required for BVID but has limited effect on individual delaminations unless the coupon is very thick such as is the case for impacts under a stiffener foot in which case delamination tends to accumulate near the impact surface. Stacking sequence has a complicated affect on BVID via varying interlaminar stiffness and so considering it would defeat the objective of developing a simple approximation to damage. Hence, It is assumed that this delamination is strongly influenced by bending associated with the geometry of the tup, thus an empirical rule, based on [13] and Fig. 5 is assumed whereby a tup of diameter 12mm causes an outer ply delamination of 7mm. Hence for the general case the delamination of diameter l_b closest to the back face, is determined assuming,

$$l_b = \frac{7d}{12} \tag{1}$$

where d is the diameter of the tup used to impact the laminate, see Fig. 6.

The above is based on damage in coupons. In order to approximate initial conditions in stiffened panels under static loading such as the one described in Chapter 7.2 some alterations are required. For impacts to the panel underneath a stiffener foot Greenhalgh et al [14] found impacts caused damage throughout the skin and stiffener, hence it is assumed that the stiffener can be represented by a laminate of equal thickness and identical lay-up to the stiffener foot.

The panel is modelled as a laminate consisting of the laminate representative of the stiffener foot combined with a laminate representative of the skin. In addition, assuming an impact on the skin surface, the circle of largest diameter is positioned at a distance of 20% of total thickness (skin thickness + stiffener foot thickness) away from the impact face rather than the back face see Fig. 6. When considering impacts to the bay between stiffeners, where the laminate is the same thickness as the skin, the LDM can be applied as it would be for a laminated plate.

Finally, note that a circular approximation of damage is chosen in general for the following reasons. Firstly, for simplicity, especially regarding the orientation with respect to ply angle that would be necessary for shapes with few or no axes of symmetry. Secondly, provided damage is fully contained in the cylinder or cone, circles will always give a conservative and hence safe estimate of the area and associated buckling strain.

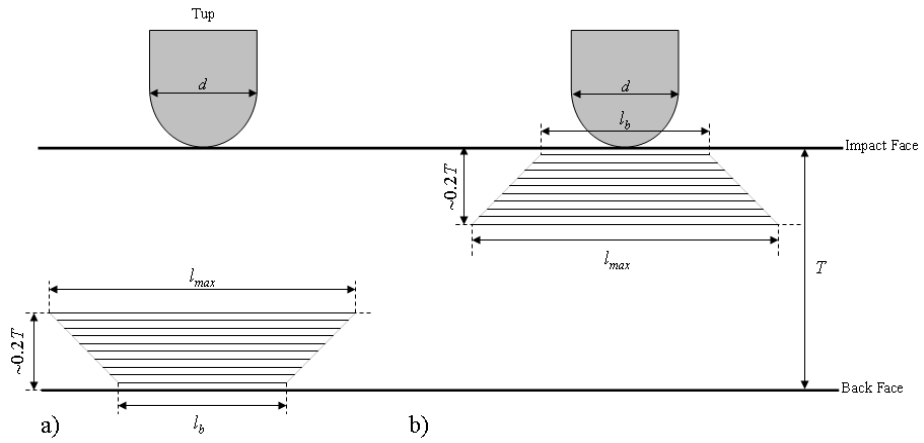

Fig. 6. Linear damage model for static strength showing, tup impactor, and assumed delamination distribution over 20% of laminate thickness for (a) plates under and (b) stiffened panels impacted under a stiffener foot.

4.3. Experimental Damage Model (EDM)

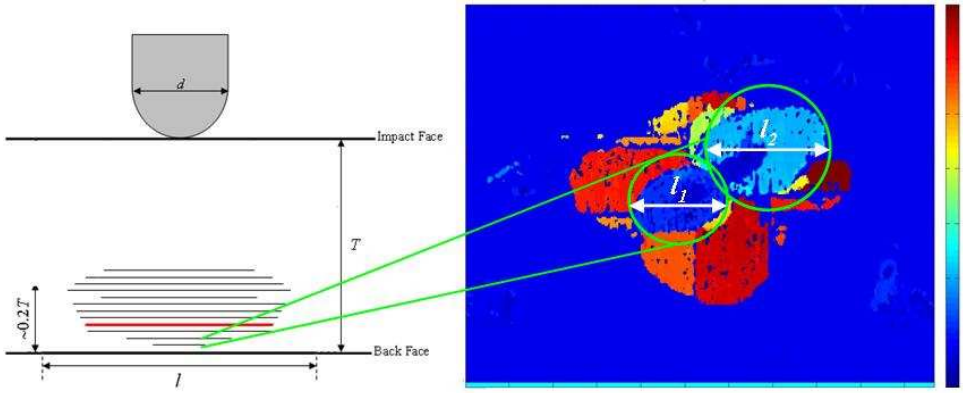

Fig. 7. The Exact Damage Model (EDM) uses circles that contain the delamination area at each individual interface.

The Experimental Damage Model (EDM) (Fig. 7) uses accurate ultrasonic time-of-flight C-scan information which includes delamination depth measured from the outer face to provide more precise delamination diameters for each interface. In particular, the through-thickness information used in this model allows individual delaminations to be placed at the correct interfaces which produces an improvement in accuracy.

(Note though that due to issues with ‘shadowing’ where near surface delaminations block the C-scan from detecting deeper delaminations the EDM approach may appear un-conservative. However, the EDM is conservative in another way as individual delamination diameters are chosen so as to contain the full area of delamination within a circle. This can result in a much larger circular area than a C-scan image of the damage suggests which can lead to reduced delamination buckling strains).

4.4. Free edge in-plane impacts

C-scan images of stiffener sections that have been subjected to on edge in-plane impacts (see Fig. 8 (a) and (b)) show that the full damage area has a clear semi-elliptical shape. Hence, the model uses this shape to approximate the complex BVID morphology that is produced following low velocity impact, see Figs 9 (a) and (b).

Identical semi-ellipses, with major and minor axes *a* and *b* respectively, are applied at the meeting of each interface where delamination is possible i.e. interfaces that separate plies of different orientations where fibre bridging is unlikely to occur. The use of identical ellipses which contain the full damage area ensure an

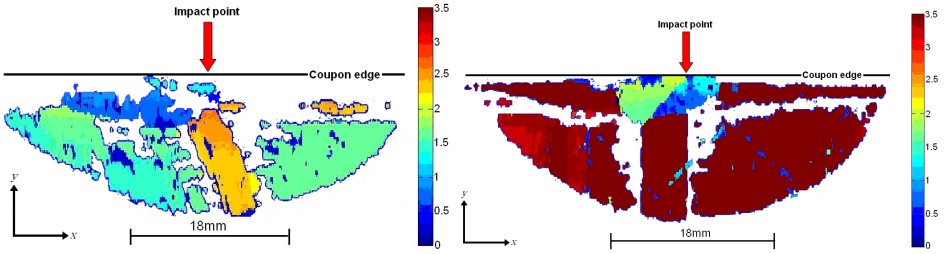

Fig. 8. C-scan images of (a) coupon with 11J BVID and (b) 10J-*a* coupon with 10J BVID. Colours show a qualitative indication of through thickness position of delaminations.

overestimate of the actual damage at any particular interface and hence conservativeness. Note in Fig. 8 that the compressive (CAI) load is applied in the *x*-direction.

Summary

Four damage models have been created that use NDT representations of damage morphology to produce through thickness delamination distributions. The models cover damage distribution in enclosed and free edge delamination problems including damage in

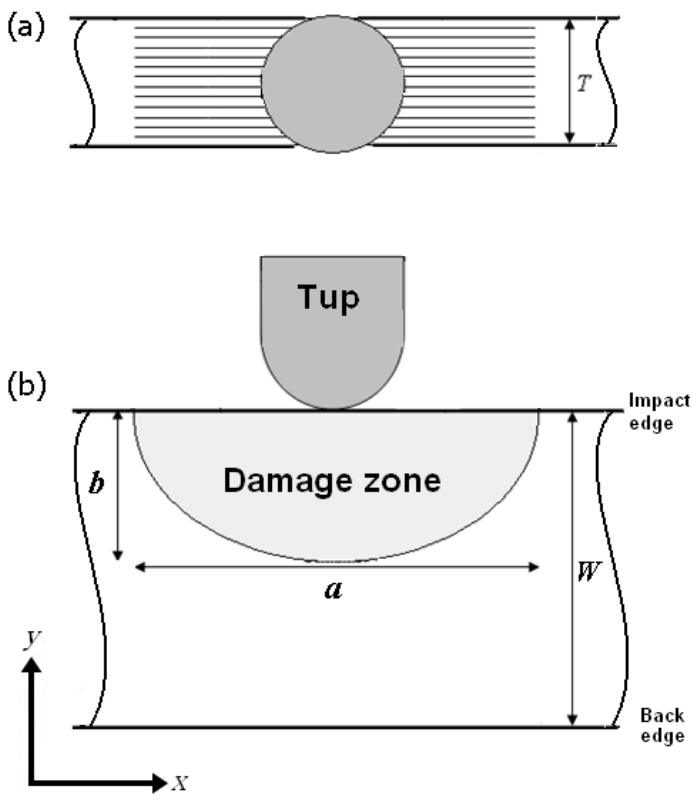

Fig. 9 (a) and (b) show plan and side views respectively of the damage model where *T* is laminate thickness and *W* is coupon width.

stiffeners and stiffened panels. The models require only very simple (if any at all) algebraic computation and thus the first objective of this thesis, to produce damage models that are computationally efficient, is fulfilled.

5. Sublaminate buckling

The overall concept of the thesis is to model the process of delamination buckling propagation. Fig. 10 describes the BVID situation treated by the model. The top layer over the delamination in each image is referred to as the sublaminate and will be the section that buckles and causes propagation.

The key process in propagation of damage under compressive loading is local buckling of the sublaminate above a delamination at some critical through thickness position. Calculation of this critical position and the corresponding level of strain required to cause damage propagation is the topic of the following chapter. Here the methods used to calculate the sublaminate buckling strain associated with each of the various problems tackled in this thesis is described. The first sub-section deals with the transfer of load from the base

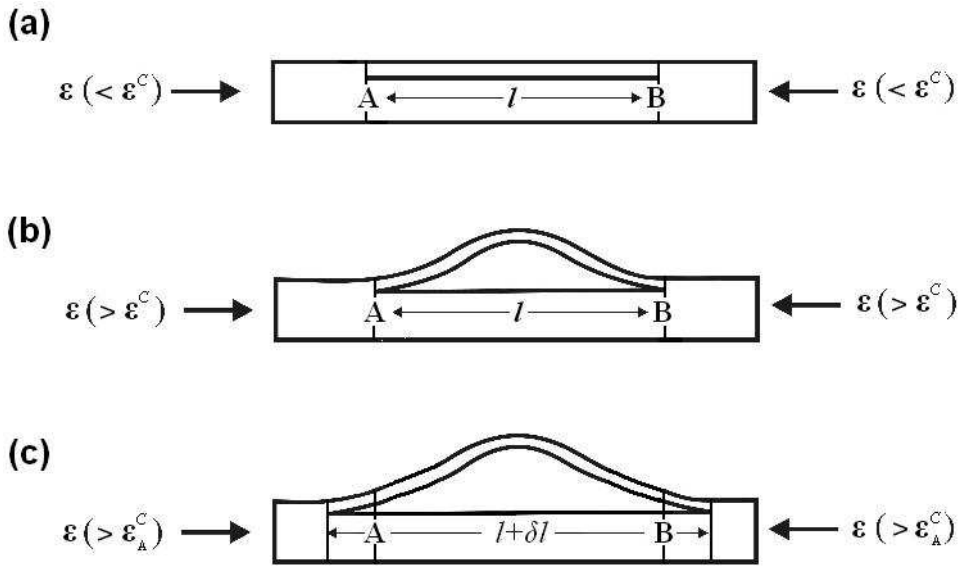

Fig. 10 Overview of the three stages in delamination buckling propagation. (a) Flat, pre-buckled state, (b) post-buckled state and (c) post-buckled propagated state.

laminate to the delaminated sublaminate which has direct consequences for the calculation of the critical sublaminate buckling strain which is addressed in the second subsection.

5.1 Loading

Here consideration is given to the transfer of load from the full laminate to the delaminated sublaminate and the issues of compatibility between the two. The full laminate stiffness matrix is given by,

$$\begin{Bmatrix} N_x \\ N_y \\ N_{xy} \\ M_x \\ M_y \\ M_{xy} \end{Bmatrix} = \begin{bmatrix} A_{11} & A_{12} & A_{13} & B_{11} & B_{12} & B_{13} \\ A_{12} & A_{22} & A_{23} & B_{12} & B_{22} & B_{23} \\ A_{13} & A_{23} & A_{33} & B_{13} & B_{23} & B_{33} \\ B_{11} & B_{12} & B_{13} & D_{11} & D_{12} & D_{13} \\ B_{12} & B_{22} & B_{23} & D_{12} & D_{22} & D_{23} \\ B_{13} & B_{23} & B_{33} & D_{13} & D_{23} & D_{33} \end{bmatrix} \begin{Bmatrix} \varepsilon_x \\ \varepsilon_y \\ \gamma_{xy} \\ k_x \\ k_y \\ k_{xy} \end{Bmatrix} \quad (2)$$

where the A_{ii} are in-plane stiffness', D_{ii} are bending stiffness' and B_{ii} are coupling stiffness' with subscripts defining stiffnesses in the principal (1), transverse (2) and out-of-plane (3) fibre directions. $\{N\}$ are the loads acting on the laminate, $\{\varepsilon\}$ are the in-plane strains acting on the laminate, $\{M\}$ are the moments acting on the laminate and $\{k\}$ are the curvatures of the laminate with subscripts denoting longitudinal (x), transverse (y) and shear directions (xy) respectively.

Note only balanced laminates are considered as the parent laminates for the sublaminates considered in later sections. For the enclosed circular delamination seen in face impacted plates, and approximated by the LDM and EDM, assuming zero curvature in the balanced parent laminate**,** the loads acting on the delaminated plate $\{N\}_D$ are

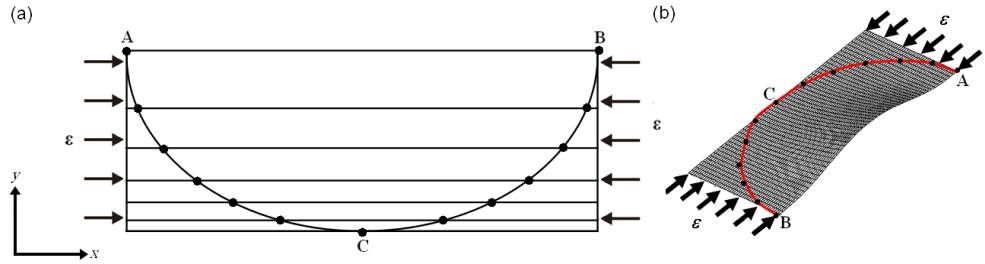

Fig. 11 (a) Shows the distribution of nodes and strips in the VICONOPT buckling model. (b) Shows the buckled shape of the sublaminate.

determined by obtaining the strain $\{\varepsilon\}_L$ of the full parent laminate when unit axial strain is applied. $\{N\}_D$ is then calculated, by assuming compatibility of strain from,

$$\{N\}_D = [A]_D \{\varepsilon\}_L \tag{3}$$

i.e.

$$\begin{Bmatrix} N_x \\ N_y \\ N_{xy} \end{Bmatrix}_D = \begin{bmatrix} A_{11} & A_{12} & A_{13} \\ A_{12} & A_{22} & A_{23} \\ A_{13} & A_{23} & A_{33} \end{bmatrix}_D \begin{Bmatrix} \varepsilon_x \\ \varepsilon_y \\ \gamma_{xy} \end{Bmatrix}_L \tag{4}$$

where $[A]_D$ is the in-plane membrane stiffness matrix of the delaminated plate. Note that although uni-axial load is applied to the full laminate, Eq. (2) may result in bi-axial load and shear being applied to the delaminated plate.

For the free edge case with semi-elliptical damage geometry three separate initial conditions are considered that approximate load transfer from the full laminate to the sublaminate in different ways. All three conditions assume zero curvature in the full laminate. The first initial condition denoted $\varepsilon_y = \varepsilon_{y-L}$, represents the boundary conditions at points A and B in Fig. 11 where the sublaminate is still attached to the base laminate and hence compatibility of strain is required. This condition assumes that the load due to Poisson's ratio strain in the full laminate is transferred to the sublaminate. Consequently, the loads acting on the delaminated plate $\{N\}_D$ are determined by obtaining the strain $\{\varepsilon\}_L$ of the full laminate when unit axial strain is applied. The $\{N\}_D$ are then calculated by assuming compatibility of strain from Eq's. (3) and (4). Note that although uni-axial load is applied to the full laminate, Eq. (3) may result in bi-axial load and shear being applied to the delaminated plate.

The second initial condition denoted $N_y = 0$, assumes there is no load along the free edge of the sublaminate i.e. no load/restraint is transferred from the base (the lower part of Figs. 10 (b) and (c)) to the sublaminate in the direction transverse to the applied compressive strain ε.

The third initial condition involves setting $\varepsilon_y = 0$ in Eq. (4) which gives an increase in stiffness in the load direction and essentially prevents any change in the width of the plate due to Poisson's ratio effects during loading. Physically, this is equivalent to holding the free edge completely rigid in the transverse direction and approximates the conditions beneath the clamps at the end of a rigidly held test piece.

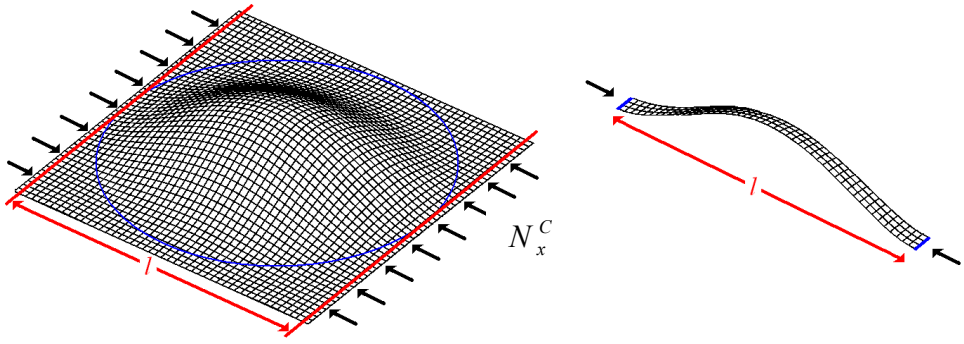

Fig. 12. (a) Plate buckling mode with clamped circular boundaries and critical load N_x^C. (b) Beam buckling mode with clamped transverse boundaries and critical buckling load $N_x^C = 4\pi^2 D_{11}/l^2$.

5.2 Buckling model

An essential difference between the model introduced here and the earlier 1D model by Butler et al [5] is the boundary conditions placed on the delamination buckling region, as illustrated in Fig. 12. The 1D bending case, Fig. 12(b), is described by a single fourth order ordinary differential equation in one direction which allows only four conditions to be placed on the transverse boundaries, in this case clamped conditions at $x = 0$ and $x = l$.

This leaves the longitudinal boundaries unrestrained which is an unrealistic representation of what happens to the plate under compression, particularly when fibres within the laminate are aligned in $\pm$ 45^o or 90^o directions. For enclosed delaminations Fig. 12(a) is a better representation because it takes into account the effects of transverse bending and twisting moments. A consequence of this derivation is that the effect of the circular boundary is taken into account. Similarly, for free edge delaminations Fig. 11 gives a two dimensional representation of the delamination boundary.

The propagation model requires the calculation of the buckling strain ε^C of the delaminated circular region. The process of calculating ε^C is described below and is reliant on the composite buckling program VICONOPT written by Williams et al [34] which has been validated for calculation of local buckling loads of sublaminates in [9,73,79]. An example input file with explanation can be found in Appendix I and a detailed description of the theory behind VICONOPT can be found in [32] and [33]. However essentially, the governing differential equations for composite plates with simply-supported end conditions,

$$\frac{dn_x}{dx} + \frac{dn_{xy}}{dy} - \frac{dN_x u_0}{dx^2} - K_x u = 0 \tag{5}$$

$$\frac{dn_{xy}}{dx} + \frac{dn_y}{dy} - \frac{dN_x v_0}{dx^2} - K_y u = 0 \tag{6}$$

$$\frac{dq_x}{dx} + \frac{dq_y}{dy} + K_z w - N_x \frac{dw}{dx^2} - N_y \frac{dw}{dy^2} - 2N_{xy} \frac{dw}{dxy} = 0 \tag{7}$$

$$\frac{dm_{xy}}{dx} + \frac{dm_y}{dy} - q_y - N_x z_c \frac{dv_0}{dx^2} = 0 \tag{8}$$

$$\frac{dm_x}{dx} + \frac{dm_{xy}}{dy} - q_x - N_x z_c \frac{du_0}{dx^2} = 0 \tag{9}$$

where (u,v,w) are displacements in the (x,y,z) directions respectively with (u_0,v_0) being the in-plane displacements from the centroidal cross-section of the plate, z_c is the distance from the centroidal plane of the cross-section of the plate, (N_x,N_y,N_{xy}) are pre-buckling in-plane loads, (n_x,n_y,n_{xy}) and (m_x,m_y,m_{xy}) are buckling in-plane forces and moments respectively, (q_x,q_y) are transverse shearing forces and (K_x,K_y,K_z) are elastic Winkler foundations are solved exactly [33] by assuming sinusoidal variations of the buckling

deformation in the longitudinal direction resulting in an eigenvalue problem involving a transcendental stiffness matrix. A novel algorithm is employed which calculates the eigenvalues of this matrix by determining changes in polarity of the determinant and interpolating to the correct value. These eigenvalues are the load factors for the buckling problem. For problems with more complex end conditions [32], and significant shear loading or anisotropy, it is necessary to use multiple sinusoidal variations combined using Lagrangian multipliers to avoid being overly conservative. In this way consistency with nodal point constraints, such as shown in Fig. 13, is achieved. Note that although the structure remains prismatic and the solution remains longitudinally periodic the position of supports can be staggered width-wise to approximate a circular boundary.

With regard to the implementation in VICONOPT, the delaminated plate is modelled as a thin film such that the plate boundary along the curved perimeter of the delamination is assumed to be constrained. The program models the plate as a series of finite strips, the edges of

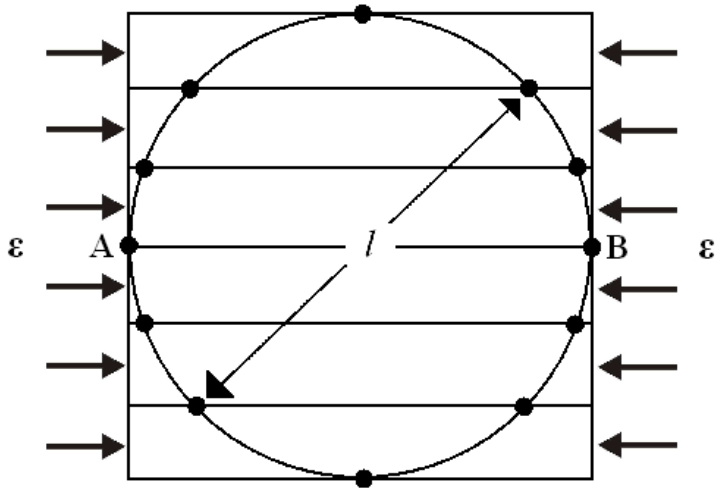

Fig. 13. Thin film model showing a plan view of circular delaminated plate of diameter l with nodes and strips to illustrate VICONOPT discretisation.

which are constrained by nodes approximating a circular boundary or in the case of the edge impact; separated by equal arc-length, approximating a semi-elliptical boundary and a free edge, see Figs. 11(a) and (b). For the results presented later, 6 equal width strips were used with 12 constrained nodes at the junction of these strips and the delamination boundary (for the effect of altering the number of strips see [73] and Chapter 7.1).

Here, for enclosed delaminations (such as those described in Figs. 12(a) and 13) constrained implies in and out-of-plane displacements and rotations are constrained at the nodal points. For free edge problems constrained implies in-plane rotations and out-of-plane displacement are constrained (depending on the initial conditions and load transfer being imposed) at all nodal points. However in-plane displacement is only constrained at a single point (point C Fig. 11(a)) to prevent unrealistic in-plane buckling.

Note that, to obtain ε^C, VICONOPT uses the loadings placed on the thin film by axial compression of the full laminate. For the free edge problem, in reality, the loads will vary along the length of the laminate, since compatibility only induces restraint where the boundary of the delamination intersects the free edge, i.e. points A and B of Fig. 11. However VICONOPT assumes invariant loading along laminates. VICONOPT buckling analysis has been previously validated for circular buckles, see [9, 73, 79].

Summary

The principles of load transfer from the base laminate to the delaminated sublaminate and the associated boundary conditions have been described for enclosed and free edge delaminations.

The advantage of using the two dimensional buckling calculation made in VICONOPT over the one dimensional model of Butler et al [5] has been shown.

Implementation of the boundary constraints for enclosed and free edge problems in VICONOPT has been described with the reader being referred to an example input file in Appendix I.

In line with aim 2 of Chapter 2 a computationally efficient way of calculating the critical buckling strain of a delaminated sublaminate has been established.

6. Propagation model

The static propagation problem was addressed by Chai et al in [6]. They produced a simple 1D propagation model based on beam theory with the simplifying assumption that all the layers in the laminate were homogenous and isotropic. A 2D initial buckling model for multiple delaminations has been derived using a Rayleigh-Ritz formulation by Suemasu et al [49] and a similar 1D Rayleigh-Ritz model by Hunt et al [30] drew attention to the concept of a critical depth of delamination in the context of post-buckling response. More recently, Butler et al [5] presented a new method for compressive fatigue which included anisotropy and was based on a combination of 2D finite strip buckling and 1D beam propagation, where the complexity of the morphology and propagation of damage was represented by the energy requirements for final stage static growth of a single delamination at a critical depth within the sample. The propagation model presented here is an extension of the model from [5] with the novelty being in the use of VICONOPT to determine the buckling strain and the introduction of the axial stiffness of the sublaminate A_{11} as a problem parameter. It assumed in the modelling that the plate in which the delaminations are contained is of sufficient size so that clamped boundaries do not inhibit the growth of the damage nor effects associated with the edge of the plate interacting with the damage except in the case of free edge delamination where this is an intrinsic part of the problem which is allowed for in the choice of boundary conditions. Problems against which the model is validated in Chapter 7 are chosen so as to fulfill these assumptions.

It is intrinsic to the derivation of the propagation model that propagation of damage is assumed to initiate in the direction of compressive load. However, no prediction as to the subsequent

direction(s) of growth after initial propagation occurs, although stability of this growth is analysed in later sections. Experimentally, Fig. 19 in [74] directly supports initiation of growth in the loading (longitudinal) direction and images from Melin and Schön [8] and Melin et al [12] display growth in the same direction although it is not apparent in which direction, longitudinal or transverse, propagation first occurred. Analytically, Chai and Babcock [3] show that it is possible for growth to initiate in the longitudinal direction for isotropic and orthotropic sublaminates, depending on the geometry and depth of the critical delamination. Anisotropy however, was not studied by Chai and Babcock in [3]. Images from a model developed by Suemasu et al [74] also indicate propagation initiating in the loading direction. Note that in reality direction of growth in a flat plate is controlled by the sublaminate stacking sequence and the overall plate boundary conditions (particularly in stiffened panels where the stiffer boundary offered by the stiffeners affects growth direction) influence growth direction, but as growth forms as an area some growth in the load direction will always be required.

The principle of the model is to find the threshold strain ε_{th} below which propagation of the delamination damage will not initiate (i.e. a lower bound). The model does not predict the strain at final failure, nor indeed the mode of propagation. However, it is assumed that the impact damage problems to be modelled will fail by delamination buckling leading to propagation of damage away from the original site. This precludes problems where the initial mechanism of failure is via kink banding or buckling of the full laminate.

The central concept of the derivation is to find the difference in energy in the post-buckled sublaminate before, Fig. 10 (b), and after, Fig. 10 (c), the growth of a delamination and to compare this difference to the Mode I fracture energy required to create a new unit of delamination. If sufficient energy is available then a new unit of delamination is created and propagation of the delamination will

occur. Note that l is the (projected) length of the sublaminate immediately before propagation, and δl is an infinitesimal length associated with the length change due to propagation. Although this length change is shown along the free edge in Fig. 10, it relates to any length change in the direction of applied load. The propagation model is applied at each interface derived from the relevant damage model. Hwang and Liu [7] note that for the case of enclosed delaminations, multiple delaminations which are representative of impact damage, can be approximated by a single delamination at a critical interface. The same principle is assumed to hold here. Thus at each application it is assumed that only the delamination being examined is present in the laminate and that all secondary effects (i.e. friction between delaminated layers) relating to multiple delaminations being present in the laminate are ignored.

The derivation itself will be divided into two parts; the first dealing with energies associated with unit width of the sublaminate of length l and the second dealing with the region of length δl.

In order to calculate the energy due to bending in the delaminated region it is assumed that the bending energy stored exactly equals the in-plane or stretching energy released (see p.171, [29]). The energy released laterally is small hence it can be assumed $\varepsilon_y = \varepsilon_{xy} = 0$ and the bending energy per unit width U_1 is,

$$U_1 = N_x^C l(\varepsilon - \varepsilon^C) \tag{10}$$

Where N_x^C is the critical buckling load of the delaminated sublaminate. Hence, Eq. (4) gives,

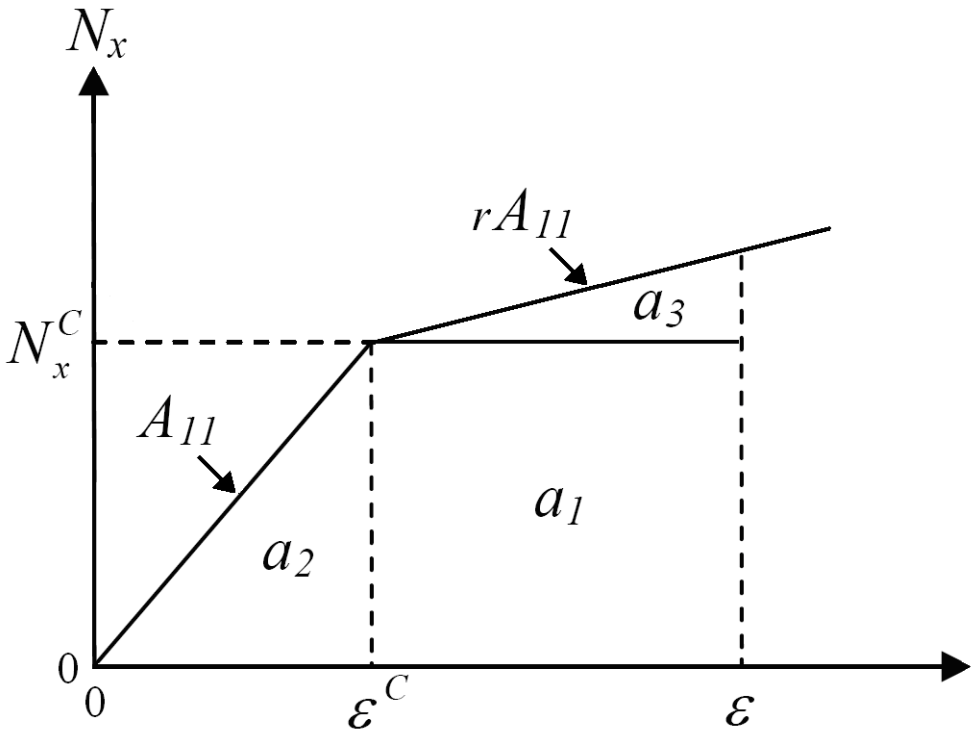

Fig. 14. Strain energy in a post buckled strip at axial strain ε. N_x is axial load per unit width, a_2 and a_3 integrated over the strip length l, are equal to U_2 of Eq. (23). Area a_1 represents U_1 of Eq. (10)., where the latter is the bending energy of the delaminated plate.

$$U_1 = A_{11}\varepsilon^C l(\varepsilon - \varepsilon^C) \tag{11}$$

Where A_{11} is the axial stiffness of the delaminated sublaminate i.e. the post buckled region of Fig. 10 (b) and (c). An alternative approach is to consider the area a_1 of Fig. 14 which gives the energy due to end shortening in the standard buckling regime.

In order to allow for variation in buckling strain due to the change in length caused by propagation consider the critical buckling strain for an Euler strut,

$$\varepsilon^C = \frac{\pi^2 I}{Al^2} \tag{12}$$

where A and I are the cross-sectional area and second moment of area, respectively. Taking this into account it is possible to assume a similar relationship for laminates i.e,

$$\varepsilon^C = \frac{K}{l^2} \tag{13}$$

where K is a constant of proportionality, dependent upon the material properties and width of the sublaminate. In particular it is noted that K is invariant with regard to a change in length of the delaminated region. Alternatively, the buckling equation for a simply supported rectangular orthotropic plate under axial compression is;

$$N_x\left(\frac{\pi}{l}\right)^2 + 2N_{xy}\frac{\pi^2}{lb} + N_y\left(\frac{\pi}{b}\right)^2 = D_{11}\left(\frac{\pi}{l}\right)^4 + 2(D_{12} + 2D_{66})\left(\frac{\pi}{l}\right)^2\left(\frac{\pi}{b}\right)^2 + D_{22}\left(\frac{\pi}{b}\right)^4 \tag{14}$$

Assuming $l = b$ (i.e. a square plate), dividing through by $\left(\frac{\pi}{l}\right)^2$ and collecting terms in D (bending stiffness') into a single constant P we have,

$$N_x + 2N_{xy} + N_y = \left(\frac{\pi}{l}\right)^2 P \tag{15}$$

Since the left hand side is a linear function of ε^C due to the effective modulus equations (Eq's. (3) and (4)), as before this can further be reduced to

$$\varepsilon^C = \frac{K}{l^2} \tag{16}$$

It is assumed that the load per unit width, applied after buckling has occurred is constant and equal to the critical buckling strain multiplied by the membrane stiffness A_{11}. However, it must be noted that the buckling strain will differ before and after propagation due to the change in length of the buckled region. So let ε^C be the critical buckling strain before propagation and ε_A^C be the critical buckling strain after propagation (see Figs 10. (b) and (c)) then,

$$\varepsilon_A^C = \frac{K}{(l + \delta l)^2} \tag{17}$$

which implies the bending energy before propagation is,

$$U_1(l) = A_{11} l \varepsilon^C (\varepsilon - \varepsilon^C) \tag{18}$$

and the bending energy after propagation is,

$$U_1(l+\delta l) = A_{11}(l+\delta l)\varepsilon_A^C(\varepsilon - \varepsilon^C) \tag{19}$$

Note here that the equations assume displacement control since the applied strain, effectively $(\varepsilon - \varepsilon^C)$, is unchanged after propagation. Hence, the bending energy released by propagation is given by,

$$U_1(l) - U_1(l+\delta l) = A_{11}(\varepsilon - \varepsilon^C)(\varepsilon^C l - \varepsilon_A^C(l+\delta l)) \tag{20}$$

Applying Eqs. (11) and (12) then implies

$$U_1(l) - U_1(l+\delta l) = A_{11}(\varepsilon - \varepsilon^C)\left(\frac{K}{l} - \frac{K}{(l+\delta l)}\right) \tag{21}$$

Since δl is infinitesimal a simple application of the binomial theorem to $(l+\delta l)^{-1}$ in which terms of second or higher order are ignored, gives

$$U_1(l) - U_1(l+\delta l) = A_{11}(\varepsilon - \varepsilon^C)\varepsilon^C \delta l \tag{22}$$

The membrane energy per unit width associated with the sublaminate is calculated using the equation

$$U_2 = \frac{A_{11}}{2}\int_0^l \varepsilon^2 dx \tag{23}$$

However, an allowance is made for a reduction of stiffness following buckling by introducing a stiffness reduction factor, the ratio of post-buckling stiffness to pre-buckling stiffness r. Hence the post-buckled membrane strain energy is given by,

$$U_2 = \int_0^l \frac{A_{11}}{2}[(\varepsilon^C)^2 + r(\varepsilon - \varepsilon^C)^2]dx \tag{24}$$

i.e.

$$U_2 = \frac{A_{11}}{2} l[(\varepsilon^C)^2 + r(\varepsilon - \varepsilon^C)^2] \tag{25}$$

Or alternatively, the equation can be derived from Fig. 14 area a_2 and a_3. For the region of length δl, before propagation occurs, there is no buckling and hence no bending energy associated with it, hence only membrane energy is available which is given by,

$$U_2^* = \frac{A_{11}}{2}\int_0^{\delta l} \varepsilon^2 dx \tag{26}$$

After propagation has occurred the full region buckles and the membrane energy is given by Eq. (18) with l replaced by $l + \delta l$.

Now the energies have been computed it is possible to compare energies before and after propagation in order to calculate the strain energy release rate (SERR) G_1.

$$G_1 = \lim_{\delta l \to 0}\{U_1(l) - U_1(l+\delta l) + U_2(l) - U_2(l+\delta l) + U_2^*\}\frac{1}{\delta l} \tag{27}$$

The application of this equation to the above functions gives,

$$G_1 = \frac{A_{11}}{2}(\varepsilon - \varepsilon^C)[\varepsilon(1-r) + \varepsilon^C(3+r)] \tag{28}$$

Results obtained by Koiter and Pignataro [75] and Weaver and Diaconu [68] suggest that $0.35 < r < 0.65$ for orthotropic laminates.

Here the sublaminates can be asymmetric and anisotropic and a value of $r = 0$ is chosen for mathematical simplicity, although comparison with $r = 0.5$ [75] (isotropic laminates with clamped boundaries under pure axial compression) is also considered. It should also be noted that $r = 0$ produces lower bound values for the threshold strain. Hence, for $r = 0$,

$$G_1 = \frac{A_{11}}{2}(\varepsilon - \varepsilon^C)(\varepsilon + 3\varepsilon^C) \tag{29}$$

It is worth noting, the similarity of equation (23) and those produced by Butler et al 4] and Chai et al [6] and secondly, the presence of the term $(\varepsilon - \varepsilon^C)$ which ensures no energy is released until buckling has occurred and the delamination has opened.

The threshold strain, defined as the strain at which the SERR for the fracture of post-buckled delaminated plies along the delamination is equal to the critical Mode I value (G_{1C}); this is the SERR required to cause Mode I failure of the resin. To obtain the threshold strain $\varepsilon = \varepsilon_{th}$ and the critical level of delamination it is necessary to solve Eq. (23) for ε, hence,

$$\varepsilon = \frac{\varepsilon^C}{(1-r)}\left(-(1+r) + \sqrt{(1+r)^2 + (1-r)\left((3+r) + \frac{2G_1}{(\varepsilon^C)^2 A_{11}}\right)}\right) \tag{30}$$

If then G_I is set equal to G_{IC}, it is possible to calculate the threshold strain, i.e.

$$\varepsilon_{th} = \frac{\varepsilon^C}{(1-r)}\left(-(1+r)+\sqrt{(1+r)^2+(1-r)\left((3+r)+\frac{2G_{IC}}{(\varepsilon^C)^2 A_{11}}\right)}\right) \tag{31}$$

and, for $r = 0$,

$$\varepsilon_{th} = \varepsilon^C\left(-1+\sqrt{4+\frac{2G_{IC}}{(\varepsilon^C)^2 A_{11}}}\right) \tag{32}$$

The interface with lowest ε_{th} will begin to release energy first and hence will be the first to propagate.

Note that unlike Chai et al [6], for enclosed delaminations the propagation model does not include any terms that refer implicitly or explicitly to Poisson's ratio effects. This is due to assumed continuity along the transverse (circumferential) edge of the delamination. Hence it is assumed that strain energy is only released in the longitudinal direction. In reality forces do occur in the transverse direction due to differences in Poisson's ratio between the delaminated region and the full laminate and these forces may be compressive or tensile depending on whether the Poisson's ratio of the delaminated region is larger or smaller than that of the full laminate.

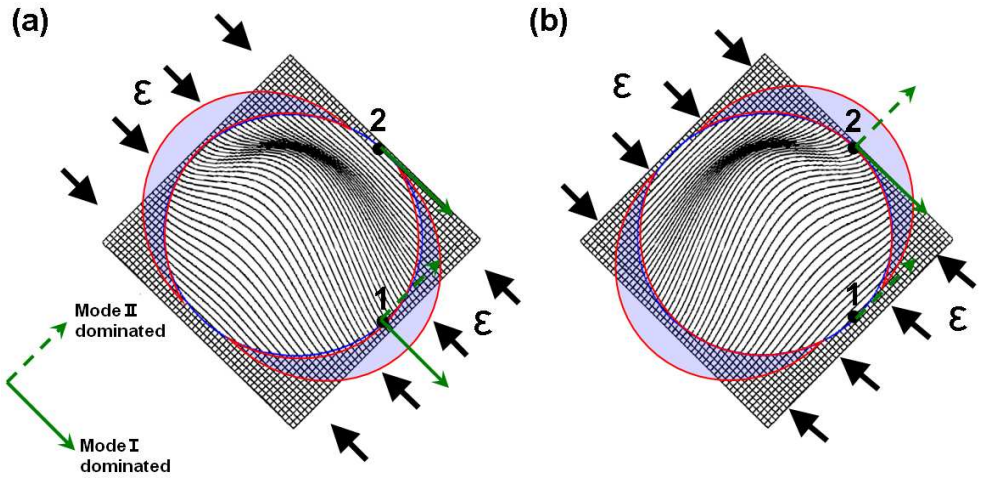

Fig. 15. Images showing directions of growth for circular delaminations with post-buckled sublaminates having fibres; (a) aligned with the load, and (b) perpendicular to the load.

However, propagation of the delamination is assumed to initiate under Mode I dominated conditions. For enclosed circular delaminations with buckled sublaminates having most fibres in the same direction as the load, see Fig. 15(a), this is representative of initiation and is consistent with the 2D model of Chai and Babcock [3]; and hence the above assumption holds. However, for sublaminates with fibres that are mostly in the transverse direction the difference between Poisson's ratio deformation in the laminate and the buckling deformation of the thin sublaminate causes a transverse strain distribution which will put the thin sublaminate into relative tension and hence propagation has a considerable Mode II contribution, see Fig. 15 (b).

Despite this, a purely Mode I (G_I) condition is applied in Eq's. (31) and (32) for all cases and is taken as a lower bound approximation for growth in the load direction at point 2 in Fig. 15(b). Conservativeness of a pure Mode I condition for transverse growth, under the assumption that lateral propagation is dominated by Mode

II effects, can be proven by establishing the following which assumes SERR can be split into Mode I and Mode II contributions,

$$\frac{G_I}{G_{IC}} > \frac{G_{II}}{G_{IIC}} \tag{33}$$

The propagation model assumes release of energy from bending and membrane energy in the load direction whereas physically, in the transverse direction, a better estimate would be that almost all energy released would come from a relaxation of the curvature of the buckle and hence bending energy. Thus a comparison of Eqs. (22) as $\delta l \to 0$ (bending energy released) and (28) (full energy released) with $r = 0$ applied to Eq.(33) again with the bending energy being equated to work done in the axial direction as per Eq. (11) and released as per Eqs. (18-22) gives,

$$\frac{A_{11}}{2G_{IC}}(\varepsilon - \varepsilon^C)(\varepsilon + 3\varepsilon^C) > \frac{A_{11}}{G_{IIC}}(\varepsilon - \varepsilon^C)\varepsilon^C \tag{34}$$

or

$$\frac{\varepsilon + 3\varepsilon^C}{2G_{IC}} > \frac{\varepsilon^C}{G_{IIC}} \tag{35}$$

Since G_{IIC} is always greater than G_{IC}, Eq.(35) is always true. Hence

Eq.(31) always gives a lower bound and therefore fulfilment of a Mode I condition will always be conservative and necessary for growth to initiate, although in reality all propagation is mixed.

In [3] Chai and Babcock calculate a general SERR based on an integral of the full stress state that incorporates energies for all modes and compares them with G_{IC} i.e. propagation is calculated to occur when,

$$\frac{G_I + G_{II} + G_{III}}{G_{IC}} \geq 1 \tag{36}$$

This compares with the real situation which is given by,

$$\frac{G_I}{G_{IC}} + \frac{G_{II}}{G_{IIC}} + \frac{G_{III}}{G_{IIIC}} \geq 1 \tag{37}$$

However, by making the substitution $G_{IC} = \beta G_{IIC} = \gamma G_{IIIC}$ where $\beta, \gamma < 1$ it follows that,

$$\frac{G_I}{G_{IC}} + \frac{\beta G_{II}}{\beta G_{IIC}} + \frac{\gamma G_{III}}{\gamma G_{IIIC}} = \frac{G_I + \beta G_{II} + \gamma G_{III}}{G_{IC}} < \frac{G_I + G_{II} + G_{III}}{G_{IC}} \tag{38}$$

Hence, Chai and Babcock's assumption is shown to be conservative and thus with reference to Fig.16 the current model is also shown to conservative for the three cases of sublaminate; fibres in the load direction, fibres perpendicular to the load and an isotropic case.

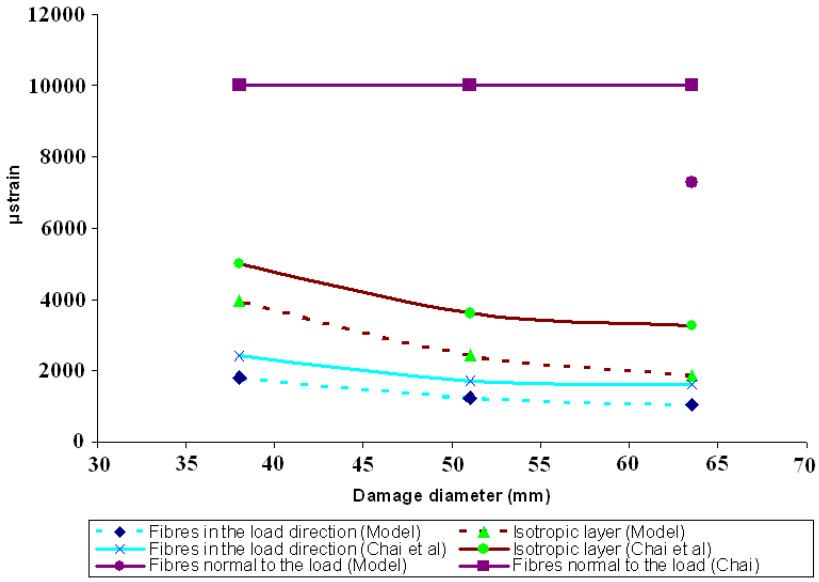

Fig. 16. Comparison of results from [3] and the propagation model. Note that results for 'Fibres normal to the load' are given in [3] as >10,000 μstrain hence this line is a lower bound for these results.

A Mode I condition is also considered more appropriate in the free edge impact problem as forces due to incompatibility in Poisson's ratio strains that occur between the base and sublaminate in an enclosed buckle (which is considered to drive Mode II delamination) do not occur in the free edge impact problem. This is due to the sublaminate buckle being able to deform, relieving Mode II stresses, rather than inducing transverse tension as it would be forced into an enclosed buckle subject to compression.

6.1. Optimisation

The propagation model is a combination of the four variables ε^C, ε, A_{11} and G_I. As such it describes a 4D surface. Although it is difficult to extract useful information directly from this 4D surface, it is possible to fix one or more of the variables at an appropriate value (usually at $\varepsilon = \varepsilon^{th}$ or $G_I = G_{IC}$) to create 2D or 3D surfaces which are much easier to interpret. Such surfaces allow determination of the sensitivity of the laminate to damage geometry [73] and stability of

delamination growth [73] as well as suggesting optimal laminate stacking sequences for damage tolerance. Figure 17 shows a 3D

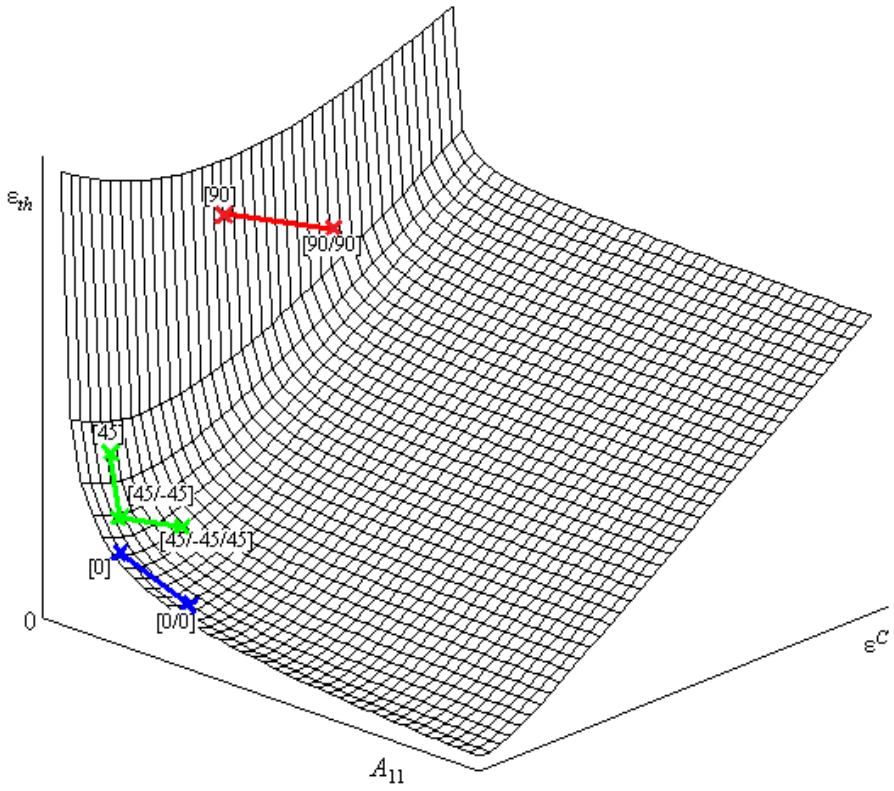

Fig. 17. 3D surface created by fixing $G_I = G_{IC}$ with seven theoretical representative sub-laminates.

surface created by fixing $G_I = G_{IC}$. This surface allows all possible sub-laminates, which are defined by A_{11} and ε^C with regard to the model, to be compared and hence some optimal features to be identified.

With the objective of optimising threshold strain, and hence maximising compressive strength after impact (CAI), it is quite clear from Fig. 17 that this is accomplished principally by minimising A_{11} and secondly by maximizing ε^C. Figure 17 shows the position on the surface of 7 general theoretical sub-laminates of a quasi-isotropic

laminate. The sub-laminates highlighted on Fig. 17 consisting of 1 layer have equal damage area and as such their associated threshold strains are directly comparable. This is also true for the sub-laminates in Fig. 17 with 2 layers. Noting this, the sub-laminates made from 90° and 45° layers are obviously more optimal than those made from 0° layers as the former offer minimal A_{11} and maximal ε^C. However, as the number of layers in the sub-laminate inevitably grows, layers other than 90° or 45° will have to be introduced into the sub-laminate which may cause the focus of optimisation to move from minimising A_{11} to maximising ε^C. This change in focus will be determined by the condition,

$$\left|\frac{\partial \varepsilon_{th}}{\partial A_{11}}\right| < \left|\frac{\partial \varepsilon_{th}}{\partial \varepsilon^C}\right| \tag{39}$$

6.2. Sensitivity to growth and material properties

Figure 18 shows a 3D surface described by the variation of ε^C, ε and G_1 in Eq. (29). This surface can be used to indicate the sensitivity of laminates to errors present in the values used for A_{11}, G_{1C} and ε^C, and also shows the stability of growth that occurs once propagation of the delamination has been initiated, i.e., $\varepsilon > \varepsilon_{th}$. Each laminate has a slightly different surface that depends on the particular properties of the laminate. However, the surfaces all have the same general shape which is based around a saddle point. The surfaces themselves are quite difficult to extract information from, but it is possible to take cross-sections of the surface by fixing one of the three variables such as the one shown as a plane in Fig. 18.

The first cross-section to be considered is one that fixes a value of the applied strain, Fig. 19. This value is fixed at the threshold strain for the sublaminates being considered. The graphs relate the buckling strain to the energy available for propagation. Note here that the buckling strain is the variable affected by changes in the shape of the delamination, in particular note that as propagation occurs the delamination will start to take on an elliptical shape which results in a change in buckling strain.

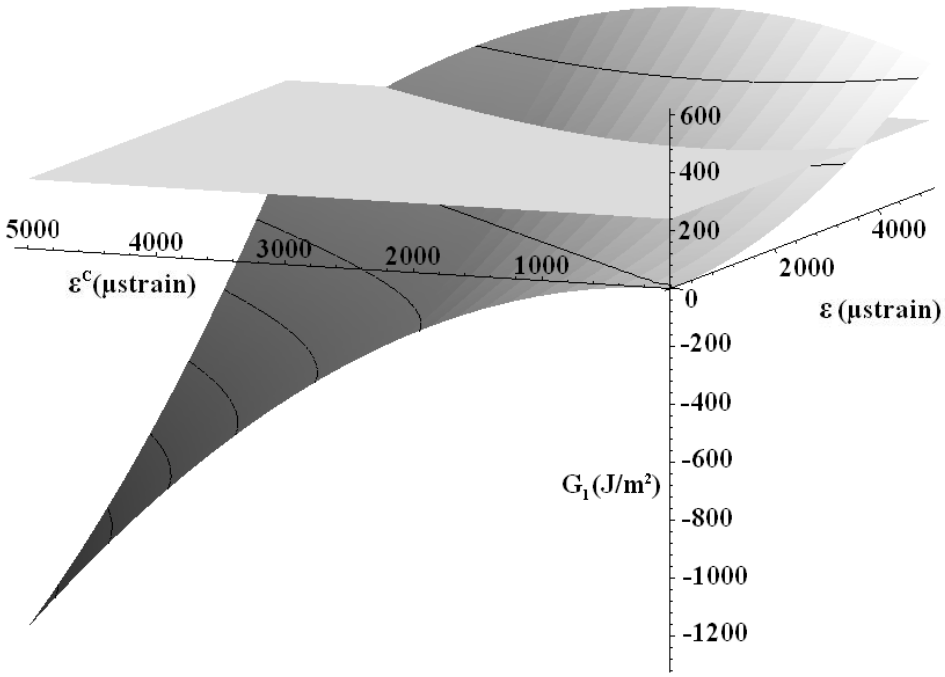

Fig. 18. Generic 3D surface produced by allowing variation of ε^C, ε and G_1 in Eq. (29). Note also the intersection of the plane that is fixed at $G_1 = G_{1C}$ and the surface. The curve along the interface is similar to Figs. 21 and 22.

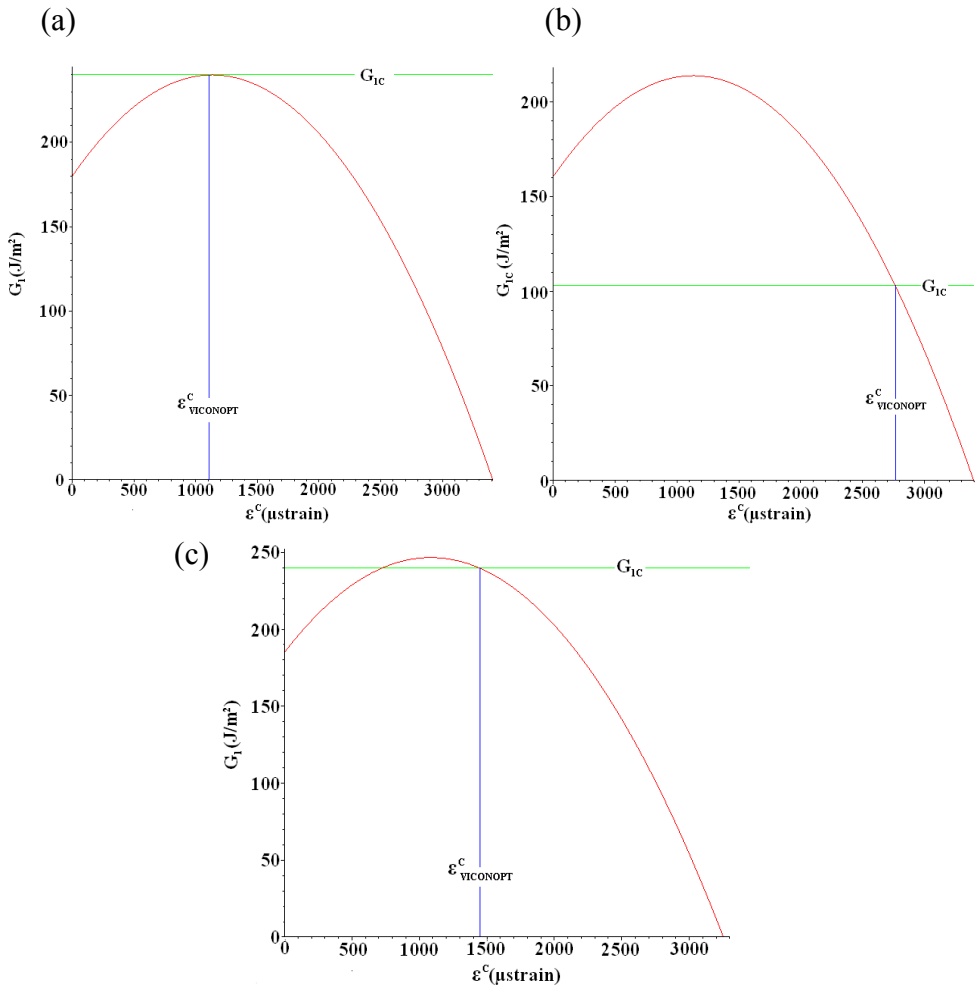

Fig. 19. (a) A cross-section of the surface along the plane of $\varepsilon = \varepsilon_{th}$ for showing stable growth. (b) A cross-section of the surface along the plane of $\varepsilon = \varepsilon_{th}$ showing unstable growth.

From Fig. 19(a) it can be seen that as the buckling strain drops from that of the circular delamination (indicated by the vertical line) the energy drops and so growth of the delamination is stable i.e. the applied strain must be increased for more propagation to occur. In contrast Fig. 19(b) shows that as the buckling strain decreases due to propagation the energy in the laminate increases. This shows that unstable growth occurs for this laminate as the energy level remains above the G_{1C} value. Fig. 19(c) shows unstable growth followed by stable growth as the buckling strain decreases far enough. A condition for stability can be derived by calculating the buckling strain

associated with the maximum of the curves in Fig. 19. The maximum is given by,

$$\frac{dG_1}{d\varepsilon^C} = 0 \tag{40}$$

Solution of Eq. (40) gives an inequality for determination of stability,

$$\varepsilon^C \leq \frac{\varepsilon_{th}}{3} \tag{41}$$

i.e. if the inequality Eq.(41) holds growth is stable. Note that for all cases in Fig. 19 it is possible that damage propagation may halt at the interface being considered if growth at a different interface will produce a lower energy system. Note also Chai and Babcock [3] show similar behaviour is possible for isotropic and orthotropic sublaminates dependent on geometric properties of the initial damage and the depth of the critical delamination at which propagation initiates.

Figure 20 defines the elastic buckling coefficient k_0 for a simply supported square plate i.e. a=b in Fig. 20. If it is assumed that a circular delamination will show a relationship similar to that in Fig. 20. Then considering 'typical' buckling strains for 0^o and 90^o dominated square laminated plates as plotted on Fig. 20 it can be seen that for a 0^o dominated sublaminate transverse growth (i.e. an increase in b) is stable as buckling strain increases and growth in the loading

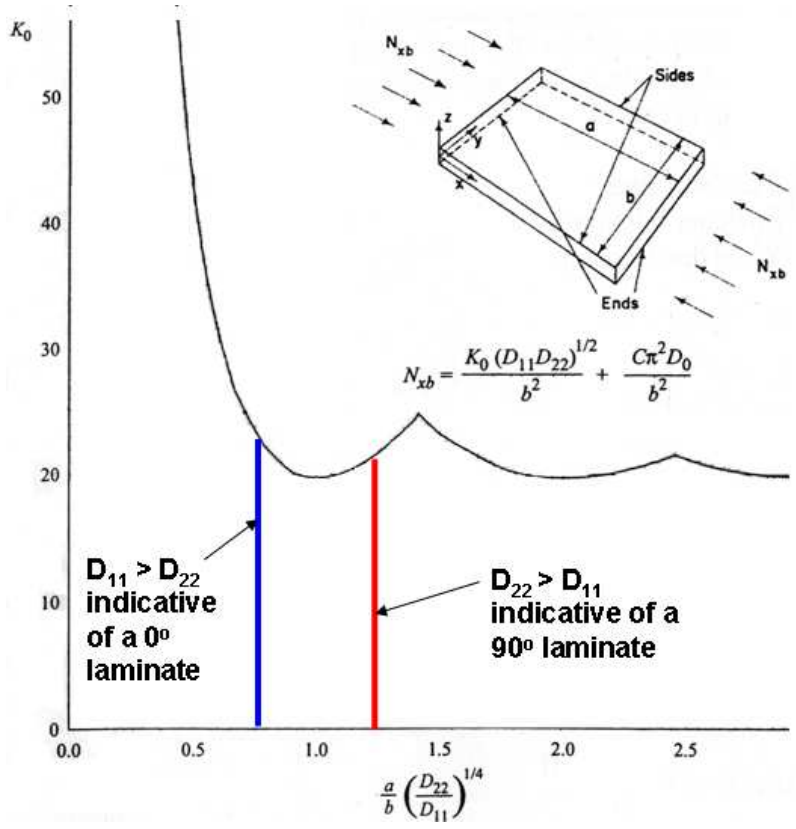

Fig. 20. from ESDU [76] Critical buckling load for a simply supported square plate with dimensions a and b. Vertical lines represent 'typical' values on the horizontal axis for a square laminated plate which is either 0^o or 90^o dominated.

direction (i.e. an increase in a) is unstable as the buckling strain decreases.

The converse is true for 90^o dominated square sublaminates with unstable growth likely to occur in the direction transverse to the load. This would suggest that growth is likely to occur in the dominant fibre direction. If Fig. 20 is considered with a=b and $D_{11} = D_{22}$, i.e. an isotropic laminate, then delamination growth is likely to be stable as the strain required for buckling will increase with growth in either direction. However, it is noted that the effect of post-buckling changes in buckling mode shape and subsequent growth at other interfaces will have an affect on stability of growth not captured here

as will the thicknesses of the base and sublaminates though the sublaminate thickness is taken into account and the thin-film assumption means the base is assumed to be infinitely thick. Assuming again a=b, unstable growth followed by stable growth is likely to occur for a sublaminate which is close to being isotropic as a small growth in a or b (depending on the dominant stiffness direction in the sublaminate) would place the sublaminate at the minimum of the curve in Fig. 20.

Figures 21 and 22 show cross sections of Fig. 18 for fixed A_{11} and G_{1C}. Clearly for Fig. 21 the variation of ε^C has little effect. For Fig. 22 the variation in threshold strain for a small change in ε^C is a little more pronounced but still relatively small. Note here that the variations being considered in ε^C are not due to changes in material properties as this would result in a different curve in Figs. 21 and 22. Comparing Figs. 21 and 22 using gradient considerations it can be seen that the sensitivity of a laminate to buckling strain can be determined by the proximity of the VICONOPT critical strain to the minimum of Eq. (32) given by,

$$\frac{\partial \varepsilon_{th}}{\partial \varepsilon^C} = 0 \tag{42}$$

Which for $r = 0$ implies;

$$\varepsilon^C = \sqrt{\frac{G_{1C}}{6A_{11}}} \tag{43}$$

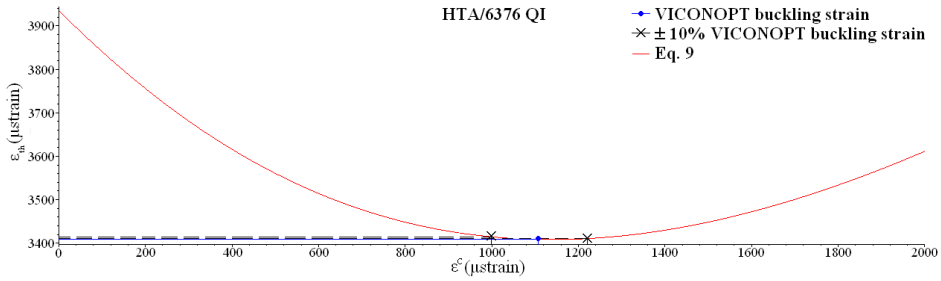

Fig. 21. Effect of varying buckling strain on threshold strain for a parametrically insensitive laminate.

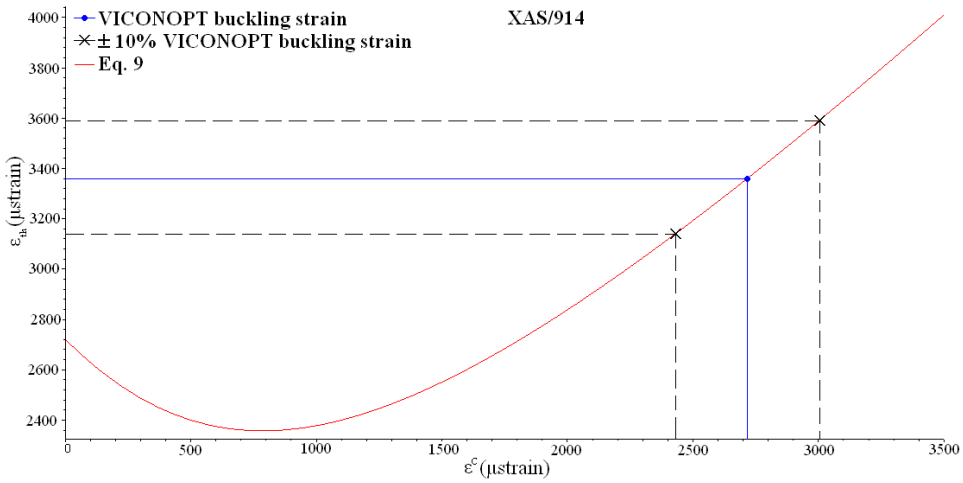

Fig. 22. Effect of varying buckling strain on threshold strain for a parametrically sensitive laminate.

This sensitivity can be quantified by creating a sensitivity ratio, R_S ,

$$\frac{f(\varepsilon^C(1+\alpha)) - f(\varepsilon^C(1-\alpha))}{2\alpha\varepsilon^C} = R_S \tag{44}$$

where f defines the right hand side of Eq. (32) and α defines the variation of buckling strain, (i.e. $\alpha = 0.1$ would represent a 10% variation of buckling strain). The denominator is the spread of the

buckling strains and the numerator is the projection of these strains onto the threshold strain axis. A sensitivity ratio close to zero indicates a high tolerance to variation of buckling strain. R_S can be used as a comparative tool for laminates and will indicate the laminate with the lowest sensitivity to buckling strain which may in turn show which laminate is least sensitive to damage size.

Equation (42) shows it is possible to attain a low value of R_S by choosing laminates with a certain ratio of G_{1C} to A_{11}. In particular a high ratio, which pushes the minimum to the right, is achieved by a large G_{1C} and a low A_{11}, although care must be taken in altering A_{11} as this will affect ε^C.

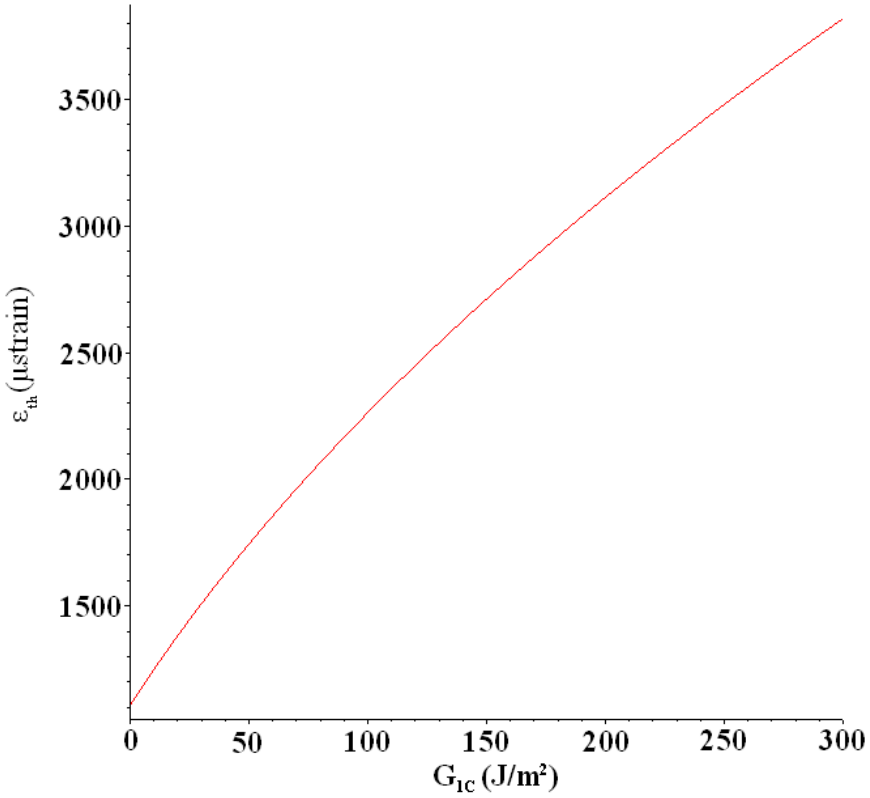

Fig. 23. A cross-section of the surface along the plane of $\varepsilon^C = 1108$ μstrain for the 5th level sublaminate of the HTA/6376 QI laminate.

The final possible cross-section is to fix the buckling strain at the critical buckling strain and from Fig. 23 it can be seen that the resulting relationship between ε_{th} and G_{1C} is an approximately linear one. Similar trends were also identified for the other laminates.

The cross-section shows the sensitivity of the threshold strain to errors in the calculation/determination of G_{1C} for the particular laminate in question and the effect of altering G_{1C} (i.e. changing the resin system) on the residual strength of a general laminate. Note that increasing G_{1C} to a value consistent with those displayed by thermoplastic resin systems enhances the damage tolerant benefits of 45^{o} and 90^{o} layers over 0^{o} layers.

6.2.1. Sensitivity to material parameters

As explained in Chapter 5 the critical (buckling) strains in Table 1 were calculated in VICONOPT using 12 constrained nodes and six strips (Fig. 13). However, it is possible to model the boundary of the delamination in a number of different ways, described below.

The first consideration is to alter the constraints placed on the boundary of the delamination by the nodes. In the results reported in Table 1 full constraint was applied at each node which is the equivalent of a fully clamped boundary i.e. no displacement or rotation is allowed in any plane. However, in the methods reported in Chapters 7.1 and 7.2 buckling guides were used around the delaminations. These guides constrain rotation and out of plane movement; not in-plane compression/Poisson effects, although these may be partially constrained by the undelaminated region. Hence it was necessary to understand the effect of altering the nodal boundary conditions in VICONOPT.

Secondly, it is possible to increase the number of nodes and therefore strips that describe the circular delamination and its boundary. In VICONOPT, nodes are used to describe the edge of the delamination, which means the problem is discretely constrained at intervals around this boundary. Increasing the number of nodes has the effect of bringing the boundary closer to the test situation of a continuously constrained delamination boundary.

A further consideration is the spacing of the nodes around the circular delamination. The results presented in Chapter 7/Table 1 use a fixed strip width which leads to an uneven distribution of nodes around the circumference of the delamination and hence some regions are more tightly constrained than others. An alternative approach is to fix the arc length between nodes and to alter the strip width, thus producing equally spaced constraints around the delamination boundary.

The final aspect tested was the diameter of the delamination, this was considered necessary as the diameter is obtained from NDT and is only approximate.

All the above considerations (number of nodes, boundary constraints, etc…) were thoroughly tested and an example of the effects on the buckling and threshold strains can be seen in Table 1. For the case of the AS4/8552 laminate in Table 1 note that, although the buckling strain changed considerably with these alterations, the threshold strain varied very little. The reasons for this are investigated in Chapter 6.

Summary

In order to fulfill objective 3 in Chapter 2 an analytical model was created that uses basic and freely available material properties, a damage representation simplified from NDT images and a critical buckling strain calculated in VICONOPT.

The model calculates a conservative level of strain for plate like composite structures with BVID under static and fatigue compressive loading regimes in comparison to a fully 2D model from Chai [3]. In addition the propagation model is fully analytic and a single line equation hence has excellent computational efficiency.

Equations are derived that analyse the sensitivity (robustness) of the model to problem parameters including material properties and damage shape, area and depth partially fulfilling objective 4 from Chapter 2. The direction and stability of growth are analysed and pure Mode I growth is shown to be a conservative approximation to mixed mode growth. Optimal sublaminate properties for improved damage tolerance are derived.

Table 1

Effects of alterations to VICONOPT problem data on buckling and threshold strain for an AS4/8552 coupon from [73].

Alteration	ε^C(μstrain)	ε_{th}(μstrain)
None	1193	3035
Constraints on nodes equivalent to an anti-buckling guide	1141	3029
10 Nodes	1269	3047
Equal arc length	1173	3033
Delamination diameter increase of 5%	1082	3025

7. Experimental validation

This Chapter details experimental work used to validate the model together with the results of the validation. Problems modelled in this chapter are limited to those placed in axial compression and can be categorised essentially by loading regime, delamination boundary (either fully contained or free edge) and the aerospace component in which the damage occurred. Specifically; enclosed delaminations in plates under both fatigue and static loading, static compression of stiffened panels with impacts on the skin under the stiffener foot resulting in enclosed BVID and T-stiffeners section where impact occurs parallel to the plane of the laminate on the free edge. Further to this problems are described by the boundary constraints placed on the delaminated sublaminate and the loading transferred to the delaminated region through its attachment to the undelaminated full laminate. A summary of problems and their key components is given in Fig. 24.

Optimised laminates for both enclosed and free edge impact problems whose stacking sequences were suggested by the properties derived in Chapter 6.1 are given here with corresponding analytical predictions. Experimental results are also given for three optimised laminates with enclosed delaminations that were tested in static compression.

Table 2 gives material properties for the materials used in the model validation. Note that these materials cover a range of values typical of those used in aerospace composites and that the laminates studied in this chapter vary in thickness, impact energy, stacking sequence and BVID area. This wide range of laminate parameters provides an excellent source of validation for the propagation model.

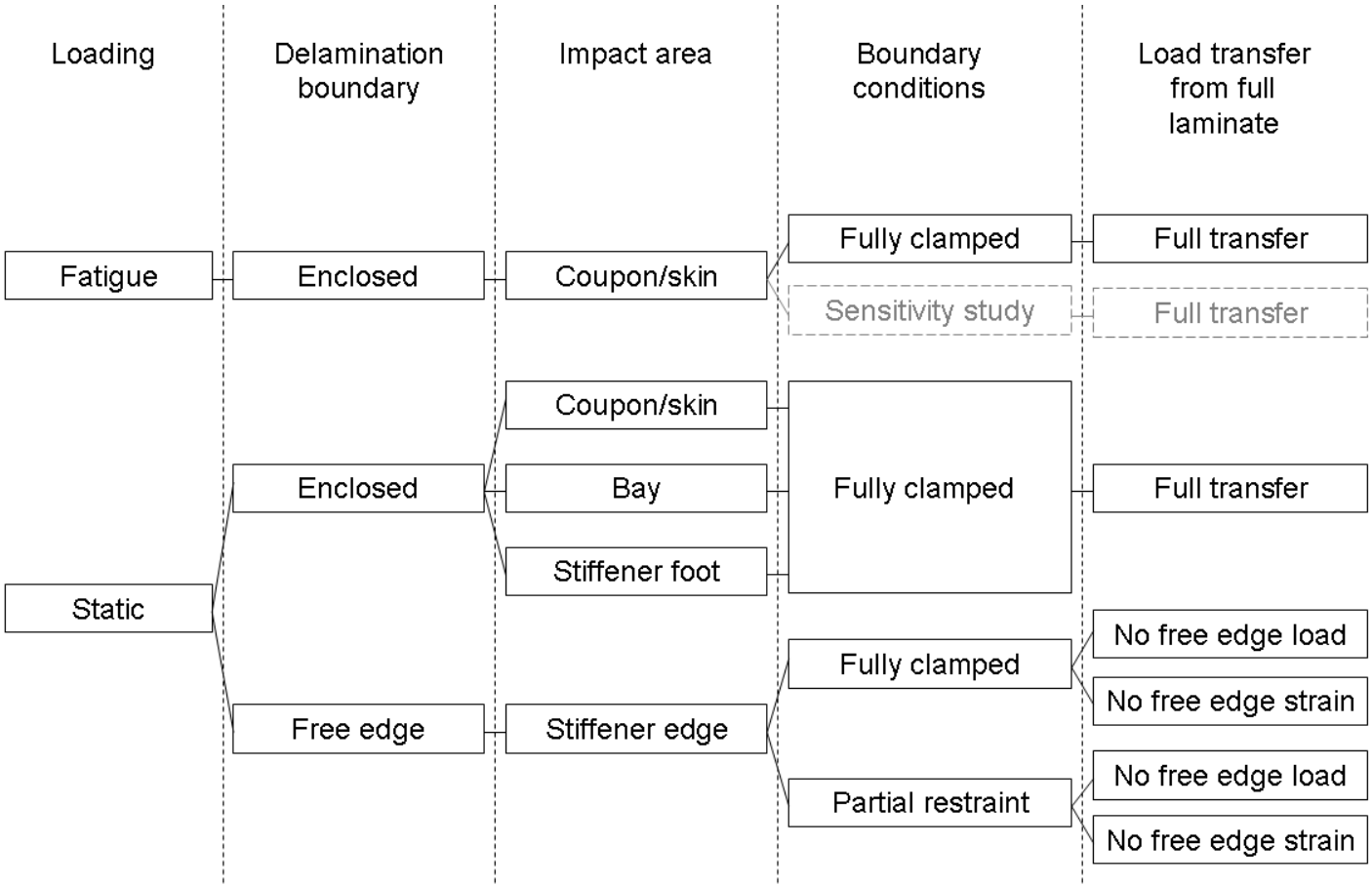

Fig. 24. Overview of experimental/analytical problems detailing problem breakdown

Table 2

Material properties of the laminates taken from [5] (AS4/8552, XAS/914), [11] (HTA/6376), [77] (UT500/Epoxy) and [78] (UTS/977-2) respectively, t is layer thickness.

Material	E_{11} (GPa)	E_{22} (GPa)	G_{12} (GPa)	v_{12}	t (mm)	G_{IC} (J/m^2)
AS4/8552	128.0	10.3	6.0	0.3	0.25	261
XAS/914	135.0	8.5	6.0	0.3	0.125	103
HTA/6376	133.0	10.8	3.6	0.29	0.13	240
UT500/Epoxy	124.0	9.6	5.75	0.344	0.167	280
UTS/977-2	117.0	17.0	4.6	0.3	0.25	478

7.1. Fatigue problems

For fatigue problems the propagation model is applied as a quasi-static approximation to the conditions apparent in the final rapid stages of fatigue damage growth (following earlier non-critical steady growth) and is intended to find the level of strain required to initiate this growth. In particular, delaminations at a significant depth within the sample are assumed to have buckled and subsequently opened hence making a Mode I propagation assumption valid. Note that once a coupon has been fatigued at a level of strain that allows it reach this final rapid stage of fatigue propagation it will fail hence for fatigue tests failure and threshold strains calculated by the model are comparable.

7.1.1. Experimental details

The propagation model with fatigue loading conditions was tested for validation purposes on a range of laminates with varying materials and lay-ups taken from the literature by Curtis et al [10], Melin and Schön [8], Melin et al [11] and Chen et al [12]. These papers used differing test data and a brief summary of each is given below. The material properties are given in Table 2.

AS4/8552 coupons (Chen et al, [12])

BVID was introduced centrally into coupons of 4mm thick AS4/8552 material with lay-up $[(45,0,-45,90)]_{2S}$ using 6kN of static load (equivalent to 10J of impact energy) applied to one side of the specimens while they were clamped over a rectangular window. The central delaminations created were approximately 27mm in diameter as indicated by acoustography images from Chen et al [12]. Samples prepared with BVID were placed in axial compression fatigue (R=10) and prevented from buckling by an anti-buckling guide which left an exposed central circular region 85mm in diameter. Note that a fatigue

limit of 3600 μstrain was incorrectly reported for these coupons in [5] since that study did not obtain upper and lower bounds on the threshold strain, and hence was conservative. A more extensive set of results, which did bound the threshold strain, was given in [12].

XAS/914 coupons (Curtis et al [10])

BVID was introduced into coupons of 2mm thick XAS/914 material with lay-up $[(45,-45,0,90)]_{2S}$ using an incident energy level of 7J. Impacts were repeated at 55mm spacing across large panels clamped in circular steel frames 100mm in diameter. The impacted panels were cut into 250mm long and 50mm wide coupons and tested with an anti-buckling guide in place to prevent overall buckling. Images from [10] suggest the critical BVID damage for these samples fits within a 15mm diameter circle.

HTA/6376 coupons (Melin and Schön and Melin [8,11])

BVID was introduced into coupons of 6.24mm thick HTA/6376 material with a so-called zero dominated (ZD) lay-up $[45,-45,0,90,45,-45,0_2,(45,-45,0,90)_2,45,-45,0_2,45,-45,0,90]_S$ and a quasi-isotropic (QI) lay-up $[(90,-45,45,0)_S,(0,45,-45,90)_S]_3$ using an impact energy of 27J. Note because of the asymmetry of the HTA/6376 QI laminate it is necessary to establish impact and back faces in order to give the correct lay-up for the sublaminate involved in propagation. The impact face is assumed to be the top of the laminate, defined by stacking sequence, which implies the delaminated sublaminate is composed of the bottom layers of the laminate. This assumption was confirmed by comparing model results to reported values using both faces of the laminate as the impact face in the analytical model. Figure 1 shows C-scan images from [8] depicting the BVID damage, which was assumed to approximate a circular area of diameter 50mm. Coupons were 156mm wide and 450mm long, with gripping zones 156mm wide and 100mm long at either end of the specimen.

An anti-buckling window was applied leaving a 100mm x 100mm square able to buckle under compressive loading.

7.1.2. Analytical Results

The experimental and analytical results for threshold strain are presented for comparison in Table 3. The experimental results are a summary of those reported in [8], [10] and [12], with experimental data set out in the previous section. Table 3 also specifies the buckling strain ε^C, determined by VICONOPT according to the procedure set out in Chapter 5, for the sublaminate corresponding to the level at which propagation first occurs. The propagation model predicts that the BVID propagates beyond the circular perimeter of initial damage first at a depth of 2 plies in the AS4/8552 laminate and at a depth of 3 plies in the XAS/914 laminate.

Melin and Schön [8] suggest that propagation occurs at a depth of around 10-20% of total thickness for their plates. Figure 25 shows that damage first grows at a depth of 5 out of 48 plies in the HTA/6376 ZD laminate. The analytical model predicts the same critical depth for the HTA/6376 QI laminate. Note that Fig. 25 may indicate some similarity in threshold strains for the sublaminates with 4,5 and 6 plies, this is due to equally sized delaminations being assumed at each level and the general homogeneity of the sublaminates involved together with the sensitivity of the threshold strain to the buckling strain in this particular problem.

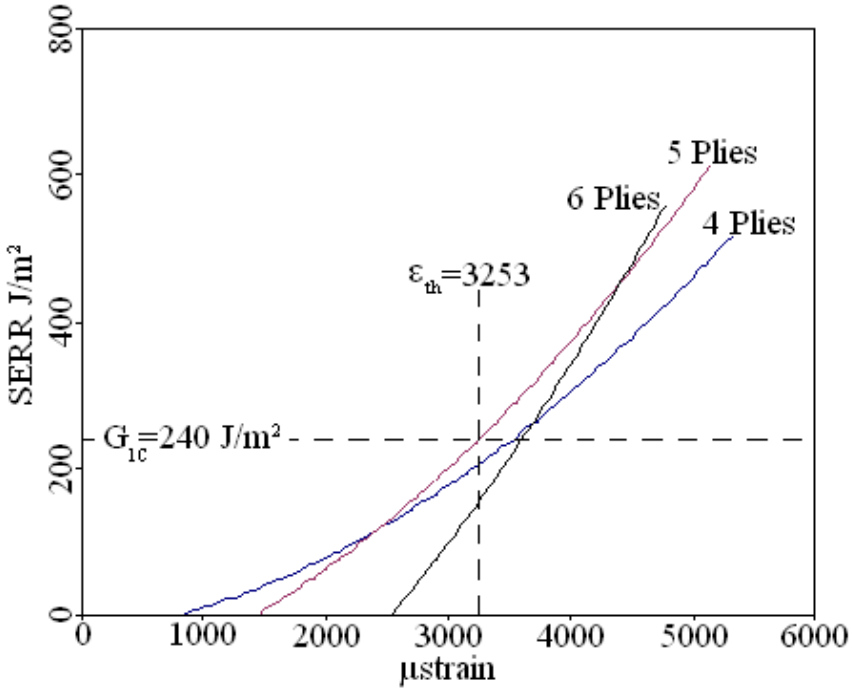

Fig. 25. Strain energy release rate (SERR) for propagation at 4, 5 and 6 ply depths in HTA/6376 ZD laminate.

Table 3

VICONOPT buckling strains and experimental and analytical threshold strains for thin sublaminates at which the delamination first propagates for various laminates described in this chapter. Note that the sublaminate stacking sequences retain the orientation of the full laminate, i.e. the top layer of the sublaminate is the one closest to the impact face.

Material	Sublaminate Lay-up	Buckling Strain (μstrain)	Experimental	Analytical Threshold strain (μstrain)	
				r=0	r=0.5
AS4/8552	[0,45]	1193	3100	3035	3320
XAS/914	[0,-45,45]	2763	3400	3397	3414
HTA/6376 QI	[90,90,-45,45,0]	1108	3300	3408	3557*
HTA/6376 ZD	[45,90,0,-45,45]	1440	3300	3253	3467

* Critical level changes from [90,90,-45,45,0] to [-45,90,90,-45,45,0]

7.1.3. Discussion

Although the model is tested on relatively few laminates it should be noted that their properties are extremely varied in terms of input energy, material, lay-up and thickness. This suggests that unlike the Butler et al model [5], which was limited to thinner laminates with less complex lay-ups, the propagation model is able to predict threshold strain values for a wide range of problems.

Figure 26 highlights the precision of the propagation model, compared with the experimental results and beam model results of Butler et al in [5]. The difference between the analytical strain predicted by the propagation model with ($r = 0$) and the experimental result is at most 4%. Unfortunately, the ability of the model to predict at which level crack propagation first occurs remains almost entirely untested. Only Butler et al [5] reported at which level the delamination grew. However in this case the model prediction of 2nd ply crack growth matches their observation that growth was at the 2nd and 3rd lamina level. It is worth noting that, as expected, when an axial post-buckled stiffness of $r = 0.5$ is used in Eq. (31), the threshold strain values all increase, Results supporting this are presented in Table 3. The greatest increase occurred for the HTA/6376 QI laminate, where an 8% difference in experimental and analytical results was calculated. Propagation, in this case, was predicted at the sixth ply level.

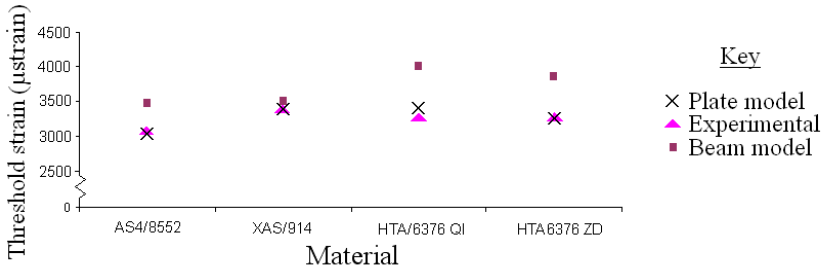

Fig. 26. Comparison of threshold strains.

Fatigue resistant laminate

As a design application for the propagation model a fatigue resistant, manually optimised laminate is now considered. The principle for the optimization was based on two factors; increasing the delaminated plate buckling strain and reducing the SERR. The former was achieved by putting all the ±45^o layers to the outer faces of the laminate, thus increasing buckling resistance. The latter was achieved by moving all the 0^o fibres to the central region as these fibres tend to cause strain energy to release earlier in effect increasing the gradient of the curves of Figs. 25 and 27. With these considerations in mind a manually optimised stacking sequence of $[(45,-45)_6, 0_2, (90,0_2)_2, (90,0)_2]_s$ was chosen. The optimised laminate was assumed to have been made from the HTA/6376 material and had the same area of damage and the same number of 0^o, ±45^o and 90^o layers as the HTA/6376 ZD laminate described above.

The results obtained from VICONOPT indicate a buckling strain of 1941 μstrain and the analytical results predict a threshold strain of 3800 μstrain. Hence the propagation model predicts a threshold strain value for this laminate which is approximately 17% higher than the threshold obtained for the HTA/6376 ZD laminate above. The model also predicted propagation occurring between the 5th and 6th layers which gives a delaminated region with stacking sequence [45,-45,45,-45,45]. Note however, that the threshold strain value and delamination depth have not been experimentally confirmed.

It is interesting to note that in Fig. 25 and Fig. 27 the compressive strength of the laminate initially decreases with sublaminate depth until it reaches a minimum as the delamination is modeled at the 5th interface before beginning to increase again. A similar result was reported by Naik et al [54] for their model. This implies there may be

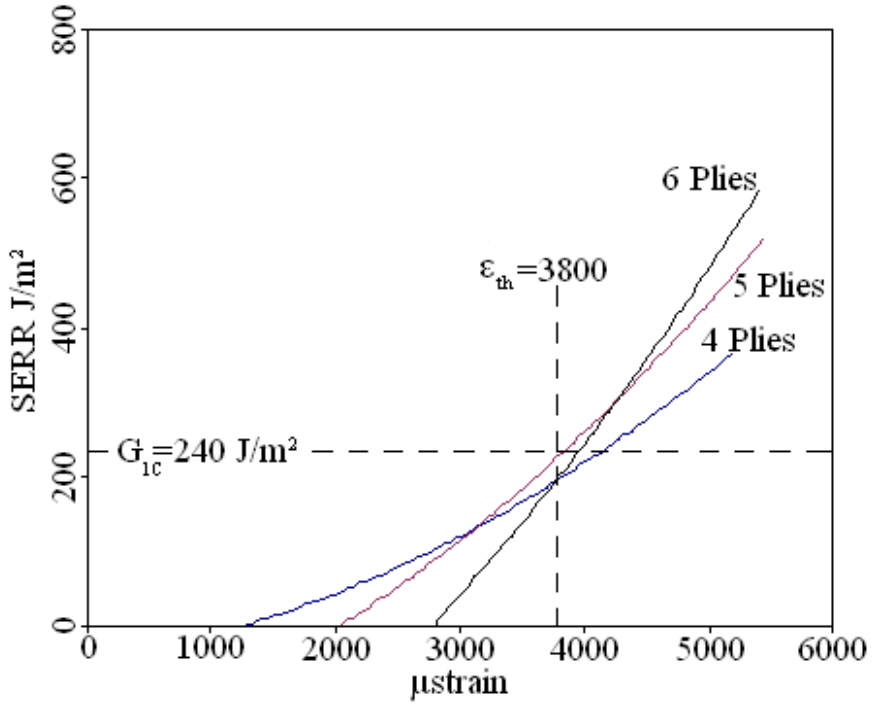

Fig. 27. Strain energy release rate for propagation at 4, 5 and 6 ply depths in optimised HTA/6376 laminate.

a 'critical' through thickness position where delamination should be minimised.

7.1.4. Conclusions

The propagation model is applied as an approximation to the conditions apparent in the final rapid stages of fatigue damage growth and it is assumed that the growth of BVID can be simplified to propagation at a single level within the laminate. It is noted the model is dependent on only three parameters of the problem G_{1C}, ε^C and A_{11}. In a fatigue loading regime assuming no post-buckled stiffness ($r = 0$), the model predicts threshold strain with at most a 4% error compared to experimental values for the laminates tested and is within 1% for some cases. Applying the model to a laminate with

damage tolerant 45^{o}/-45^{o} layers protecting the 0^{o}/90^{o} (such as the laminate above) shows that these types of lay-up offer enhanced damage tolerance under fatigue loading. However, it should be noted that the laminate was manually optimised to maximise buckling strain and minimise SERR. It was not optimised using any specific design strategy nor did it consider other constraints, such as buckling or aeroelasticity. Nevertheless, the model could provide an excellent tool for designing laminates in the future and could reduce the need for expensive and time consuming fatigue testing.

7.2. Static enclosed delamination problems

7.2.1. Experimental details

This chapter outlines experimental problems, including new work (results referenced as [79] in Table 4) and existing problems taken from the literature ([8, 11, 13] in Table 4), that were used to validate the model under static loading. Brief descriptions of the experimental set-up for problems used in validation are included here in addition to applicable material and laminate properties and dimensions in Table 2. Stacking sequences are given in Table 4. The details of impact damage introduced into the coupons/stiffened panel are given in Table 5. All coupons and the stiffened panel from [14] were impacted to produce BVID and subsequently placed in axial compression to determine their static strength.

Details of the experimental set-up of the HTA/6376 (ZD) and (QI) coupons from [8,11] are given in Chapter 7.1. As noted in Chapter 7.1 because of the asymmetry of the HTA/6376 QI laminate it was necessary to establish impact and back faces in order to give the correct lay-up for the sublaminate involved in propagation. The UT500/Epoxy (QI) (Toho Tenax, QU135-197A) coupons from [13] were reduced from 50mm impacted width to 35mm width for compression testing, to allow for the capacity of the test machine.

To prevent buckling of the UT500/Epoxy (QI) coupons, a gauge length of 35mm was chosen and the coupons were supported by guides along their longitudinal edges. The configurations of the stiffened panels stiffened with T-stiffeners from [14] and the locations of the impacts are given in Fig. 28.

Table 4

Example laminates showing relevant references in the literature.

Material	(Laminate ID)	Lay-up	Reference
UT500/Epoxy	(QI)	$[45,0,-45,90]_{3S}$	[13]
HTA/6376	(QI5, QI14)	$[(90,-45,45,0)_S,(0,45,-45,90)_S]_3$	[8,11]
HTA/6376	(ZD)	$[45,-45,0,90,45,-45,0_2,(45,-45,0,90)_2,45,-45,0_2,45,-45,0,90]_S$	[8,11]
HTA/6376	(FOOT)	$[45,-45,0,90]_{3S}$ + $[45,-45,0_3,90,0_3,-45,45]$	[14]
HTA/6376	(BAY)	$[45,-45,0,90]_{3S}$	[14]
AS4/8552	(Control)	$[45,0,-45,90]_{4S}$	[79]
AS4/8552	(45^o Outer)	$[(45,-45)_4,(90,0)_4]_S$	[79]
AS4/8552	(90^o Outer (1) and (2))	$[90_3,45,90,-45_3,0,45_3,0_2,-45,0]_S$	[79]

QI=Quasi-isotropic, ZD=Zero-dominated, FOOT=stiffened panel impact site.

Table 5

Damage details for laminates of Table 4. *T* is total laminate thickness and $l_{\max}$ is maximum damage diameter.

Material (Laminate ID)	*T* (mm)	Impact energy (J)	Tup diameter *d* (mm)	$l_{\max}$ (mm)
UT500/Epoxy (QI)	4	7.6	12	27
HTA/6376 (QI5)	6.24	27	7.5	52
HTA/6376 (QI14)	6.24	27	7.5	47
HTA/6376 (ZD)	6.24	27	7.5	49
HTA/6376 (FOOT)	4.375	15	12.7	30
HTA/6376 (BAY)	3	15	12.7	35
AS4/8552 (Control)	4	8	16	27
AS4/8552 (45^{o} Outer)	4	8	16	37

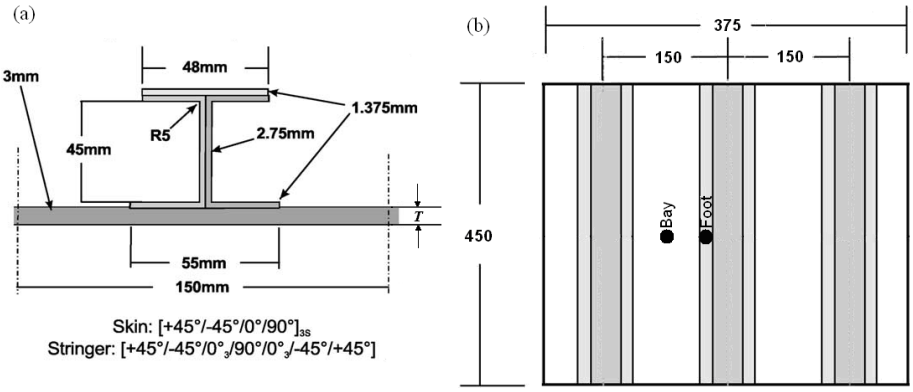

Fig. 28. Stiffened panel example from [14]. (a) Stiffener configuration. (b) Plan view of panel showing impact sites.

Two stacking sequences have been identified as possible candidates for a damage tolerant quasi-isotropic laminate. The first, $[90_3,45,90,-45_3,0,45_3,0_2,-45,0]_S$, was a product of an optimisation routine described in [80] which sought to minimise both angles between plies (to improve damage resistance) and A_{11} while following current design constraints regarding blocking of a maximum of three plies to prevent intraply cracking. The second $[(45,-45)_4,(90,0)_4]_S$ was a product of the author's experience which mimics current design philosophies for prevention of global buckling (placing 45^o layers to the outside of the laminate) whilst also exploring the damage tolerance properties of this configuration. These laminates together with a control laminate $[45/0/-45/90]_{4s}$ have been manufactured and tested the details of which together with the test results are given below.

Quasi-isotropic coupons were made from Hexcel AS4/8552 pre-preg layers with material properties given in Table 1 and stacking sequences given in Table 4. Samples were cured in an LBBC Quicklock Thermoclave using the Hexcel specified curing cycle. Coupons were tabbed with 1.5mm aluminium plates to provide grip and to prevent crushing at the loading points see Fig. 29.

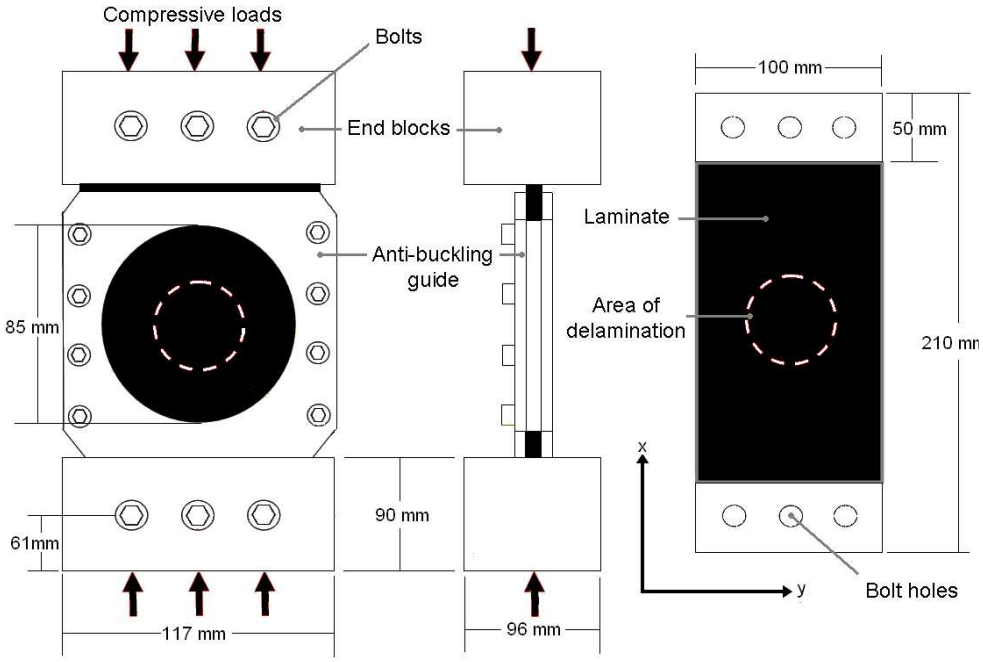

Fig. 29. Experimental set-up and jig.

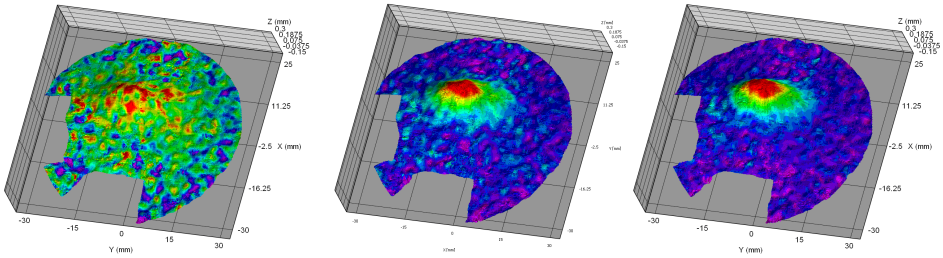

Fig. 30. Three DIC images taken at 50 fps showing displacement contours during delamination buckling of the 90^{o} Outer (2) coupon. The outer edge of the coloured circles represents the anti-buckling guide.

Strains were recorded throughout the testing of the laminates described above by two pairs of back-to-back strain gauges attached to a HBM 600 Hz Spider 8 data acquisition system. Coupons were covered in a random speckle pattern to allow capture of buckling modes and final failure images and video using a Limess VIC-3D HS Digital Image Correlation (DIC) system employing Photron Fastcam

SA3 cameras capable of 2000 FPS at full resolution, see Fig. 30. The coupons were subjected to 8J single impacts in an Instron Dynatup 9250HV instrumented impact tester. The tup used was hemispherical with 16mm diameter. The extent of BVID was captured using an Ultrasonic Sciences Ltd. C-scan system. Resulting maximum damage diameters $l_{\max}$ were 36mm, 37mm, 42.5mm and 42mm for the Control, 45^{o} Outer, 90^{o} Outer (1) and 90^{o} Outer (2) coupons respectively see Fig. 31. Axial compressive load was applied under displacement control from an Instron 5585H test machine until failure. Coupons and their end fixtures are described in Fig. 29. An anti-buckling guide is used in order to prevent global buckling and to ensure samples failed as a result of damage propagation following delamination buckling.

7.2.2. Results

Analytical results for static problems are compared with experimental data in Tables 6, 7 and 8. Experimental failure and analytical propagation strains for laminates from the literature are given in Table 6 with VICONOPT buckling strains and critical sublaminates be described in Table 7. Results for the new experimental coupons are given in Table 8. Results indicate that, with the exception of the UT500/Epoxy (QI) result, which will be discussed in Chapter 7.2.3, the model predicts threshold strain to within 16% (14% for $r = 0.5$) of the experimental values. Table 7 indicates the interface at which propagation takes place by providing the lay-up of the sublaminate for which growth first occurs as well as the associated buckling strain ε^{C}. Failure occurs for the HTA/6376 (BAY) stiffened panel at 5830 μstrain. Note that for the result HTA/6376 (FOOT) propagation first occurs at an experimental strain of 4300 μstrain.

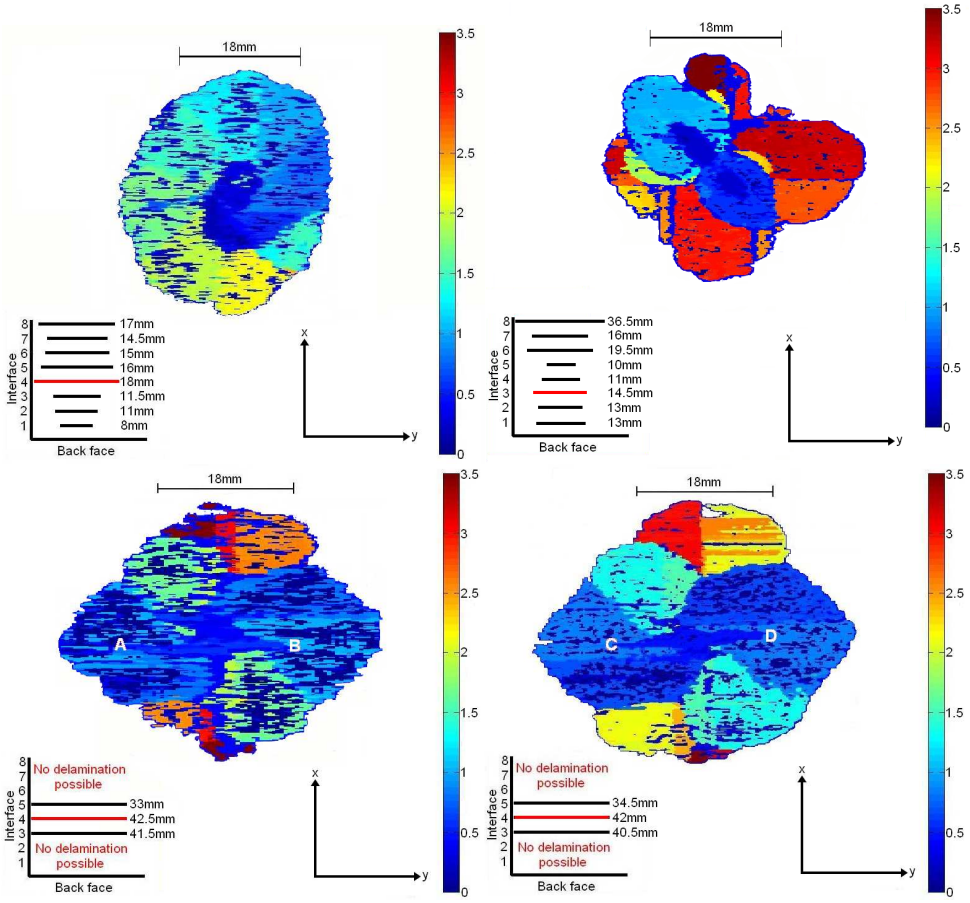

Fig. 31. Ultrasonic C-scan images of BVID with insets showing EDM representations from the non-impact face of (a) the Control , (b) 45^{o} Outer, (c) 90^{o} Outer (1), and (d) 90^{o} Outer (2) coupons. Colour scales relate to through-depth position. Colours toward the top of the scale are closer to the mid-plane of the laminate.

Table 6

Static loading results for laminates described in Chapter 7.2. r is post-buckled stiffness ratio, see Eq. (24).

Material (Laminate ID)	Experimental failure strain (μstrain)	Analytical threshold strain (μstrain)	
		r=0	r=0.5
UT500/Epoxy (QI)	5277†	4074	4144
HTA/6376 (QI14)	5025	4382	4496
HTA/6376 (QI5)	5025	4248	4350
HTA/6376 (ZD)	4439	4542	4588
HTA/6376 (FOOT)	4461	4219	4296
HTA/6376 (BAY)	3550-4810*	3659	3957

†Boundary conditions delay failure, see Chapter 7.2.3.
*Propagation of damage rather than failure occurs between these values.

Table 7

Lay-ups and associated VICONOPT buckling strains for critical sublaminates giving analytical results of Table 6.

Material (Laminate ID)	Lay-up	Buckling strain (μstrain)
UT500/Epoxy (QI)	[45,0,-45]	2764
HTA/6376 (QI14)	[0, 45]	2690
HTA/6376 (QI5)	[0, 45]*	2416*
HTA/6376 (ZD)	[-45, 45,0]	3381
HTA/6376 (FOOT)	[45, -45,0]†	2822†
HTA/6376 (BAY)	[45, -45,0]	1422

*Results for r=0.5 are [0,45,-45], 3008 (μstrain). † Results for r=0.5 are [45,-45,0,90], 2236 (μstrain).

Table 8.

Experimental and analytical VICONOPT buckling and propagation strains for critical sublaminates of the optimised laminates using the Linear and Experimental Damage Models.

Material (Laminate ID)	Sublaminate Lay-up	Buckling strain (μstrain)	Propagation strain (μstrain)	
	LDM/EDM	LDM/EDM	LDM/EDM	Experimental
AS4/8552 (Control)	(45,0,-45) / (45,0,-45)	1143 / 3446	3834 / 4742	5700
AS4/8552 (45^o Outer)	$(45,-45)_3$ / (45,-45)	4037 / 1904	4997 / 6081	5882
AS4/8552 (90^o Outer (1))	$(90_3,45, 90)$* / $(90_3,45)$	6430 / 3014	8238 / 6637	6400
AS4/8552 (90^o Outer (2))	$(90_3,45, 90)$* / $(90_3,45)$	6576 / 3086	8349 / 6656	6200

*The LDM actually gives a lower strain at the 5^{th} level but this is disregarded as it occurs at a -45/-45 interface at which (due to fibre bridging) delamination will not occur.

Control Laminate-$[45,0,-45,90]_{4S}$

Figure 31 (a) shows the C-scan image before the CAI test with l_{max} = 36mm. Following a divergence in strain at 50-60 kN (see fig. 32(a)) relating to Euler buckling contact with the anti-buckling guide occurred between 80-90 kN leading to restiffeneing. Table 8 gives the experimental final failure strain corresponding to a failure load of 107 kN. For the purposes of the EDM the damage diameter at the critical level was 18mm.

45^{o} Outer Laminate-$[(45,-45)_4,(90,0)_4]_S$

Figure 31(b) shows the C-scan image before the CAI test with l_{max} = 37mm. Table 8 gives the nominal experimental propagation strain corresponding to a failure load of 120 kN. Fig. 32(b) shows that following a divergence in strain at 40-50 kN relating to an Euler buckling, contact with the anti-buckling guide occurred between 70-80 kN. For the purposes of the EDM the damage diameter at the critical level was 14.5mm. Gauges 2 and 4 reach the maximum strain input into the data acquisition system at 107 and 111 kN respectively. Hence the projected average strain from this point (dotted line) is continued with the same gradient. Kinks in gauges 1 and 3 at 120 kN show a damage propagation event. Final failure occurred at 150 kN (equivalent to a nominal strain of 7350 μstrain) due to transverse full width cracking; although post compression C-scan images clearly show damage propagation in the four principle fibre directions.

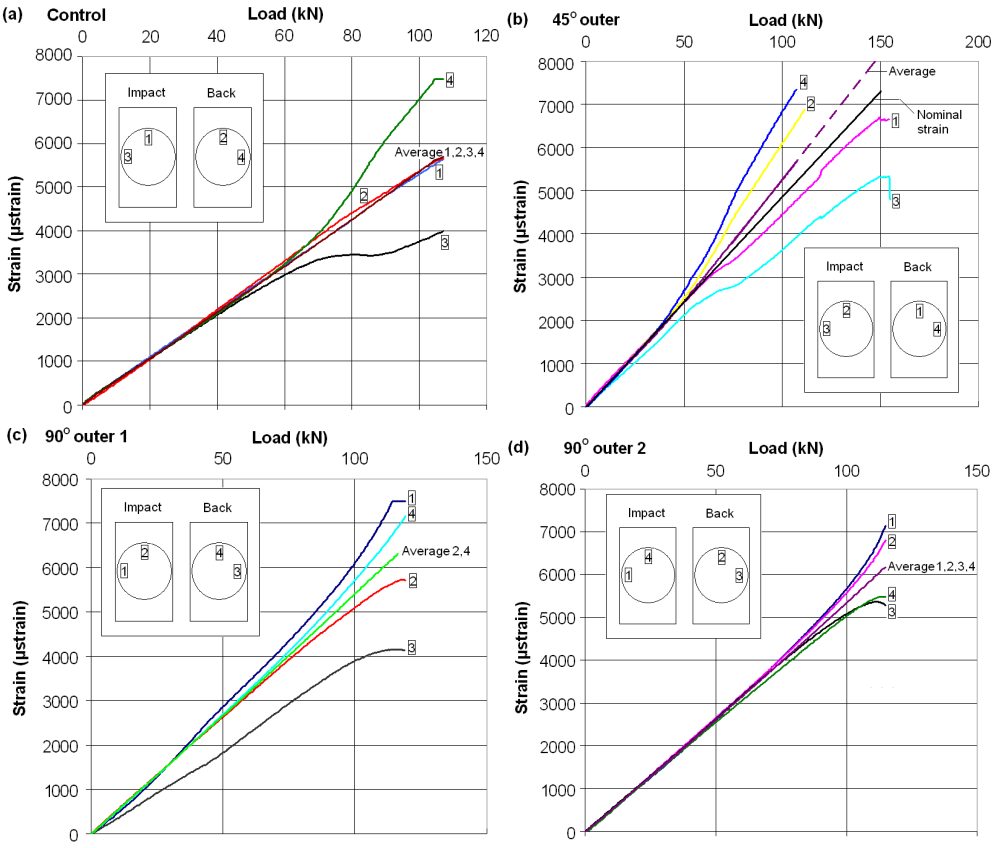

Fig. 32. Strain vs. Load plots for the four coupons with inset showing strain gauge positions: (a) Control, (b) 45° Outer, (c) 90° Outer (1) and (d) 90° Outer (2).

90° Outer (1) Laminate-$[90_3,45,90,-45_3,0,45_3,0_2,-45,0]_S$

Figure 31(c) shows the C-scan image before the CAI test with l_{max} = 42.5mm. An intraply crack 3 layers deep, a result of impact, runs from point A to B on Fig. 31 (c) and was a factor in final failure of the laminate. In Fig. 32(c) channels 1 and 3 are not considered as part of the average strain because channel 3 appears to be anomalous. Table 8 gives the experimental final failure strain corresponding to a failure load of 119 kN. For the purposes of the EDM the damage diameter at the critical level was 42.5mm.

90^{o} Outer (2) Laminate-$[90_3,45,90,-45_3,0,45_3,0_2,-45,0]_S$

Figure 31(d) shows the C-scan image before the CAI test with $l_{\max}$ = 42mm. An intraply crack 3 layers deep, a result of impact, runs from point C to D on Fig. 31 (d) and was a factor in final failure of the laminate. Table 8 gives the experimental final failure strain corresponding to a failure load of 115 kN as shown in Fig. 32(d). For the purposes of the EDM the damage diameter at the critical level was 42mm. Video from the DIC system indicated delamination buckling occurred (frame 2 Fig. 30) shortly before final failure occurred due to transverse full width cracking.

7.2.3. Discussion

The model is compared with experimental results for a range of laminates and structural features with varying damage geometries and diverse properties in regard to input energy, material, lay-up and thickness. For all problems the model was able to predict threshold strain values to an acceptable degree of accuracy.

With the exception of the analytical strain for HTA/6376 (ZD), the threshold strains obtained for the static compression problems are lower than the experimental failure strain. The non-conservativeness of the HTA/6376 (ZD) coupon can most probably be attributed to a combination of factors including the simplicity and inaccuracy of the damage model, the sensitivity of the laminate to ε^C (and hence damage size) and the instability of growth of this coupon, see Chapter 6. Failure generally occurs when damage propagates to the edge of the coupon and not at the threshold strain, which gives initial propagation. In comparison, a similar rationale can be applied to stiffened panels where the prevalent failure mechanism is some degree of stiffener detachment or otherwise damage that is sufficient to cause the stiffener to lose stiffness thus leading to an overall

stiffness loss and finally to global failure. Since damage in the bay would need to propagate under the stiffener to cause detachment (or damage sufficient to compromise the stiffener) a higher strain is necessary to cause failure than for damage under the stiffener foot where propagation causes localised failure of the skin which induces a corresponding stiffness loss immediately without the need for further propagation. This is reinforced by the results. For bay impact, HTA/6376 (BAY), the threshold strain is predicted correctly but the failure strain of 5830 μstrain is significantly higher, whereas for the HTA/6376 (FOOT) failure (4461 μstrain) quickly follows propagation (4300 μstrain) which is accurately predicted to within 5% difference. The UT500/Epoxy (QI) result is influenced by experimental boundary conditions. The $l_{\max}$ damage diameter for this coupon is 27mm in an exposed rectangle of laminate 50mm in width and 35mm in length. Outside this area the coupon is clamped at its ends and is unsupported along its length. The proximity of the clamped edges to the damaged area may well delay failure of the coupon by preventing the delamination from propagating and is thought to explain the poor comparison with the analytical results for this problem.

Unfortunately, the ability of the model to predict at which level crack propagation first occurs remains only partially validated. Only Greenhalgh et al for the HTA/6376 (FOOT) result of the experimental problems records the interface relating to initial propagation. However in this case, the model predicts the interface depth correctly. Note that as laminates tested by the author were tested to failure (in order to determine there damage tolerant failure strain) it was impossible to determine the interface at which propagation first occurred.

As a design application for the analytical model two damage tolerant, manually optimised laminates, AS4/8552 (90^{o} Outer (1) and (2)) and (45^{o} Outer), were considered. The principle for the optimization of

these laminates was based on the two factors identified in Chapter 6.1]; increasing the delaminated plate buckling strain and minimising A_{11}. In the case of the AS4/8552 (45^o Outer) coupon the current industry practice of keeping 90^o fibres away from the surface of the laminate was followed. The AS4/8552 (90^o Outer) (AS4/8552 (45^o Outer)) laminates were designed by putting all the 90^o (±45^o) layers to the outer faces of the laminate, thus increasing buckling resistance. Hence, all the 0^o fibres are positioned away from the critical propagation region which is assumed to be up to 20% depth of the laminate away from the surface. This is because 0^o fibres have the highest A_{11} and tend to cause strain energy to release earlier.

Results for the optimised laminate tests indicate that all laminates failed as a result of propagation of damage following delamination buckling. The 90^o Outer coupons produced an average improvement in strength over the control laminate of 11% and the 45^o Outer laminate gave improvement in strength of 29%, although propagation occurred at about 8% higher load in comparison to the control. Divergence in strain gauge readings at medium levels of load for the Control, 45^o Outer and 90^o Outer (1) coupons is attributed to Euler buckling leading to bending which is then arrested by contact with the anti-buckling guide as can be seen in Fig. 32.

During the analysis of the C-scans of the 45^o Outer coupon it was noted that large delamination damage was not present until the 8th interface, which coincided with the interface of ±45^o fibres and 90^o/0^o fibres. This is an obviously weak interface where stress is likely to be concentrated. It is assumed that the depth of this weak interface and the fact that a large area of damage was ‘drawn’ to it away from the critical damage region (approximately 5-20% of laminate thickness) was a major contributing factor to the strength of the overall laminate. Similarly, the stacking sequence for the 90^o outer coupons and the C-scan images show an obvious weakness is present between the

4^{th} and 5^{th} layers. However, in contrast to the effect on the 45^{o} Outer coupon, the weak 4^{th} interface in the 90^{o} Outer coupons is thought to have significantly reduced their CAI strength. This may be a factor to consider in future optimisation strategies. Impacts on the 90^{o} Outer laminates produced almost identical damage morphologies as can be seen from Figs. 31(c) and (d). The limited possible interfaces (due to ply blocking) in these coupons at which delamination could occur following impact resulted in impact energy being dispersed over a smaller number of interfaces and hence the area of each delamination had to be larger. Both 90^{o} Outer laminates were also subject to large intraply cracks through the non-impact outer layers which almost certainly had a negative effect on the strength of the laminate.

The LDM analytical results differ from the experimental results by 33%, 32%, 29% and 35% for the Control, 45^{o} Outer, 90^{o} Outer (1) and 90^{o} Outer (2) respectively. Clearly, the LDM does not work well for the more exotic stacking sequences presented here which include blocks of layers with the same orientation and unusual damage morphologies. This is probably due to the inflexibility of the LDM with regard to position of the largest damage diameter. This weakness in damage morphology modelling was exploited by the optimisation procedure to derive optimised laminates. The performance of the 90^{o} Outer coupons could also have been affected by the ASTM standard rectangular impact test window over which coupons were placed during impact. The rectangular shape reduced the length over which 90^{o} fibres bent during impact which in turn increased their bending stiffness when compared to the 0^{o} fibres. This may have caused larger delaminations than assumed by the LDM (and would probably occur in service) to occur closer to the back face (where bending forces peak during impact) thus resulting in an earlier failure than if impact had been over a square window.

However, results can be improved by careful study of the C-scan images to derive the correct damage diameter for each interface see Fig. 31. Results for initial propagation using the EDM differ by 17%, 2%, 4% and 7% for the Control, 45^o Outer, 90^o Outer (1) and 90^o Outer (2) laminates respectively. The EDM analysis using the C-scan data was able to capture particularly well the events up to and including failure in the 45^o Outer compression test. Note that analysis in [73] shows delamination growth to be stable if the inequality $3\varepsilon^c < \varepsilon_{th}$ holds. This inequality does indeed hold for the 2nd interface in the 45^o Outer coupon which is thought to be linked to the propagation event at 120 kN (a nominal strain of 5882 μstrain) evident as a jump in readings on the load-strain plot. As the growth at the second level is stable it is unlikely to be the cause of final failure hence propagation at other levels needs to be considered. The level with second lowest propagation strain and hence next to propagate is the unstable 3rd interface with sublaminate lay-up (45,-45,45) which buckles at 5874 μstrain and has a threshold strain of 7198 which differs by only 2% from the experimental failure strain. Similarly, for the control coupon, propagation at the 2nd interface (4310 μstrain) is predicted to be briefly unstable before becoming stable which is then followed by unstable growth at the 3rd interface. Due to the inherent difficulty in accurate sizing individual delamination areas and the effect this has on calculated strains it is quite likely that propagation at the 2nd level is in fact purely stable which would correlate with experimental results. Note that it is likely that detailed C-scans will be difficult if not impossible to capture in in-service situations and thus is not a predictive strategy.

7.2.4. Conclusions

When applied in conjunction with a simple linear representation of damage (LDM) used when detailed through depth delamination

information is unavailable the analytical model is accurate to within 16% of experimental values for static strength in a variety of materials and structural types with realistic boundary conditions. Results from [14] indicate that impacts under the stiffener foot of a stiffened panel are more serious than those to the bay i.e. the reduction in strength associated with impacts under the stiffener foot is much greater than that attributed to bay impacts. Hence modelling of the former problem is more important and here the model gives an accurate, slightly conservative result.

Experimental results demonstrate increases of 8% and 29% in damage tolerant strain can be achieved by replacing a standard $[45,0,-45,90]_{4S}$ laminate with $[90_3,45,90,-45_3,0,45_3,0_2,-45,0]_S$ and $[(45,-45)_4,(90,0)_4]_S$ laminates, respectively. However, stable propagation of damage was observed in the laminate with 45^o material outermost. The results also show that the propagation model is capable in its current form of making qualitative predictions about CAI using the LDM and so is a legitimate basis for an optimisation routine designed for damage tolerance.

The optimised stacking sequences have identified a weakness in the damage modelling. However, it has been shown that this weakness can be ameliorated by using experimental C-scan data. This though is clearly not yet a predictive strategy and so is not applicable to an optimisation procedure. Nevertheless, the model could in conjunction with an accurate damage prediction strategy provide an excellent tool for designing laminates in the future and could reduce the need for expensive and time consuming testing.

7.3. Static free edge problems

7.3.1. Experimental details

A stiffener similar to those used in Liu et al [78] was manufactured from Cytec UTS/977-2 uni-directional pre-preg layers with material properties given in Table 1 and stiffener blade stacking sequence of $[45/0/-45/0_3/90/0_2/90/0_3/-45/0/45]_s$.

Following preliminary tests to determine energy levels required for BVID the stiffener was subjected to single in-plane impacts, two 10J and one 11J applied at the through-thickness centre of the free edge at three separate locations along the *x*-axis, see Fig. 33. An Instron Dynatup 9250HV instrumented impact tester was used. The tup used was hemispherical with diameter 16mm and was connected to a rigid steel rod allowing precise placement of the impact location at the centre of the stiffener edge. Figure 33 shows the set up for impact testing and primary dimensions for the cross section of the stiffener. To simulate boundary conditions similar to those found in real applications and to prevent excessive vibrations during impact, the stiffener was bolted to a steel backing plate, which was then clamped to the machine.

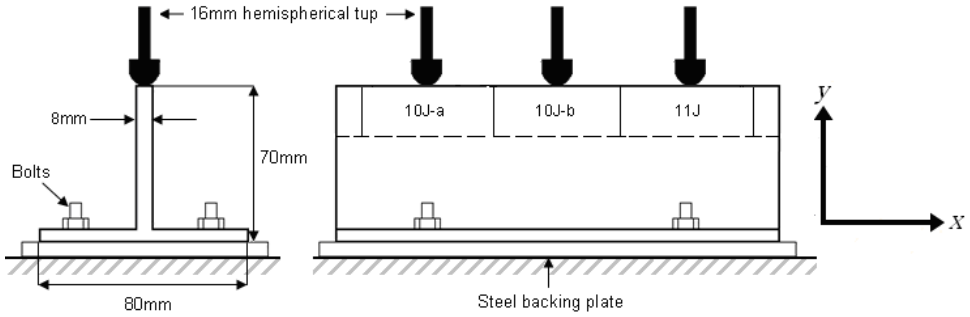

Fig. 33. Impact test set up and primary dimensions of stiffener.

In addition, to ensure only a single impact of known energy was delivered, a pneumatic anti-bounce mechanism was used to catch the tup assembly after the first controlled impact. Following impact, the extent and location of BVID was measured using an Ultrasonic Sciences Ltd. C-scan system with a 350 MHz ultrasonic probe. For testing purposes, the stiffener blade was sectioned into three coupons measuring 162mm in length with the damaged region at the centre of each. To allow for propagation of the delaminations, the width of the sections was initially set at 32.5mm for the first 10J specimen (referred to as 10J-*a*). Subsequently, to reduce the load necessary for failure, the width was reduced to 26.5mm for the 11J and a second 10J specimen (10J-*b*).

To reduce crushing at the loading points, provide grip and to prevent slipping of the test piece coupons were tabbed at both ends with 35mm or 40mm strips of emery tape before being hydraulically clamped. An axial compressive load was applied under load control, using a constant ramp input, from an Instron 1332 test machine until initial propagation or in the case of the coupons 10J-*a* and 10J-*b*, until failure. To ensure that failure was through propagation of the sublaminate following delamination buckling and to prevent global buckling, the gauge length was reduced to a maximum of 92mm, see Fig. 34. Note that due to the small physical distances associated with microstrain control over a gauge length of 92mm the test machine was unable to maintain exact displacements under displacement control and the output was not smooth. Hence load control was preferred for its smooth output.

Strains were recorded throughout the tests by two pairs of back-to-back longitudinal strain gauges and either one or two transverse strain gauges connected to a HBM 600 Hz Spider 8 data acquisition system. The locations of the gauges for the specimens are described in Fig. 34 and repeated on the load vs strain plots (Fig.36). On all of

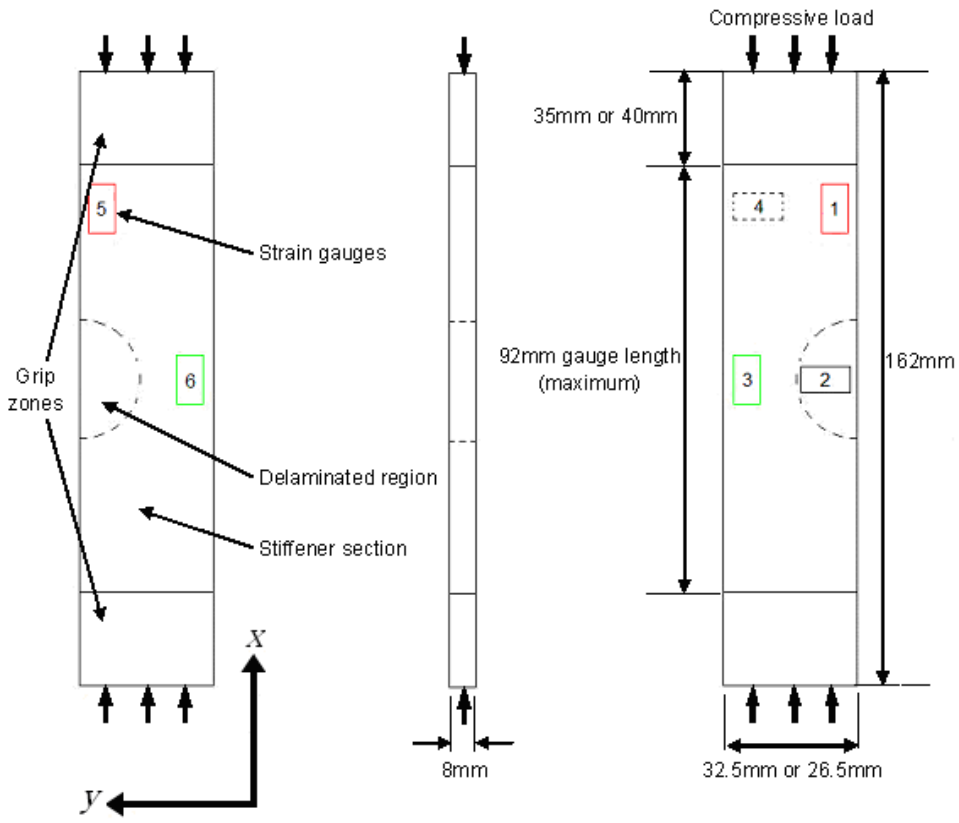

Fig. 34. Front, side and back views of coupons for CAI test.

the specimens, a transverse gauge was located over the damaged region to enable the calculation of the Poisson's ratio strains in this region. A second transverse gauge was added to the 10J-*b* and 11J coupons to allow comparison with far field Poisson's ratio strains. Specimens were covered in a random speckle pattern to allow capture of buckling modes and final failure images and video using a Limess VIC-3D HS Digital Image Correlation (DIC) system employing Photron Fastcam SA3 cameras, capable of 2000fps at full resolution.

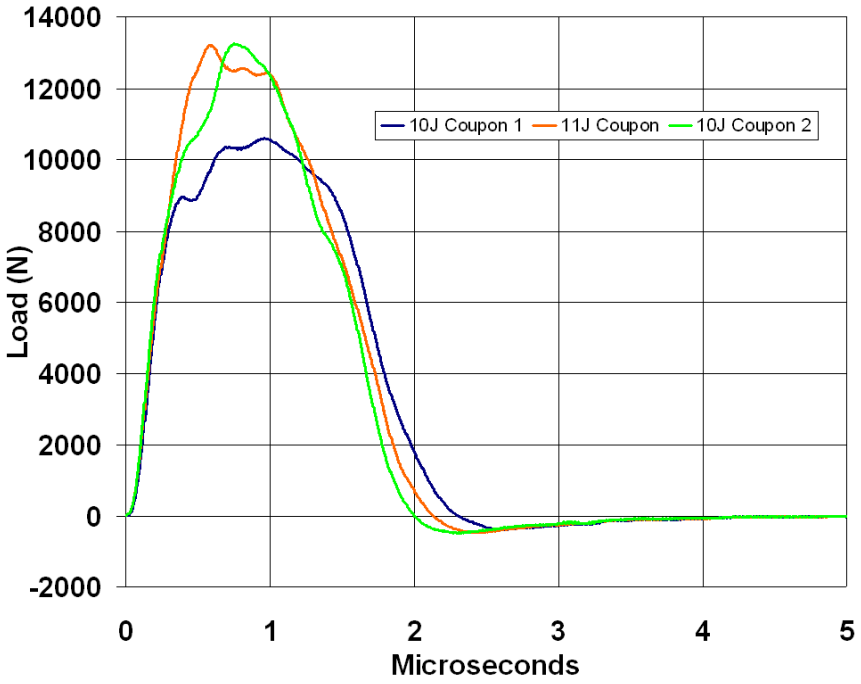

Fig. 35. Graph of Load vs. time for impacts on the 3 optimised coupons.

7.3.2. Results

Impact test results

Impact damage was consistent in area, morphology (see Fig. 8) and dent depth for all three coupons. The damage size recorded had approximately *a*=45mm and *b*=17mm for all coupons, see Figs. 8 (a) and (b). An inspection of the free edge of all three coupons following impact showed evidence of delamination that indicated damage was not symmetrically distributed about the mid-plane. Figure 35 shows force/time graphs for edge impacts on the three coupons. Peak impact forces are identical for the 11J coupon and 10J-*b* coupon. The peak impact force for the 10J-*a* coupon is considerably lower than for the 10J-*b* coupon.

Maximum dent depths of 0.15mm, 0.17mm and 0.15mm were recorded for the 10J-*a* coupon, 10J-*b* coupon and 11J coupon respectively. The average diameters of the circular dents were 6.7mm, 7.8mm and 6.8mm respectively.

Compression after impact (CAI) test results

DIC images, taken from the post-buckling test phase of the 10J-a specimen showing local delamination buckling, can be seen in Fig. 36. Two cross-sections of the buckled region in two orthogonal planes are also shown. These images show local buckling of a symmetric semi-elliptical delamination which is followed by propagation as a result of this local buckling occurring in subsequent images. This justifies the thin-film assumption made in the buckling model. Table 9 gives a summary of buckling, propagation and failure loads and nominal strains taken from the load vs. strain plots in Fig. 37.

Here nominal strain is calculated using applied load, measured cross-sectional area and the effective laminate stiffness, calculated from the ideal material properties given in Table 1 and assuming $N_y = 0$. It is expected that strains from individual test pieces will differ from this strain to some degree.

The buckling strain range for the 10J-b coupon is larger than the other coupons because it was harder to determine due to divergence in strain occurring from the outset. Initial propagation is associated with kinks in the load vs. strain curves in Fig. 37. A final failure strain was not recorded for the 11J coupon as the test was halted before failure occurred. Note that the kink that occurs at 18 kN in the curve for Gauge 1 in Fig. 37 (b) is attributed to noise in the strain gauge input as opposed to a physical event as it only occurs in a single gauge and afterwards it returns to the correct gradient.

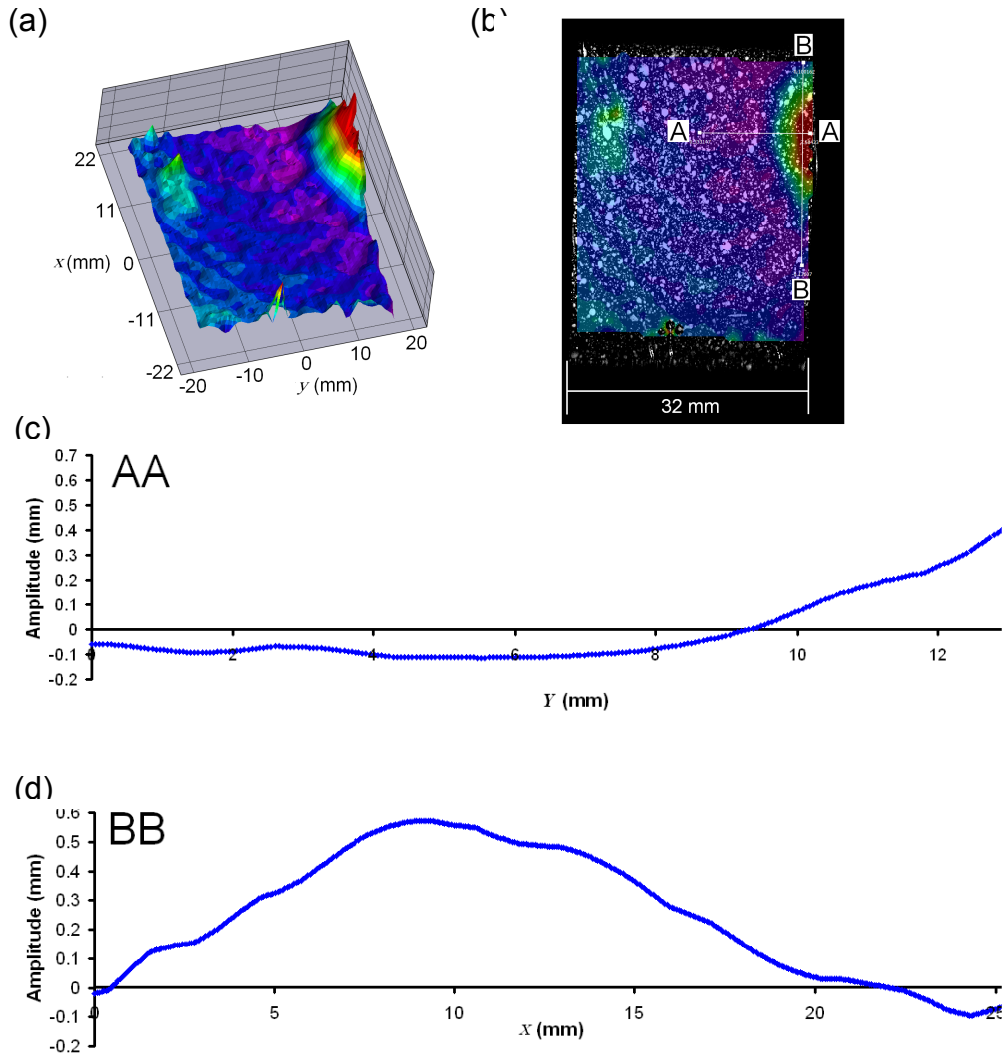

Fig. 36. (a) and (b) show 3D and 2D DIC images of the 10J-a coupon during the post-buckling phase respectively. Figures (c) and (d) show cross sections of (b) in planes AA and BB respectively which in turn indicate the amplitude of the local buckling of the delaminated region. In all cases, the free edge is the edge along which deformation is maximum.

Table 9

Experimental values of load and nominal strain for buckling, propagation and failure of the three coupons.

	Buckling		Propagation		Failure	
Coupon	Load (kN)	Strain (μstrain)	Load (kN)	Strain (μstrain)	Load (kN)	Strain (μstrain)
10J-*a**	22-26	1100-1200	89	4160	93	4400
10J-*b*	18-26	1100-1500	68	3960	74	4370
11J	20-22	1000-1200	78	4540	N/A	N/A

* Note that the width of 10J-*a* specimen is 18.5% lower than the 10J-b and 11J, see Chapter 7.3.1.

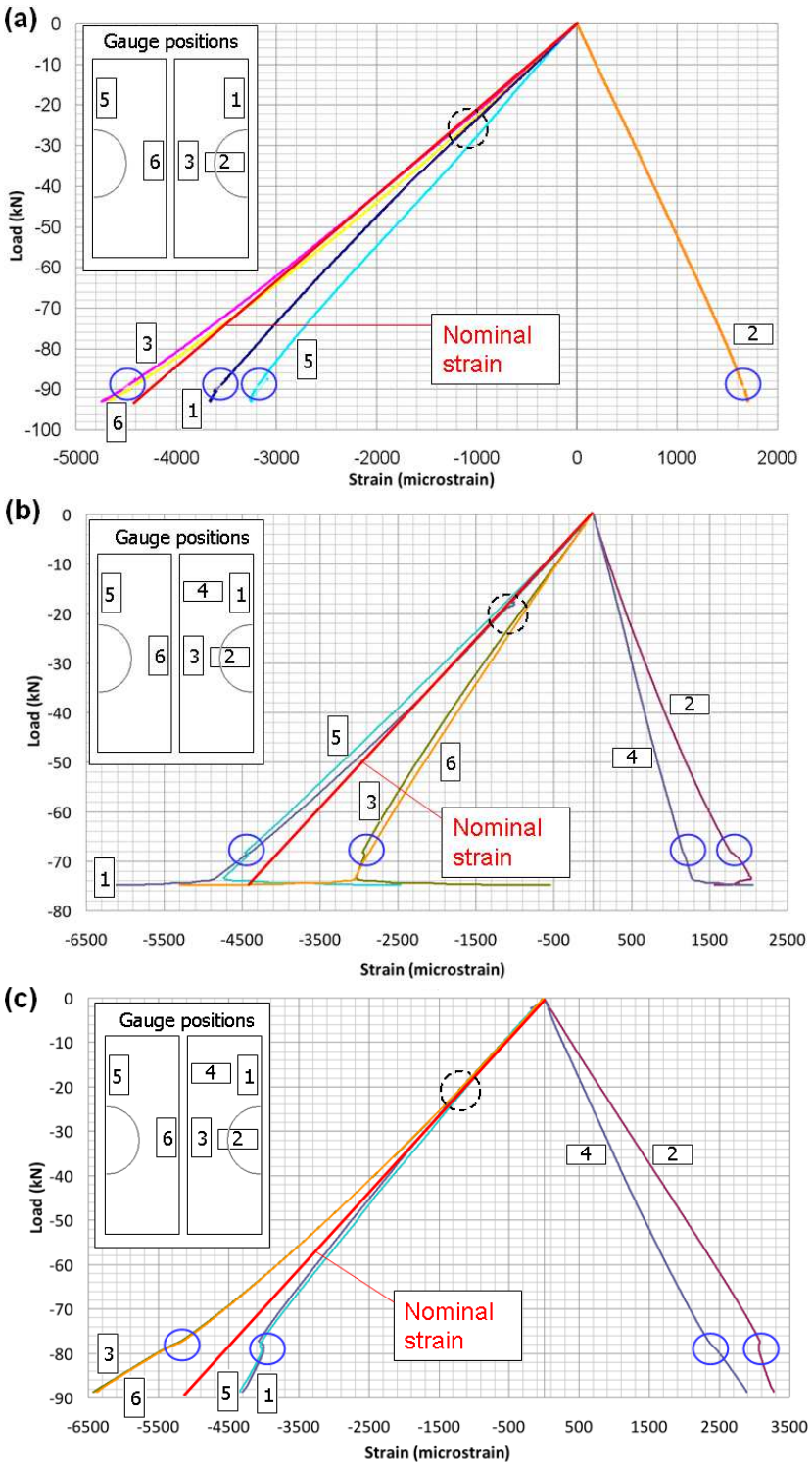

Fig. 37. Load vs. strain plots for the (a) 10J-*a*, (b) 10J-*b* and (c) 11J coupons. Dashed circles highlight initial buckling, small circles highlight propagation.

Analytical results

Analytical threshold strain results are shown in Fig. 38 for the outermost seven layers of the laminate with a comparison to the experimental results. Layers 4-6 (0_3) are blocked together in Fig. 38 as it is unlikely that delamination will have occurred at the interfaces contained within the block. As a difference in ply angle between adjacent layers is required for delamination to occur. Fig. 38 shows that the interface with lowest propagation strain, where delamination is likely to occur, is the third interface and this is where delamination

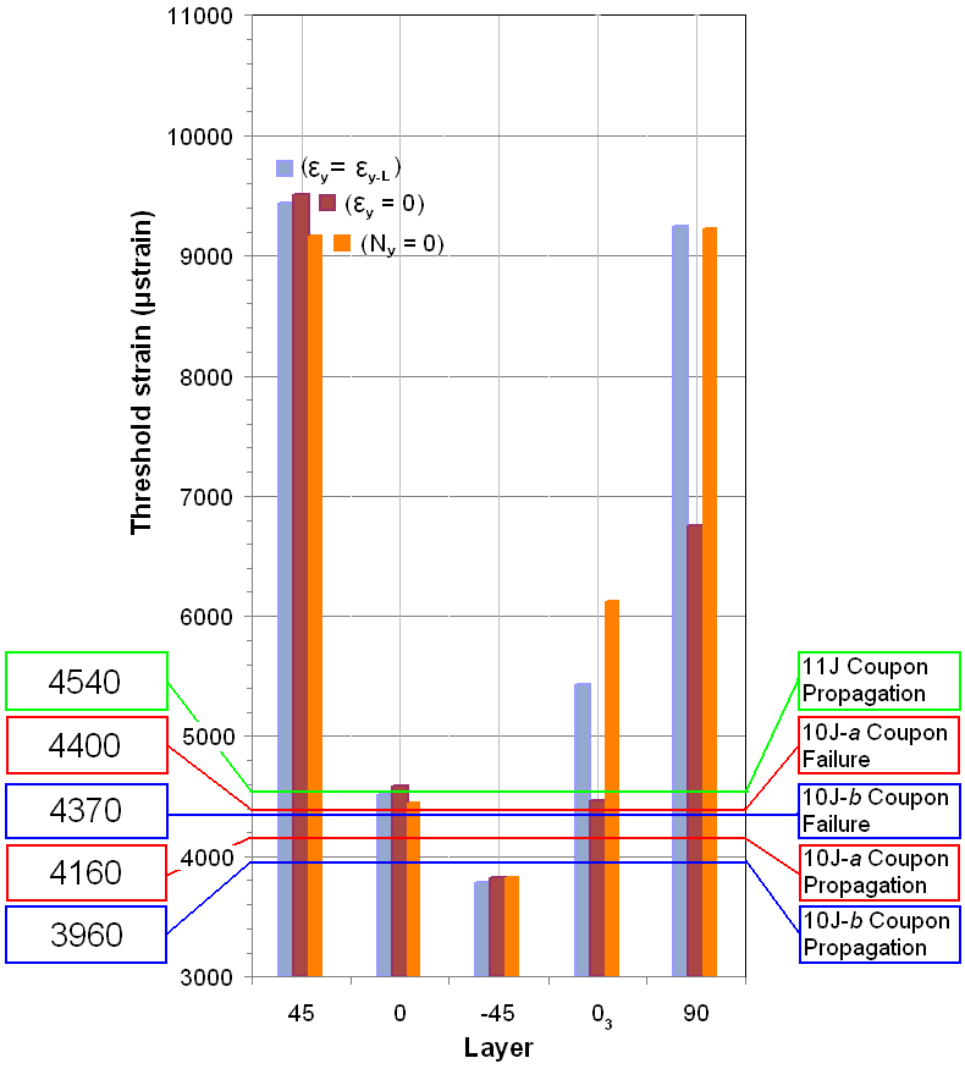

Fig. 38. Comparison of the CAI model with various initial conditions (bars) and experimental results (horizontal lines).

propagation is assumed to occur. The value of propagation strain at this level is similar for all initial conditions.

7.3.3. Discussion

Prior to impact a visual inspection of the 10J coupons indicated the presence of two tubular shaped voids occurring symmetrically at the third interface in from either side of the coupon. Using strain gauge positioning in Fig. 37 for orientation and following cutting of the coupons from the stiffener (see Fig. 33). an inspection of the cut surfaces revealed the following. The void in the 10J-*a* coupon nearest the surface with gauges 5 and 6 (gauges 1,2 and 3) attached tapered linearly from an approximately elliptical cross-section of 7mm (4mm) major diameter by 1mm (1mm) minor diameter (with the major diameter in the (x,y)-plane) through to an elliptical cross-section of 1mm by 0.2mm (no void was visible on the 1,2 and 3 gauge side) at the join with 10J-*b* coupon. No evidence of the voids was found at the junction between the 10J-*b* and 11J coupons or in the 11J coupon as a whole. The tops of both elliptical voids were approximately 0.2mm from the free edge. The voids can be seen as a thin band close to the free edge on the C-scan of the 10J-*a* coupon in Fig. 8 (b). In addition to the above, cracks along the free edge at the mid-plane and above the voids were also noted in the 10J-*b* coupon.

The larger size of the manufacturing defects in the 10J-*a* coupon may have reduced its strength. However, the effect was not thought to have been significant, i.e. it weakened the 10J-*a* coupon but did not as such cause failure. This is due to the small width (y-direction) of the defect (average 4mm) in comparison to the damage width (maximum 17mm). The defects are thought to have had minimal or no influence on the other two coupons in which little or no voiding was observed.

Following [15] kinking in the impact load vs. time plots is attributed to delaminations forming at various interfaces throughout the laminate. The lower peak impact load seen in Fig. 35 for the 10J-*a* coupon is attributed to the manufacturing fault in this coupon.

Figure 12(b) shows a general semi-elliptical buckling mode from VICONOPT that agrees well with the C-scans of the delamination areas (Fig. 11) and Digital Image Correlation (DIC) buckling mode images (Fig. 36). Different analytical values for buckling derived from the individual initial conditions bound the experimentally reported buckling strain values for all three coupons with upper and lower limits given by the $N_y = 0$ and $\varepsilon_y = 0$ conditions, respectively.

As different impact energies have been shown to produce almost identical areas (see Fig. 8(a) and (b)) it is suggested that free edge damage may be more dependent on tup geometry than on impact energy. However, this may be an effect of the voids present in the stiffener producing larger than expected damage areas.

The similarity in strain within the back to back pairs of gauges in Figs. 37 (a)-(c) indicates that the gauge length of the specimens was sufficient to negate global buckling. Divergence in strain between the pairs of back to back strain gauges is seen in Figs. 37 (a)-(c) and is attributed to the loss in stiffness of one side of the test piece following delamination buckling. Divergence in the transverse gauges in the 10J-*b* and 11J coupons is attributed to the difference in stiffness over the damage area compared to the stiffness in the area where the far-field strain was measured.

Experimental initial propagation and final failure strains for the 10J coupons are very similar and hence some repeatability is established. The slight difference in initial propagation strains could be attributed to the presence of the manufacturing defects or the extent of damage in the two coupons at the third interface. The fact

that this difference is much reduced when final failure occurs may suggest that final failure did not occur at the third interface. This is supported by an analysis of the stability of growth (Chapter 6) at this level which implies growth is either stable (i.e. for further growth to occur load must be continually increased) or briefly unstable (i.e. a delamination will continue to propagate, once at a certain level of load without further load being applied) before becoming stable depending on the initial conditions chosen as illustrated in Fig. 39. The curves in Fig. 39 are calculated by fixing A_{11} and $\varepsilon = \varepsilon_{th}$ in Eq. (29) at the values appropriate for the sublaminate in question and then varying ε^c to determine G_I. The boundary conditions $(\varepsilon_y = 0)$ and $(N_y = 0)$ produce the same threshold strain and hence the same SERR curve. Note that analysis in [72] shows delamination growth to be stable if the inequality $\varepsilon^c < \varepsilon_{th}/3$, which represents the horizontal coordinate of the maximum value of the curves in Fig. 39, holds. It is assumed that as damage propagation occurs the increase in area of the delaminated region leads to a drop in buckling strain ε^c. Hence, it can be seen that for ε_{th} = 3825 μstrain, the SERR remains above the propagation threshold G_{IC}, relating to unstable growth (no increase in load/strain is required for propagation) before returning below it when the delamination area reaches a critical size. Alternatively, for ε_{th} = 3780 μstrain, the SERR remains below G_{IC}, indicating more energy is required for further delamination and hence growth is stable.

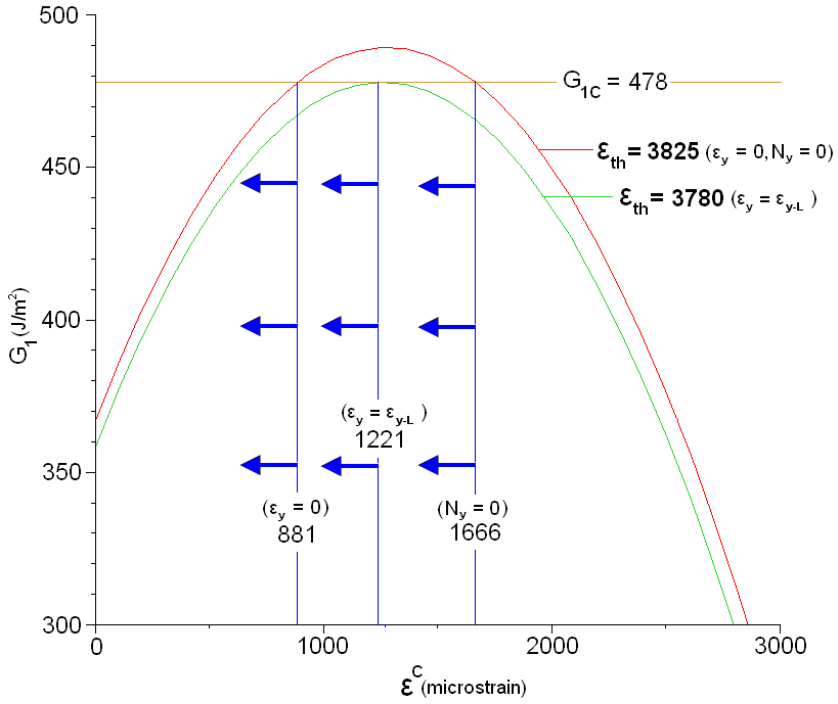

Fig. 39. Strain energy release rate for propagation at the third interface where curves are upper and lower bounds on the threshold strains derived for the various initial conditions considered. Vertical lines represent buckling strains associated with these initial conditions. Arrows indicate a drop in buckling strain due to damage propagation.

Noting the proximity of the final failure strains of the 10J coupons to the theoretical threshold strain at the second interface, see Fig. 38, it could be inferred that final failure occurred at this level. However, growth at this level is certainly stable as, in this case, 350 μstrain < ε^C < 580 μstrain depending on the chosen initial conditions. The interface with the next lowest threshold strain at which a delamination could propagate unstably is interface 6. Threshold strains at this level are all considerably larger than the experimental value, apart from the $\varepsilon_y = 0$ condition which gives a remarkably accurate and conservative result for final failure of the 10J coupons with ε^C = 4050 μstrain and ε_{th} = 4463 μstrain. However, it is noted that VICONOPT is

a linear buckling program and as such does not predict any post-buckling effects that would occur at the third level before and during propagation. In addition, any change of mode shape during post-buckling would reduce the energy in the buckle and hence the energy available for propagation thus increasing the strain at which propagation occurs. If final failure were to follow unstable propagation at the sixth interface it should be noted that buckling at this level would occur at reduced strain due to the post-buckling loss in stiffness of the first three layers and hence the predicted propagation strain would be reduced.

Consequently, for absolute conservativeness theoretical threshold strains are reported as 3780 μstrain for all three coupons. Further to the above with reference to Fig. 38 it is noted that the $\varepsilon_y = 0$ condition is the most consistently conservative initial condition.

An inspection of Fig. 17 clearly shows that the objective of optimising threshold strain, and hence maximising CAI strength is principally accomplished by minimising A_{11} and secondly by maximising ε^C for the outermost layers. Employing the above, whilst using the same ply-percentages as the stiffener sections described in this Chapter, an optimised stacking sequence $[45/90_2/0_4/-45/45/0_4/-45/0_2]_s$ has been derived.

Assuming the same damage morphology seen in the experimental coupons and applying the CAI model with a conservative $\varepsilon_y = 0$ initial condition, damage in this laminate theoretically propagates at the seventh interface with ε_{th} = 6164 μstrain. Hence it produces a theoretical 63% increase in CAI strength in comparison to the analytical threshold strain, 3780 μstrain, calculated for the third interface of the original stiffener. In comparison to the highest recorded experimental strain 4540 μstrain for the 11J coupon an increase of 35% is predicted. If the less conservative initial condition

$N_y = 0$ is considered then a threshold strain of 6956 μstrain is recorded at the third interface. This threshold strain corresponds to an increase in CAI strength over the analytical threshold strain for the original stiffener of up to 84%. An improvement over the maximum experimentally derived threshold strain of up to 53% is also predicted.

Finally, it is noted that the optimised laminate suggested may exhibit some bend-twist coupling. It is possible that this may reduce the experimental threshold strain of the laminate.

7.3.4. Conclusions

A first attempt was made to model BVID propagation in an edge impacted T-stiffener. To provide experimental validation for the modelling, as none was available in the literature, a composite T-stiffener was impacted in three locations (two 10J impacts and one 11J) separated spatially from each other so as to avoid interconnected damage morphology. Three coupons containing the separate damage areas were cut from the stiffener and placed in compression until initial propagation (and then final failure for the coupons with 10J impacts). Experimental results for compression of the three stiffener sections have shown consistent damage areas and dent depths. Static strength (damage propagation) results for the three coupons differ by a maximum of 15%.

Using a simple approximation to complex free edge damage morphology an accurate and fast approach for calculating the static strength of coupons following edge impact has been derived. The model has conservatively predicted the static strength of the above coupons to within 4.5%, 9% and 17% for the 10J-*a*, 10J-*b* and 11J coupons respectively. It is noted that the model remained a lower bound to the coupon with a manufacturing defect and that the effect

of varying initial loading conditions has been explored. However, both the conservativeness of the model when applied to coupons with manufacturing defects and the correct choice of initial conditions, particularly in terms of conservativeness, will require further experimental validation.

Assuming damage morphology seen in the experimental coupons in this paper, an optimisation methodology, based on the above CAI model, has derived a stacking sequence $[45/90_2/0_4/\text{-}45/45/0_4/\text{-}45/0_2]_s$ which produces, depending on choice of initial conditions, an increase in CAI strength of up to 84% in comparison to the analytical threshold strain, 3780 μstrain, calculated for the original stiffener. In addition, when compared to the highest recorded experimental threshold strain, 4540 μstrain for the 11J coupon, an increase of up to 53% is seen. The optimised laminate was designed via a re-distribution of the existing plies in the experimental stiffener sections and so maintains the same in-plane stiffness.

Summary

Chapter 7 has dealt with the remaining objectives (5, 6 and 7) from Chapter 2. In part objective 4; to investigate the sensitivity (robustness) of the model to problem parameters including material properties and damage shape, area and depth has also been experimentally tested. This is different to the analytical treatment given in Chapter 6 and does more to establish the robustness of the model by applying it to a variety of laminates with differing materials and BVID sizes under two loading regimes.

Chapter 7 clearly fulfills objective 5 by identifying various problems in the literature suitable for validation of the model, or where no suitable problem was found (i.e. in the case of the in-plane free edge impact which is only lightly researched) experimental testing instead was undertaken instead.

Using results derived in Chapter 6 candidate optimised laminate stacking sequences were identified that theoretically improved damage tolerance or CAI strength for all loading regimes and types of BVID (enclosed or free edge). Only the two stacking sequences derived for the enclosed delaminations subject to static compressive loading were tested. However, as noted in Chapter 9 a series of tests is planned to verify predictions made about possible static strength increases for free edge BVID problems.

8. Final Discussion

A model for CAI strength of composites structures has been developed that when applicable covers a considerable range of BVID problems and is both computationally efficient and simple in application. It is the objective of this chapter to further discuss when the model *is* applicable and the implications of the assumptions integral to its derivation.

The first assumption to be discussed is the thin-film assumption. This assumption requires that no energy be released from the base of the laminate during delamination propagation. In practice this equates to the requirement that delaminations buckle locally and no curvature is introduced into the base laminate. Hence ensuring no moment is placed on the sublaminate which would result in bending energy in the base being available to cause delamination propagation. For the problems modeled in this thesis this assumption can be shown to be correct by considering strain gauge readings and DIC images. Thus with regard to the thin-film assumption the model is applicable to the problems covered in this thesis. In addition, as laminates (and hence buckled sublaminates) considered in this work are relatively thin in comparison to those used in real aircraft structures it is likely that the thin-film assumption will hold in practice too.

Currently the model assumes that only axial load is applied to the laminates (although VICONOPT is capable of calculating buckling strains under mixed loading). This assumption approximates loading in an aircraft wing which is generally dominated (particularly in the 'once in a lifetime' manoeuvres when the static strength of a wing containing BVID would be tested) by loading on a single axis. However, in reality mixed axis loading occurs in all situations and the model, if it is to applied to real aircraft, will need to consider the

implications of this more carefully. It would also need to be understood how well a flat structure under axial load approximates an aircraft structure that may be subject to bending loads too. Note that the axial load should be an excellent approximation in all situations to the loading on an in-service stiffener.

Aside from bending loads causing curvature in aircraft structures curvature is also found in wing skins as part of the aerofoil design. This tests the implicit assumption in the model (as it was initially developed to analyse BVID in flat coupons) that no curvature is present in the base or sublaminate. Under pure axial loading normal to the plane of curvature the model and thin film assumption may successfully approximate a curved component as no bending moment would be applied to the sublaminate due to the high second moment of area and hence bending stiffness associated with a curved structures. However, for multi-axial or bending loads further investigation and extended models may be required.

A number of models have been produced to approximate the damage morphology found in composite structures containing BVID. These models required differing amounts of initial data and were generally more accurate when detailed C-scans were available to inform them. However, the models were *required* to become more accurate as the stacking sequences tested (due to the optimisation routines used to create them) diverged from that of the standard Control sequence: $[45/0/-45/90]_{4s}$. This is because through-thickness delamination distributions were no longer well approximated by the Linear Damage Model (LDM) (itself based on the often seen “Christmas tree” damage distribution see Fig. 2) and individual delamination positions needed to be determined. In fact, although optimisation based on the model has been proven to produce laminates with improved CAI strength the stacking sequences produced have exploited assumptions made about the damage

morphology. In the case of optimised laminates in this thesis, the LDM was used as an assumed damaged distribution. This implied small (in comparison to the largest delamination present) near surface delaminations were part of the damage morphology which proved to be an underestimate in the case of the 90's Outer coupons and an overestimate in the case of the 45's Outer coupon.

A mode of failure, unaccounted for in the modelling, is multi-layer buckling where multiple layers buckle in turn into the space left by the layer above buckling. A specific overlapping through thickness delamination distribution is required which may only be found in particular stacking sequences. However, in theory this failure mechanism could considerably reduce compression after impact strength and will need to be modeled (or avoided) in future optimisation attempts.

Hence, a key finding that has come from this work is that optimisation of laminates for damage tolerance requires a model capable of predicting propagation of given damage but also a model capable of predicting the damage morphology of an impacted laminate. Otherwise, as has been demonstrated, optimisation will frequently produce laminates that are only optimal for the initially suggested damage distribution. Damage tolerance and impact damage morphology are inextricably linked altering one will alter the other. They need to be considered together to form a truly predictive strategy for damage tolerance.

Finally, the model assumes an out-of-plane buckle which causes delamination propagation under Mode-I conditions. This type of buckle occurs under pure axial loading. However, under mixed loading buckling can occur in-plane as shear buckling, which although would be predicted by VICONOPT would not propagate under Mode-I conditions and hence the propagation model would not apply.

9. Final Conclusions

All aims of the thesis have been met to a satisfactory degree and the following key conclusions have been drawn.

The propagation model is based on the assumption that the growth of BVID can be simplified to propagation at a single level within the laminate and is dependent on only three parameters of the problem G_{1C}, ε^C and A_{11}. In a fatigue loading regime where the propagation model is applied as a quasi-static approximation to the conditions apparent in the final rapid stages of fatigue damage growth and assuming no post-buckled stiffness ($r = 0$), the propagation model predicts threshold strain (which for fatigue problems coincides with the failure strain as it is assumed that component in question would be in the final rapid stages of growth) with at most a 4% error compared to experimental values for the laminates tested and is within 1% for some cases. When applied in conjunction with a simple linear representation of damage the analytical model is accurate to within 16% of experimental values for static strength in a variety of materials and structural types with realistic boundary conditions. Results from [14] indicate that impacts under the stiffener foot of a stiffened panel are more serious than those to the bay i.e. the reduction in strength associated with impacts under the stiffener foot is much greater than that attributed to bay impacts. Hence modelling of the former problem is more important and here the model gives an accurate, slightly conservative result.

Experimental results demonstrate increases of 8% and 29% in damage tolerant strain can be achieved by replacing a standard $[45,0,-45,90]_{4S}$ laminate with $[90_3,45,90,-45_3,0,45_3,0_2,-45,0]_S$ and $[(45,-45)_4,(90,0)_4]_S$ laminates, respectively. However, stable

propagation of damage was observed in the laminate with 45^{o} material outermost. The results also show that the propagation model is capable in its current form of making qualitative predictions about CAI using the Linear Damage Model and so is a legitimate basis for an optimisation routine designed for damage tolerance. Further analysis of the model was able to offer some insight into the sensitivity of laminates to errors in the statement of the initial problem and also to predict the stability of growth immediately after the initiation of propagation.

The optimised stacking sequences have identified a weakness in the damage modelling. However, it has been shown that this weakness can be ameliorated by using experimental C-scan data. However, this is clearly not yet a predictive strategy and so is not applicable to an optimisation procedure. Nevertheless, the model could provide an excellent tool for designing laminates in the future and could remove the need for expensive and time consuming testing.

Using a simple approximation to complex free edge damage morphology an accurate and fast approach for calculating the static strength of coupons following edge impact has been derived. The model has conservatively predicted the experimental static strength to within 4.5%, 9% and 17% of the 10J-*a*, 10J-*b* and 11J coupons respectively. It is noted that the model remained a lower bound to the coupon with a manufacturing defect and that the effect of varying initial loading conditions has been explored. However, both the conservativeness of the model when applied to coupons with manufacturing defects and the correct choice of initial conditions, particularly in terms of conservativeness, will require further experimental validation.

Applying the model to a laminate with damage tolerant 45^{o}/-45^{o} layers protecting the 0^{o}/90^{o} (such as the laminate in Chapter 7.2) shows that these types of lay-up offer enhanced damage tolerance

under fatigue loading. However, it should be noted that the laminate was manually optimised to maximise buckling strain and minimise SERR. It was not optimised using any specific design strategy nor did it consider other constraints, such as buckling or aeroelasticity.

Assuming damage morphology seen in the experimental coupons in this paper, an optimisation methodology, based on the above CAI model, has derived a stacking sequence $[45/90_2/0_4/\text{-}45/45/0_4/\text{-}45/0_2]_s$ which produces, depending on choice of initial conditions, an increase in CAI strength of up to 84% in comparison to the analytical threshold strain, 3780 μstrain, calculated for the original stiffener. In addition, when compared to the highest recorded experimental threshold strain, 4540 μstrain for the 11J coupon, an increase of up to 53% is seen. The optimised laminate was designed via a re-distribution of the existing plies in the experimental stiffener sections and so maintains the same in-plane stiffness.

In summary, a modelling procedure has been developed that is accurate, computationally efficient and flexible enough to be adapted to a wide range of BVID propagation problems in two distinct loading regimes with a minimum of problem preparation. The efficiency and accuracy of the model give it the flexibility to be an excellent preliminary design tool allowing multiple stacking sequences to be considered in a short period of time making it an ideal candidate for the basis of an optimisation routine. This routine has been used to develop Optimised laminates that theoretically improve damage tolerance in all cases and in the case of static loading of coupons this has been experimentally verified.

10. Future and ongoing work

Currently, the model deals with and has only been tested on flat axially compressed coupons that have been impacted normal to their surface using a hemi-spherical tup. This is however, a reasonable approximation to most low-velocity BVID causing impacts on an aircraft wing as impacts are likely to be normal to the surface and a single large axial load due to lift on the wings dominates the load distribution. Clearly though, a more representative problem would be an oblique impact from an object with an asymmetric geometry on a curved plate under combined loadings. Hence, some future research effort should be directed toward applying the model to this more representative problem.

Although the above problem extensions apply to free edge impacts the free edge problem is not as well understood as the plate and hence it would be beneficial to explore the normal impact/axial compression problem via altering material properties, impact energies, laminate stacking sequences and laminate thicknesses first. In addition, the tup currently used is hemispherical in shape; in the case of free edge stiffener impact it would be interesting to analyse the effect of a cylindrical bar shaped tup on the damage morphology. It is anticipated this tup would enhance the applicability of the damage model by improving the repeatability of the damage morphology and producing a more consistent through thickness damage profile. In addition, experiments should be undertaken in order to validate the suggested free edge optimised stacking sequences.

An essential part of the novelty of this model and its advantage over other models dealing with the same problem is that it is analytically based and as such is computationally efficient. However, the model

is not fully analytic; it relies on experimental descriptions of damage and the finite strip program VICONOPT to calculate buckling strain. By making the modelling fully analytical and developing or marrying the model with an existing impact damage model computation times could be reduced further. Alternatively, an analytical approach to determining the largest delamination diameter combined with the linear damage model could provide an intermediate step to a fully analytical damage model. However, any change to the current damage approximation strategy would need to be computationally efficient to maintain the advantage offered by the current methodology.

The overall concept of this work is to increase damage tolerance of composite aircraft components. A step has been taken towards this via the optimisation undertaken in this work. However, an improved optimisation procedure for damage tolerant laminates based on the propagation model would be essential to make further progress in this problem. This may be accomplished by producing a method that can identify weak interfaces and/or cause them to occur deeper in the laminate. Alternatively, a 'null' stacking sequence could be produced that minimised axial, shearing and bending stresses between layers which are the drivers for delamination propagation.

Work is currently in progress on the application of the modelling technique set out in this thesis to composite sandwich panels. This work is being undertaken by Moustafa Kinawy and some preliminary results are recorded in [81]. The technique is also the basis for ongoing research effort by Neil Baker into selecting laminate stacking sequences optimised for damage tolerance. Again preliminary results are recorded in [80].

Future projects under discussion that are related to the methods developed in this thesis include:

- Investigation of the impact face dependent damage tolerance properties of fully isotropic laminates in collaboration with Dr. Chris York at the University of Glasgow.
- Under the supervision of Dr. Richard Butler at the University of Bath, identification of interfaces at a depth within laminates where delamination buckling does not occur that could have their damage resistance properties diminished in a controlled fashion to produce ‘safe’ areas for impact delamination to form. In essence, drawing damage away from more critical load carrying regions hence increasing overall damage tolerance.
- Further to the last point and in collaboration with Dr. Ian Bond at the University of Bristol, self healing layers maybe introduced in either the ‘safe’ regions or at the interface the model has calculated as being the weakest i.e. the first at which damage will propagate.
- Under the supervision of Dr. Butler investigate the compression after impact strength of curved laminates including modelling of the problem described by Short et al [39]. Note VICONOPT input files can be adjusted to take account of curved surfaces. However, the validity of the thin-film and Mode I propagation assumptions remains to be seen and may require some alteration of the model.

References

[1] U.S. Department of Transportation Federal Aviation Administration. “Advisory Circular 20-107B. Draft.

[2] K.-F. Nilsson, L.E. Asp, J.E Alpman, L. Nystedt. “Delamination buckling and growth for delaminations at different depths in a slender composite panel”. Int.J. Solids and Structures, Vol.38, 2001, p.3039-3071.

[3] H. Chai, C.D. Babcock. “Two-dimensional modelling of compressive failure in delaminated laminates”. Journal of Composite Materials, Vol.19, Jan 1985, p.67-98.

[4] G.A. Kardomateas. “The initial post-buckling and growth behaviour of internal delaminations in composite plates”. Journal of Applied Mechanics, Vol.60, 1993, p.903-910.

[5] R. Butler, D.P. Almond, G.W. Hunt, B. Hu, N. Gathercole. “Compressive fatigue limit of impact damaged composite laminates”. Composites: Part A, Vol.38, 2007, p.1211-1215.

[6] H. Chai, C.D. Babcock, W.G. Knauss. “One dimensional modelling of failure in laminated plates by delamination buckling”. Int. J. Structures, Vol.17, No.11, 1981, p.1069-1083.

[7] S.-F. Hwang, G.-H. Liu. “Buckling behaviour of composite laminates with multiple delaminations under uniaxial compression”. Composite Structures, Vol.53, 2001, p.235-243.

[8] G.L. Melin, J. Schön. “Buckling behaviour and delamination growth in impacted composite specimens under fatigue load: an experimental

study". Composites Science and Technology, Vol.61, 2001, p.1841-1852.

[9] A.T. Rhead, R. Butler. "Compressive static strength model for impact damaged laminates". Compos Sci Technol. 2009, doi:10.1016/j.compscitech.2009.01.010.

[10] P.T. Curtis, J. Gates, C.G. Molyneux, "Impact damage growth in carbon fibre composites". Defence Research Agency, Farnborough, Hampshire, Technical Report 93009, 1993.

[11] G.L. Melin, J. Schön, T. Nyman. "Fatigue testing and buckling characteristics of impacted composite specimens". Int J Fatigue, Vol.24, 2002, p.263-272.

[12] A.S. Chen, D.P. Almond, B. Harris. "In situ monitoring in real time of fatigue-induced damage growth in composite materials by acoustography". Composites Science and Technology, Vol.61, 2001, p.2437-2443.

[13] N. Uda, K. Ono. "Compression fatigue failure of CFRP laminates with impact damage". Proceedings of 16th ICCM Kyoto, Japan, 2007.

[14] E. Greenhalgh, C. Meeks, A. Clarke, J. Thatcher. "The effect of defects on the performance of post-buckled CFRP stringer-stiffened panels". Composites: Part A, Vol. 34, 2003, p.623-633.

[15] A. Malhorta, F.J. Guild, M.J. Pavier. "Edge impact to composite laminates: experiments and simulations". J Mater Sci, Vol.43, 2008, p.6661-6667.

[16] G.A.O. Davies, X. Zhang. "Impact damage prediction in carbon composite structures". Int. J. Engng, Vol.16, No.1, 1995, p.149-170.

[17] J. Lee, C. Soutis. “Prediction of impact-induced fibre damage in circular composite plates”. Applied Composite Materials, Vol.12, 2005, p.109-131.

[18] L. Lammerant, I. Verpoest. “Modelling of the interaction between matrix cracks and delaminations during impact of composite plates”. Composites Science and Technology, Vol.56, 1996, p.1171-1178.

[19] Y. Qian, S.R. Swanson, R.J. Nuismer, R.B. Bucinell. “An experimental study of scaling rules for impact damage in fibre composites”. Journal of Composite Materials, Vol.24, May 1990, p.559-570.

[20] R. Ollsson. “Closed form prediction of peak load and delamination onset under small mass impact”. Comp. Struct., Vol. 59, 2003, p.341-349.

[21] R. Ollsson. “Analytical prediction of large mass impact damage in composite laminates”. Composites Part A, Vol.32, 2001, p.1207-1215.

[22] R. Ollsson, M.V. Donadon, Falzon B.G. “Delaminated threshold load for dynamic impact on plates”. Int. J. Sol. Struct., Vol.43, 2006, p.3124-3141.

[23] E. Greenhalgh, A. Clarke, B. Millson, R. Thompson. “Investigation of impact damage in a CRFP wingbox under load”. 41st AIAA Structures, Structural Dynamics, and Materials Conference and Exhibit, April 2000.

[24] C. Breen, F. Guild, M. Pavier. “Impact damage to thick carbon fibre reinforced plastic composite laminates”. J. Mater. Sci., Vol. 41, 2006, p.6718-6724.

[25] D.G. Katerelos, A. Paipetis, V. Kostopoulos. “A simple model for the prediction of the fatigue delamination growth of impacted composite laminates”. Fatigue Fract. Engng. Mater. Struct., Vol.27, 2004, p.911-922.

[26] J.D. Whitcomb. “Parametric analytical study of instability-related delamination growth”. Int. Symp. ‘Composites: Materials and Engineering’, Newark, Delaware, Sept, 1984, p.19-48.

[27] C.S. Yerramalli, A.M. Waas. “A nondimensional number to classify composite compressive failure”. Trans. ASME: J. Applied Mechanics, Vol.71, May 2004, p.402-408.

[28] P. Berbinau, C. Soutis, A. Guz. “On the failure criteria for unidirectional carbon fibre composite materials under compression”. International Applied Mechanics, Vol.35, No.5, 1999, p.462-468.

[29] J.M.T. Thompson, G.W. Hunt. “Elastic instability phenomena”. John Wiley and Sons Ltd., 1984.

[30] G.W. Hunt, B. Hu, R. Butler, D.P. Almond, J.E. Wright. “Nonlinear modeling of delaminated struts”. AIAA Journal, Vol.42, No.11, Nov 2004, p.2364-2372.

[31] H. Suemasu, K. Gozu, K. Hayashi, T. Ishikawa. “Compressive buckling of rectangular composite plates with a free-edge delamination. AIAA J., Vol.32, No.2, 1995, p.312-319.

[32] M.S. Anderson, F.W. Williams, C.J. Wright. “Buckling and vibration of any prismatic assembly of shear and compression loaded anisotropic plates with an arbitrary supporting structure”. J. Mat. Sci., Vol.25, No.8, 1983, p.585-596.

[33] M.S. Anderson, F.W. Williams. “Buckling of simply supported plate assemblies subject to shear loading”. Aspects of the analysis of plate structures: A volume in honour of W. H. Wittrick (A87-20166 07-39). Oxford and New York, Oxford University Press, 1985, p. 39-49.

[34] F.W. Williams, M.S. Anderson, D. Kennedy, R. Butler, G. Aston. “User manual for VICONOPT”. NASA CR-181966, 1990.

[35] C.G. Diaconu, P.M. Weaver. “Postbuckling of long unsymmetrically laminated composite plates under axial compression”. Int. J. Solids and Structures, Vol.43, 2006, p.6978-6997.

[36] G.Z. Harris. “The buckling and post-buckling behaviour of composite plates under biaxial loading”. Int. J. Mech. Sci., 1975, Vol.17, p.187-202.

[37] H. Chai, W.G. Knauss, C.D. Babcock. “Observation of damage growth in compressively loaded laminates”. Experimental Mechanics, Sept 1983, p.329-337.

[38] G. Zhou, L.A. Rivera. “Investigation for the reduction of in-plane compressive strength in preconditioned thin composite panels”. Journal of Composite Materials, Vol.39, No.5, 2005, p.391-422.

[39] L.E. Asp, S. Nilsson, S. Singh. “An experimental investigation of the influence of delamination growth on the residual strength of impacted laminates”. Composites: Part A, Vol.32, 2001, p.1229-1235.

[40] G.J. Short, F.J. Guild, M.J. Pavier. “Post-impact compressive strength of curved GFRP laminates”. Composites: Part A, Vol.33, 2002, p.1487-1495.

[41] X.W. Wang, I. Pont-Lezica, J.M. Harris, F.J. Guild, M.J. Pavier. “Compressive failure of composite laminates containing multiple delaminations”. Composites Science and Technology, Vol.65, 2005, p.191-200.

[42] A.S. Chen, D.P. Almond, B. Harris. “Acoustography as a means of monitoring damage in composites during static or fatigue loading”. Meas. Sci. Technol., Vol.12, 2001, p.151–156.

[43] J. Lee, C. Soutis, C. Kong. “Static compressive strength of unidirectional carbon fibre-epoxy laminate”. Key Engineering Materials, Vols.334-335, 2007, p.357-360.

[44] B.G. Falzon, K.A. Stevens, G.O. Davies. “Postbuckling behaviour of a blade-stiffened composite panel loaded in uniaxial compression”. Composites: Part A, Vol.31, 2000, p.459-468.

[45] S. Singh, E. Greenhalgh. “Validation data for the development of realistic models of delamination growth in composite structures”. Euromech 400, Impact & Damage Tolerance Modelling of Composite Materials & Structures, Imperial College, London, Sept 1999.

[46] E. Greenhalgh, B. Millson, R. Thompson, P.Sayers. “Testing and failure analysis of a CRFP wingbox containing a 150J impact”. Euromech 400, Impact & Damage Tolerance Modelling of Composite Materials & Structures, Imperial College, London, Sept 1999.

[47] S. Benmedakhene, M.Kenane, M.L. Benzeggagh. “Initiation and growth of delamination in glass/epoxy composites subjected to static and dynamic loading by acoustic emission monitoring”. Composites Science and Technology, Vol.59, 1999, p.201-208.

[48] T. Nyman, A. Bredberg, J. Schön. “Equivalent damage and residual strength for impact damaged composite structures”. J. Reinforced Plastics and Composites, Vol.19, No. 06, 2000, p.428-448.

[49] H. Suemasu, T. Kumagai, G. Katsuhisa. “Compressive behaviour of multiply delaminated composite laminates part 1: experiment and analytical development”. AIAA Journal, Vol.36, No.7, 1998, p.1279-1285.

[50] G.A. Kardomataes, A.A. Pelegri. “The stability of delamination growth in compressively loaded composite plates”. Int. J. Fract. Vol. 65, 1994, p.261-276.

[51] P. Chen, S. Zhen, W. JunYang. “A new method for compression after impact strength prediction for composite laminates”. Journal of Composite Materials, Vol.36, No.5, 2002, p.589-609.

[52] Y. Zhuk, I. Guz, C. Soutis. “Compressive behaviour of thin-skin stiffened composite panels with a stress raiser”. Composites: Part B, Vol.32, 2001, p.697-709.

[53] D. Bruno, A. Grimaldi. “Delamination failure of layered composite plates loaded in compression”. Int. J. Solids and Structures, Vol.26, No.3, 1990, p.313-330.

[54] N.K. Naik, R. Ramasimha. “Estimation of compressive strength of delaminated composites”. Composite Structures, Vol.52, 2001, p.199-204.

[55] T.E. Tay. “Characterisation and analysis of delamination fracture in composites: An overview of developments from 1990 to 2001”. ASME Appl Mech Rev, Vol.56, No.1, 2003, p.1-31.

[56] V.J. Hawyes, C. Soutis, P.T. Curtis. “Effect of impact damage on the compressive response of composite laminates”. Composites: Part A, Vol.32, 2001, p.1263-1270.

[57] J.H. Ahn, A.M. Waas. “Mircomechanics-based predictive model for compressively loaded angle-ply composite laminates”. AIAA, Vol. 38, No.12, Dec 2000, p.2299-2304.

[58] M.F.S.F.de Moura, J.P.M. Gonçalves, A.T. Marques, P.M.S.T. de Castro. “Prediction of compressive strength of carbon-epoxy laminates

containing delamination by using a mixed mode damage model". Composite Structures, Vol.50, 2000, p.151-157.

[59] A. Riccio, F. caramuzzino, P. Perugini. "Embedded delamination growth in composite panels under compressive load". Composites: Part B, Vol.32, 2001, p.209-218.

[60] H. Chen, X. Sun. "Residual compressive strength of laminated plates with delamination". Composite Structures, Vol.47, 1999, p.711-717.

[61] F. Shen, K.H. Lee, T.E. Tay. "Modeling delamination growth in laminated composites". Composites Science and Technology, Vol.61, 2001, p.1239-1251.

[62] Y. Zhuk, C. Soutis, I. Guz. "Prediction of the compression-after-impact strength of thin-skin stiffened composite panels". Advanced Composites Letters, Vol.9, No.4, 2000, p.281-287.

[63] L.E. Asp, K.-F. Nilsson. "Delamination criticality in slender compression-loaded composite panels". Key Engineering Materials, Vols.221-222, 2002, p.3-16.

[64] J. Yang, Y. Fu. "Analysis of energy release rate for composite delaminated cylindrical shells subjected to axial compression". Acta Mech. Sin., Vol.22, 2006, p.537-546.

[65] J.E. Herencia, P.M. Weaver, M.I. Friswell. "Local optimisation of long anisotropic laminated fibre composite panels with T shape stiffeners". AIAA Structures, Structural Dynamics, and Materials Conference, May 2006.

[66] S. Adali, A. Richter, V.E. Verijenko. "Optimization of shear-deformable laminated plates under buckling and strength criteria". Composite Structures, Vol.39, No's 3-4, 1997, p.167-178.

[67] S. Adali, M. Walker, V.E. Verijenko. “Multiobjective optimization of laminated plates for maximum prebuckling, buckling and postbuckling strength using continuous discrete ply angles”. Composite Structures, Vol.35, 1996, p.117-130.

[68] C.G. Diaconu, P.M. Weaver. “Approximate solution and optimum design of compression-loaded, postbuckled laminated composite plates”. AIAA Journal, Vol.43, No.4, 2005, p.906-914.

[69] J.F.M. Wiggenraad, R.W.A. Vercammen, P. Arendsen, L.C Ubels. “Design optimization of stiffened composite panels for damage resistance”. 41st AIAA Structures, Structural Dynamics, and Materials Conference and Exhibit, April 2000.

[70] C. Bouvet, B. Castanié, J-J. Barrau. “Modelling of impact damage in laminated composites”. In: Proceedings of 13th ECCM 2008, Stockholm, Sweden.

[71] E. Greenhalgh, M. Bishop, D. Bray, D. Hughes, S. Lahiff, B. Millson.” Characterisation of impact damage in skin stringer composite structures”. Comp. Struct., Vol.36, 1996, p.187-207.

[72] D. Hull, Y. Shi. “Damage mechanism characterization in composite damage tolerance investigations”. Comp. Struct., Vol.23, 1993, p.99-120.

[73] A.T. Rhead, R. Butler, G.W. Hunt. “Post-buckled propagation model for compressive fatigue of impact damaged laminates”. Int. J. Sol. Struct., Vol.45, No.16, 2008, p.4349-4361.

[74] H. Suemasu, W. Salsaki, Y. Aoki, T. Ishikawa. “Compressive behaviour of impact damaged laminates”. 16th International Conference on Composite Materials, Kyoto, 2007.

[75] W.T. Koiter, M. Pignataro. “A general theory for the interaction between local and overall buckling of stiffened panels”. Delft University of Technology Report, WTHD-83, 1976.

[76] M.E.Grayley. “Buckling of rectangular specially orthotropic plates”. ESDU technical report: 80023.

[77] V. La Saponara, H. Muliana, R. Haj-Ali, G.A. Kardomateas. “Experimental and numerical analysis of delamination growth in double cantilever laminated beams”. Eng. Frac. Mech.,Vol.69, No.6, 2002, p.687-699.

[78] W. Liu, R. Butler, A.R. Mileham, A.J. Green. “Bilevel Optimisation and Postbuckling of Highly Strained Composite Stiffened Panels”. AIAA J., Vol.44, No.11, 2006, p.2562-2570.

[79] A. T. Rhead, R. Butler and N. Baker. ”Compression testing of laminates optimised for damage tolerance”. 17th International Conference on Composite Materials, Edinburgh, 2009.

[80] N. Baker, A.T. Rhead, R. Butler. “Optimisation of aerospace laminates for damage tolerance”. 7th ASMO-UK/ISSMO international conference of engineering design optimisation, 2008.

[81] M. Kinawy, R. Butler. “Face damage growth of sandwich composites under compressive loading”. 17th International Conference on Composite Materials, Edinburgh, 2009.

Appendix I

Below is a typical input file for VICONOPT. The exact functions of each input field can be obtained from [33] but the use of input fields as they pertain to the problems defined in this work will be described in turn below.

```
pri
3
len 0.021
vic 5 5
MAT
1 133E9 .29 0 3.6E9 10.8E9
LAY
1 0.00013 1 0
2 0.00013 1 90
3 0.00013 1 45
4 0.00013 1 315
5 0.0003102001 2 0
WAL
1 1 1 3 4 2
PLATE
1 0.0035 1 1
STR
1 43669.94 0 -53.8586
CON
1 2 1  2 3 1  3 4 1  4 5 1  5 6 1  6 7 1
ATT
```

```
1 901 7 901
LON
34
POI
123456
1 7
X 0.0105
123456
2 6
X 0.002673762079 0.01832623792
123456
3 5
X 0.000600505063 0.02039949494
123456
4
X 0
PLO
2 3
CRO
0
RES
INMOD=1
END
```

`Pri with in` This command determines which extra data is to be printed along the results of the analysis. In this case the ‘3’ indicates that the data the WAL group is to be returned.

`Len` This function followed by a numeric value gives the length of the strips in Figs. 11 and 13.

`vic` Calls VICON analysis function (see [31]) with numeric values relating to the number of trial wavelength periodicity values to be used and the number of half-wavelengths which are considered in the analysis. The latter helping to produce a convergent solution.

`MAT` Determines the material properties of the layers in the laminate under investigation. The first value is a material identifier; more than one material may be used in laminates that mix carbon and glass fibre layers. The five remaining values relate to the material properties E11, V12, Density (always 0 as not required to determine buckling loads), G12, E22 respectively.

`LAY` This identifier gives individual layers that are used to form the laminate. The first value identifies the layer, the second defines layer thickness, the third calls the material type from `MAT` and the final value gives layer orientation.

`WAL` As before, the first value is an identifier then the following values are layer identifiers called from `LAY` that give the laminate stacking sequence in order from the top surface down.

`PLATE` The plate function describes each strip in this case a single strip is used repeatedly so only a single strip is defined with width given by the second value (the first being the `PLATE` identifier) and the stacking sequence being given by the third. The fourth relates to the loadings placed on the strip.

STR The first number defines as before is an identifier. The rest of the numeric values define the longitudinal (see Fig.11), shear and transverse loads respectively.

CON The first two numbers of these numerical triplets determine two nodes that are to be connected. The third value is the plate identifier number which specifies which plate lies between the nodes.

ATT ATT determines fixed line supports at the nodes specified by the single digits in the line; in this example, nodes 1 and 7. The numerical triplets define that a line support is being used (the '90' part) with the first line of LON data.

LON The doublet of data defines which degrees of freedom are restrained by the longitudinal support in this case movement out of plane and rotation in the plane defined by the transverse and out of plane directions. Normally further values would follow but as the supports in this case offer infinite restraint which is notated by a 0 the value can be omitted.

POI The list of three lines determines point supports used to produce a circular boundary. The first line determines the degrees of freedom that are to be restrained. This is any combination of numbers 1 to 6 that refer to the three possible translations and 3 possible rotations. The second line determines along which node lines the supports apply and the third line determines the position along the line.

PLO This produces plots of the structure and mode shapes. Five possible plotting types are available with options available for each. In this case un-deformed structures with dashed lines and contour and isometric plots are displayed.

CRO Using this option cross sectional plots of the structure can be produced. The 0 value used in the example indicates the whole structure should be plotted.

RES The RESet command allows special lines of data to be changed from their default values and in this case allows the INMOD command to be used.

INMOD This command forces all cross sectional plots to be plotted more accurately than normal.

END Indicates the data input of the problem data has come to an end.